Ultrafast Optical Studies of Multiple Exciton Generation in Lead Chalcogenide Quantum Dots

by

Aaron G. Midgett

B.S., University of North Carolina, at Asheville, 2005

A thesis submitted to the

Faculty of the Graduate School of the

University of Colorado in partial fulfillment

of the requirement for the degree of

Doctor of Philosophy

Department of Chemistry and Biochemistry

2011

This thesis entitled:

Ultrafast Optical Studies of Multiple Exciton Generation in Lead Chalcogenide Quantum Dots

written by Aaron Gilbert Midgett

has been approved for the Department of Chemistry and Biochemistry

_____

Arthur J. Nozik

_____

David Jonas

Date_____

The final copy of this thesis has been examined by the signatories, and we find that both the content and the form meet acceptable presentation standards of scholarly work in the above mentioned discipline.

Midgett, Aaron Gilbert (Ph.D. Chemistry)

Ultrafast Optical Studies of Multiple Exciton Generation in Lead Chalcogenide Quantum Dots

Thesis directed by Professor Arthur J. Nozik and Professor David Jonas

Providing affordable, clean energy is one of the major challenges facing society today, and one of the promising solutions is third generation solar energy conversion. Present day, first and second-generation solar cells can at most convert each absorbed photon into a single electron hole pair, thereby establishing a theoretical limit to the power conversion efficiency. The process of multiple exciton generation (MEG) in semiconductor quantum dots increases that theoretical efficiency from 33% to 42% by utilizing the excess energy of high energy photons that is otherwise wasted as heat to excite a second electron-hole pair, thereby boosting the potential photocurrent. This thesis explores the benefits of MEG in quantum confined systems and shows that quantum dots are more efficient at generating multiple excitons from a single photon than bulk semiconductors. The variations in optical measurements of MEG have raised skepticism and brought into question the validity of these experiments. The two important questions that this thesis attempts to address are (1) what are the enhanced QYs in isolated PbSe QDs and (2) does quantum confinement enhance MEG over bulk semiconductors. Experimental variations in the enhanced QYs are partially explained by the production of a long-lived photocharged

state that increases the apparent photon-to-exciton QYs. A procedure is detailed that decreases the possibility of producing this charged state. By studying the production of these states, conditions are found that minimize their effect and produce less variation in the reported QYs. Variations in the MEG efficiency were studied in films of chemically treated PbSe quantum dots where a different mechanism was responsible for an apparent decrease of the measured QYs. Finally, for the first time, a quantum dot size-dependence in the MEG efficiency was found in colloidal PbSe, PbS, and PbS_xSe_{1-x} quantum dot solutions and is attributed to the increased Coulomb interaction in materials with a larger Bohr exciton radius. These results will allow a better understanding of MEG and how this important process may be used to enhance solar energy conversion.

Acknowledgements

First and foremost, I would like to thank my advisors, Art Nozik and David Jonas. When I first met Art, he told me that he was no longer accepting new students, since he was retiring. I am so very grateful that he changed his mind, and now, five years later, Art seems more enthusiastic about his work than ever. I am exceptionally grateful to Matt Beard for being a wonderful teacher and supportive mentor. Matt is the reason that my graduate school career has gone as smoothly as it has and the only reason that I have had a working laser for most of my time at NREL. To the rest of my group and all of my fellow scientist at NREL, I appreciate all of the help you have given me: from the many samples that I didn't have time to make, to enlightening scientific discussions, to Philly cheesesteak days and learning about the . Barbara Hughes, Octavi Semonin, Justin Johnson, Danielle Smith, Matt Bergren, Kevin Mistry, Joey Luther, Jianbo Gao and Ryan Smith have been a wonderful and sportive group to work with, and I hope that I have the chance to collaborate with all of you in the future. And finally, thank you to my family for all of their loving support in a stressful few years. Steve and Caitlin, thank you for starting me on this journey of scientific discovery and instilling this love of learning in me. Jacob and Terra, I am so lucky to have you as siblings. Susie and Add, thank you for always providing us with the best possible weekend getaways. Nala, you are such a loving soul and you make my life better. And possibly the one who deserves the most credit, Kim, thank you for all of your loving support. I could not have made it without you, and I am very excited to spend the rest of my life with you.

Contents

Tables

Figures

Chapter 1: General Introduction

1.1 The Energy Crisis

The motivation behind the search for cost effective, carbon neutral, renewable energy sources is readily apparent in all areas of our daily life. Since the industrial revolution, the human need for high quality, inexpensive energy has driven both exploration and technology. For most of that time, that need was filled by fossil fuels, which today comprise 85% of the U.S. energy supply.[8] Since their rise to power in the industrial revolution, fossil fuels have always been readily available and inexpensive. The problem with fossil fuels that the cost of mining and distributing coal and oil does not take into account is their cost to the environment and their finite availability. Because of these two missing factors, fossil fuels are sold for considerably less than their true costs, on a larger scale, meaning that other energy sources are not able to compete. This has meant that for the last two hundred years, fossil fuels have had a monopoly on the energy market, while slowly changing the climate of our planet. We have now come to expect an unlimited supply of relatively inexpensive energy, and therefore, any replacement must be cost effective, easily transportable and widely available.

Based on these criteria, there are a limited number of sources that are capable of providing the energy needed, and none that can do so for the same price that oil, coal and gas are sold for today.[9] The most obvious untapped energy source is harnessing the power from the sun. More energy strikes the earth, in the form of sunlight, in a single hour (4.3×10^{20} J) than humans consumed on the entire planet in 2001 (4.1×10^{20} J).[9] The current technology for collecting this energy is insufficient. While fossil-fuel-derived energy can be produced for as little as \$0.02-0.05 $(\text{kW-hr})^{-1}$, the average cost of solar cells, based on a twenty year lifetime, are in the range of

$0.21-0.46 (kW-hr)$^{-1}$ for a commercial utility scale power plant.[10] Due to the large discrepancy between the costs of these two energy sources, incremental improvements to the cost of solar cells are not enough, and instead, new revolutionary ideas must be implemented that are not only more cost effective, but also more efficient. This is the area of solar research categorized as third generation.

1.2 Solar Cells: Generating Electricity from Light

Solar cells are designed to absorb photons from sunlight and convert that energy into electricity by taking advantage of the photovoltaic effect and separating an electron and hole across the bandgap of the semiconductor. If a photon does not have enough energy to excite an electron across the gap, it will either be transmitted or scattered. On the other hand, if the photon has more energy than the bandgap of the semiconductor, the excess kinetic energy is lost to heat as the high-energy electron and hole cool to the bandedge. Once the electron is separated from the hole, a built in asymmetry in the device (usually created with a junction of electrically different materials) causes the electrons to flow through an external circuit where they can be used to do electrical work.[11] The efficiency of a solar cell can then be calculated by the following equation:

$$\eta = \frac{V_{OC} \times I_{SC} \times FF \times M}{A \times P_{IN}} \tag{1.1}$$

where V_{OC} is the open circuit voltage, I_{SC} is the short circuit current, FF is the fill factor (the maximum power divided by the $V_{OC} \times I_{SC}$ product), M is the spectral mismatch, A is the device area and P_{IN} is the incident optical power density at 1 sun (1000 W m^{-2}). The delicate balance of collecting the most photons possible while keeping the highest voltage based on the solar spectrum creates an upper limit to the theoretical efficiency of a traditional, single bandgap,

terrestrial solar cell. This detailed balance calculation, originally defined in 1961, leads to the Shockley-Queisser limit of 30-33% for solar cells with bandgaps in the range of 1-1.6 eV.[12] As can be seen in Figure 1.2.1, while some of the energy loss is due to the transmission of low energy photons, the majority of the lost energy (almost 50%) is due to heat created as the high energy charge carriers cool to the bandgap. By accessing this lost energy, the theoretical efficiency of a solar cell increases, and the goal of third generation solar is realized.

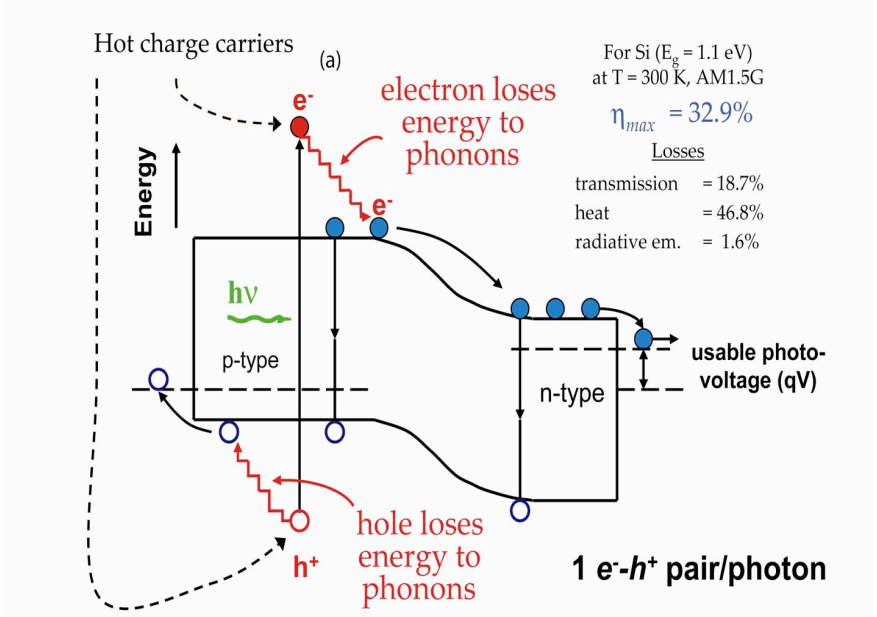

Figure 1.2.1: Solar Cell Schematic
This schematic of a solar cell shows the absorption of a photon with energy greater than the bandgap of the material that then promotes an electron into the conduction band where it can be separated from the hole and used to do work. Notice that the majority of the energy loss comes from the relaxation of high energy electron hole pairs to the bandedges. Reprinted with permission from reference 3.

1.3 Utilizing the solar spectrum: Breaking the Shockley-Queisser Limit

In order to overcome the SQ limit, a greater energy conversion of the photons in the solar spectrum must be collected. Several methods have been proposed to increase the energy conversion efficiency, but all of them come with significant challenges. As one example,

multiple junction cells[13] employ several materials with different bandgaps that are stacked monolithically. While these cells do achieve power conversions efficiencies (PCE) of greater that 30%, they have prohibitively high costs of up to two hundred times more than first generation solar cells. These conversion systems work by collecting the highest energy photons within a high bandgap material at the front of the cell, while the lower energy photons pass through to the next layer, and so fourth. In this way, a larger portion of the available photons can be collected, and the voltage of each layer can be collected independently, so that the energy in each photon is more efficiently used. The additional construction of the completed system increases the cost to an unacceptable level, and consequently multi-junction cells are only used in concentrator cells, or in space applications where weight is a large contribution to the overall cost. Another approach is to collect the nascent carriers before they have a chance to cool to the bandedge (due to phonon scattering and emission). Hot carrier extraction would lead to an increased photovoltage, but in order for this to occur, carrier separation and transport would have to happen on a time scale faster than the carrier cooling rate.[14,15] While slowing the cooling rate is a meaningful approach, the fact that carrier cooling in bulk semiconductors occurs on the sub-ps time scale means that little progress has been made, despite intense efforts. The final process that is discussed and is also the basis of this thesis is multiple exciton generation in semiconductor quantum dots.

1.4 Multiple Exciton Generation

Multiple exciton generation (MEG) is the process by which a single high energy photon can produce more than one electron hole pair in a quantum confined material (see Figure 1.4.1). This breaks the SQ limit through a process similar to impact ionization in bulk materials. Impact ionization (II) in bulk materials (one high energy photon creating more than one electron hole

pair) was well studied starting in the 1950s, but was found to not be very efficient due to the energy and momentum conservation that must be present in bulk systems. This means that the threshold for impact ionization is often four to six times the bandgap of the material, requiring photons well in the UV that are not present in the solar spectrum for ideal gap semiconductors. The exact mechanism for the MEG process is unknown, but the end result is that the excess kinetic energy found in a hot carrier can be used in a reverse Auger process to excite one or more extra electron hole pairs significantly more efficiently than in bulk materials. Auger recombination and cooling are well known processes that can aid in the increased cooling of many materials, in particular in cases with increased coulomb coupling (such as quantum confined systems). In Auger recombination, an electron hole pair at the bandedge can give its energy to a second bandedge pair non-radiatively. This leads to faster carrier cooling because the single high energy exciton created quickly cools to the bandedge, effectively allowing for the relaxation of one bandgap worth of energy on the time scale of a hundred picoseconds.[16,17] Auger cooling on the other hand is where a highly excited electron transfers its extra energy to its associated hole therefore bypassing the hot phonon bottleneck because of the greater density of hole states. These processes have been found to be increased in quantum confined systems due to the increased coulomb coupling and the decrease in translational momentum conservation.[18-20] It was this increase in Auger recombination and the fact that momentum is not conserved in quantum confined materials that prompted Nozik to propose that quantum confined materials should be more efficient at generating subsequent electron hole pairs from a single photon using fundamentally different physics than bulk systems.[2,15] Chapter 2 deals with the differences between bulk and quantum dots in detail and provides a mechanism for comparing the MEG efficiency of materials with different bandgaps.

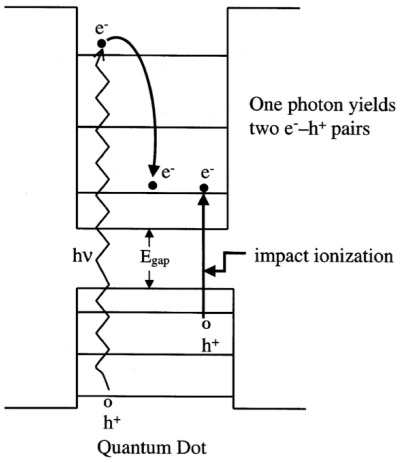

Figure 1.4.1: Multiple Exciton Generation in Quantum Dots
The process of multiple exciton generation is depicted above where one high energy photon can yield two or more electron hole pairs. This process is enhanced in quantum confined materials, due to a slowed carrier cooling rate, decreased momentum conservation and increased Auger processes. Reprinted with permission from reference 2.

1.5 Quantum Confinement

Bulk semiconductor materials are characterized by two distinct distributions of allowed states called the conduction band (lowest unoccupied band) and valence band (highest occupied band) separated by an energy gap (E_g) known as the bandgap of the material (Figure 1.5.1a). When individual atoms bind together, their atomic orbitals split to form pairs of molecular orbitals. For an infinite number of atoms combing in a crystal lattice (bulk solid), the states form continuous energy bands separated by energy gaps instead of isolated energy levels. A semiconductor's bandgap is defined by the electronic properties of electrons in a perfect, infinite lattice and is the amount of energy needed to move an electron from the fully occupied valence band where it is bound, to the unoccupied conduction band, where it can freely move through the material. In metals, the conduction band is partially occupied, so electrons are always free to move through the material, making a conductor, while an insulator has such a large gap that thermal electrons never gain enough energy to cross into the conduction band. A bandgap within the solar spectrum is necessary in a solar cell because electrons and holes cool very quickly (thermalization happens on the order of femtoseconds) through the continuum of states but take much longer to radiatively recombine across the bandgap of a semiconductor. It is this point in

the photovoltaic effect that can be exploited to generate electricity by imparting some asymmetry on the system through the use of an electric field or gradient in electron density allowing the charge carriers to be collected. For a more detailed description of the workings of bulk semiconductors and solar cells, see reference 11.

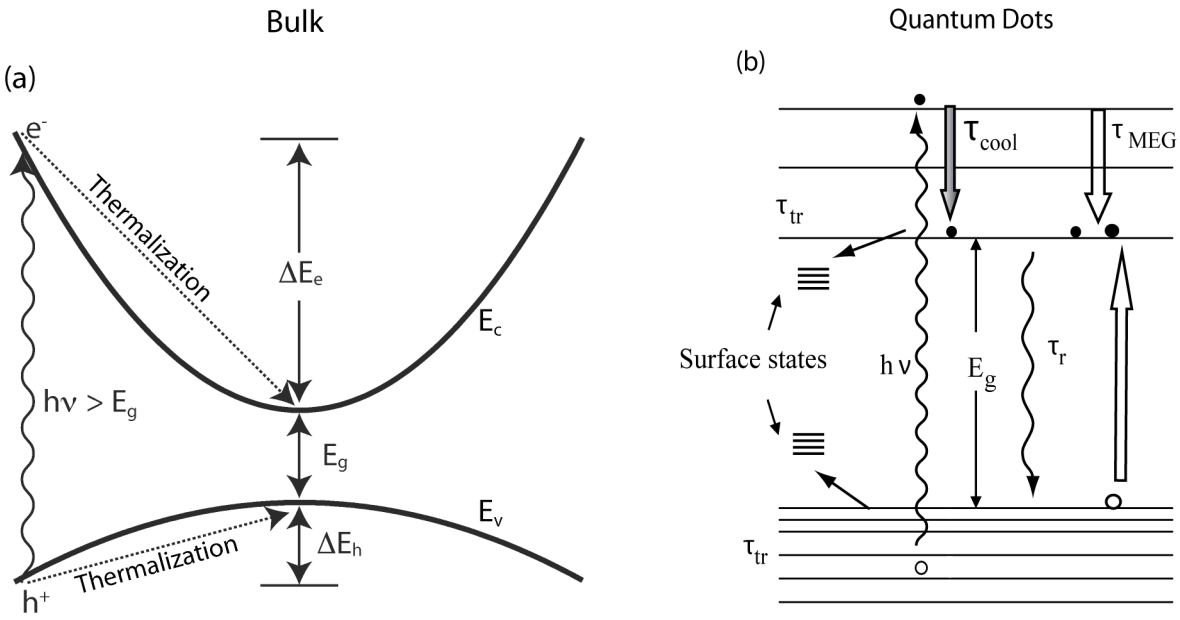

Figure 1.5.1: Quantization of Semiconductor Energy Levels
The band diagrams for (a) bulk semiconductors and (b) quantum dots are shown above with the conduction band at the top and the valence band at the bottom.

When atoms are arranged in much smaller lattices on the order of a few hundred to a few thousand atoms, the conduction and valence bands are no longer continual, but instead an arrangement of energy levels with small intraband gaps on the order of hundreds of meV (Figure 1.5.1b) for states near the bandedges.[3] This effect is caused by the confinement of the electron and hole wavefunctions, which according to the Heisenberg uncertainty principle will lead to a decrease in certainty of momentum with an increase in the certainty of position. The discrete states can now be thought of as a superposition of bulk states, concentrating the oscillator strength to a few transitions and increasing the overall energy of those transitions.[21] The splitting between intraband energy levels in QDs suggests that the cooling of hot electrons should be

slowed when compared to bulk counterparts, because the energy needed for the relaxation between individual states is much larger than the energy of a single optical phonon (1-4 meV) and therefore a multi-phonon process would be necessary. This is the theoretical concept of the phonon bottleneck that should dramatically slow cooling in QDs.[22] While some evidence has been found for slowed cooling in quantum confined systems,[23] the high energy states are found to be more bulk like.[24] This fast cooling through high energy states and the increased Auger coupling can lead to relatively fast overall cooling to the bandedges.

The effective mass approximation is one of the simplest and most successful ways to analytically describe the energy levels found in QDs. This theory is based on the assumption that if the QD is sufficiently larger than the crystal lattice constants, then the lattice properties (along with the same effective mass of carriers) will stay the same. Using this assumption and the modifications in the energy of the charge carriers caused by quantum confinement, the Schrödinger equation of a 3-D particle in a box can be used to describe this system.[15] The Hamiltonian that describes a strongly confined quantum dot where the electron and hole coulomb interactions are enhanced can be written as:

$$\widehat{\mathbf{H}} = -\frac{\hbar^2\nabla_e^2}{2m_e^*} - \frac{\hbar^2\nabla_h}{2m_h^*} - \frac{e^2}{\epsilon|r_e - r_h|} + V_e(r_e) + V_h(r_h) \tag{1.2}$$

and

$$\widehat{\mathrm{H}}\Psi(r) = E\Psi(r) \tag{1.3}$$

where m_e^* and m_h^* are the effective mass of the electron and hole, r_e and r_h are the distances of the electron and hole from the center of the QD, ϵ is the dielectric constant of the bulk material and V_e and V_h are confining potentials. Analytical solutions are difficult for this equation because of the many particles and motions involved, but by treating a QD as a perfect sphere

surrounded by infinite potential while ignoring surface states, perturbation theory leads to the solution[25]

$$\boldsymbol{E_{min} = E_g + \frac{\hbar^2 \pi^2}{2R^2}\left[\frac{1}{m_e^*} + \frac{1}{m_h^*}\right] - \frac{1.8e^2}{\varepsilon R} - 0.25E_{Ryd}^*} \quad (1.4)$$

where E_{min} is the minimum energy between electron and hole states (or the bandgap), E_{Ryd} is the binding energy for the bulk semiconductor and R is the QD radius. Many improvements have been made to this model, but this is the basis of much of the theoretical work on semiconductor quantum dots.[15] The quantum confinement in QDs also leads to crystal momentum no longer being conserved.[26] This is due to the fact that that the eigenfunctions of Equation (1.2) are not able to exist in the confined space of a QD and therefore each allowed state is a linear combination of a continuum of Bloch functions, each with a different translational crystal momentum.[15] This can also be understood in the basic principles found in a particle in a box model, or by applying the Heisenberg uncertainty principle, which states that by knowing the position of a particle more closely, we must lose certainty in the momentum of that particle.

According to Kang and Wise[27] the direct optical transitions that are allowed in QDs are governed by the transition-matrix element defined as:

$$M_{e,h} = \left|\langle \Psi_f(r)|e \cdot \hat{\boldsymbol{p}}|\Psi_i(r)\rangle\right|^2 \quad (1.5)$$

where e is the polarization vector of the light, $\hat{\boldsymbol{p}}$ is the momentum operator and $\Psi_f(r)$ and $\Psi_i(r)$ are the total wavefunctions for the initial and final states. Because of envelope function approximation (valid when the QD diameter is larger than the lattice constant[27]), the total wavefunctions can be represented as a product of the periodic Bloch function ($u_{n,k}$) and an envelope function ($\phi_k(r)$).

$$\Psi_i(r) = u_{ni} \cdot \phi_i(r)$$

$$\Psi_f(r) = u_{nf} \cdot \phi_f(r) \tag{1.6}$$

Since the envelope functions are approximately constant over the entire cell, we can rewrite the transition-matrix element for the interband transitions ($ni \neq nf$) as:

$$\langle \Psi_e(r)|e \cdot \hat{\boldsymbol{p}}|\Psi_h(r)\rangle = \langle u_{vf}|e \cdot \hat{\boldsymbol{p}}|u_{vi}\rangle\langle \phi_f|\phi_i\rangle \tag{1.7}$$

The two parts of this equation can be integrated separately and the Bloch part yields the size-independent dipole matrix element found in bulk. Using the assumptions of a spherical QD in an infinite potential, the relationship developed above and the orthonormality of the envelope functions, the transition-matrix element is only non-zero for interband transitions where quantum numbers are identical in initial and final states. This relationship leads to the conservation of the primary quantum number (n) and angular momentum (l) and the selection rules for interband transitions in QDs of $\Delta n = 0$, $\Delta l = 0$ and orbital angular momentum, $m \leq |l|$.[1,27,28] In real quantum dots, as opposed to perfect spheres in an infinite potential, these selection rules are relaxed and disallowed transitions occur.

The process of quantum confinement begins to be noticed when at least one dimension is less than twice the Bohr radius of excitons in the bulk material.[15] The Bohr radius of an exciton is defined as:

$$\boldsymbol{a_B} = \boldsymbol{\epsilon_\infty} \frac{\boldsymbol{m_e}}{\boldsymbol{m^*}} \boldsymbol{a_0} \tag{1.8}$$

where $\boldsymbol{\epsilon_\infty}$ is the optical dielectric constant of the material, m_e is the electron mass, m^* is the reduced effective mass of the exciton and a_0 is the Bohr radius of the hydrogen atom ($a_0 = 0.529\text{Å}$).[29] The relationship between the Bohr radius, the dielectric constant and the MEG efficiency is discussed in detail in Chapter 4. This thesis focuses on colloidal quantum dots that

are synthesized in solution and are characterized by having ligands on the surface of the nanocrystal that serve to keep the quantum dots in solution and act as a potential barrier that confine the electron and hole. It is this confinement that allows the energy levels in quantum dots to be tuned with size. As can be seen in Figure 1.5.2, the bandgap of QDs is inversely proportional to the size of the dot. From this figure, it is clear that the size distribution of the QD samples is extremely good and that very small changes in the size of these QDs (less than a single monolayer of atoms) can considerably change the bandgap absorption. The confinement found in quantum dots is what provides their new physical properties including increased Auger recombination, increased coulomb coupling, decreased cooling rates and most importantly for this work, an increase in MEG efficiency.

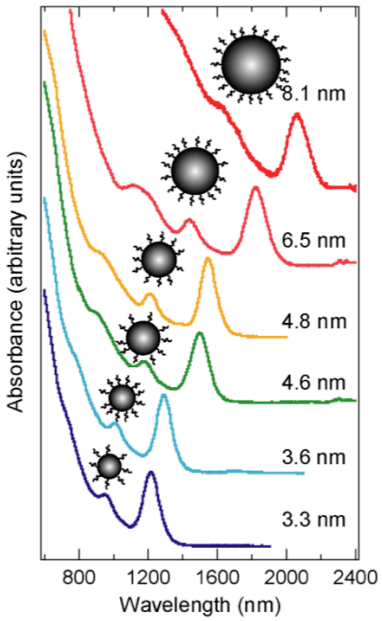

Figure 1.5.2: Quantum Dot Size Dependence
The semiconductor bandgap is controlled by the size of the crystal in quantum confined systems. For PbSe nanoparticles, extremely good size distributions can be obtained and less than a single monolayer of atoms can dramatically change the energy gap of the material. Reproduced with permission in part from reference 3.

1.6 Femtosecond Transient Absorption

The majority of these experiments were conducted using an ultrafast transient absorption pump probe experiment depicted in Figure 1.6.1a and described in detail in reference 3. Transient absorption spectroscopy (TA) monitors the change in transmission of a weak probe pulse over a delay time with the excitation by an intense pump pulse. Our experiment consisted of an amplified Ti:Sapphire laser seeded with a broadband Ti:Sapphire oscillator, that is able to produce ~60fs pulses of 810nm light at a repetition rate of 1kHz and a pulse energy of 3.5mJ. This beam is used to pump two tunable optical parametric amplifiers that can provide wavelengths between 290nm-2,300nm for the pump beam and 290nm-10,000nm for the probe. The pump beam is blocked every other pulse so that a transmission measurement can be taken with and without the pump pulse. This allows for an accurate determination of the transmitted light with and without pumping and produces a differential transmission signal ($\Delta T/T$) seen in Figure 1.6.1c. The probe beam can be delayed up to 1.5 ns so that the dynamics of the initial relaxation can be determined. When the $\Delta T/T$ signal is small, then the following relationship with the absorption coefficient (α) is true:

$$\Delta\boldsymbol{\alpha}\cdot\boldsymbol{l} = -\ln\left(\frac{\Delta\boldsymbol{T}}{\boldsymbol{T}}+\mathbf{1}\right)\approx -\frac{\Delta\boldsymbol{T}}{\boldsymbol{T}} \tag{1.8}$$

where l is the pathlength. When the pump pulse excites electrons to the bandedge (or above) the absorption at the probe wavelength (the bandedge) decreases, or bleaches, due to state filling and the overall result is a signal at early times that is proportional to the total number of electron hole pairs in the first excited state.[3,16] Chapter 3 gives a detailed explanation of how this experiment

is used to determine the MEG efficiency in semiconductor QDs, but it is this differential transmission signal that all of these experiments are based on.

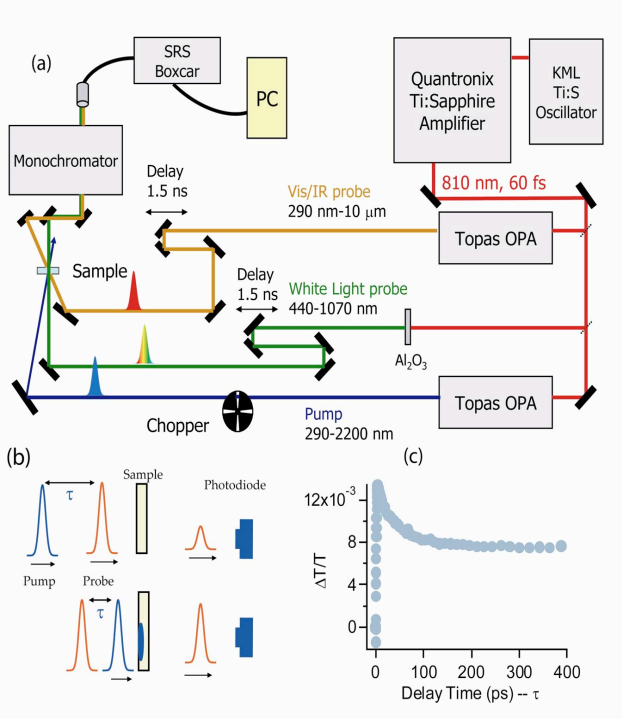

Figure 1.6.1: Transient Absorption Experiment
(a) Schematic of the transient absorption experiment used for the determination of MEG efficiencies in QD solutions and films. For this work, the IR probe was used due to the smaller bandgap of the materials used. TA is a pump probe experiment (b) where a pump pulse excites the sample and the sample is then probed at the bandedge by the probe beam. The result is an increased transmittance (c) when the probed state is occupied so the change in transmission signal over transmission (ΔT/T) shows the population of occupied states and how those states decay. Reprinted with permission from reference 3.

1.7 Thesis Focus

This thesis will investigate the increase in MEG efficiency found in semiconductor QDs and some of the complications that arise in the pulsed laser experiments used to measure these efficiencies. The goal of all of these experiments is to gain a more complete understanding of the MEG process so that more efficient materials can be designed in the future. Since optical spectroscopy was the first technique used to show that MEG is enhanced in QDs over bulk, it is

important that these measurements are understood and that any systematic error associated with these experiments is eliminated.

After the introduction in the first chapter, the second chapter provides a detailed explanation of the differences between MEG in QDs and impact ionization in bulk semiconductors and shows that MEG in QDs is enhanced over bulk. This enhancement suggests new physics are involved. This chapter also defines a scale to compare the MEG of different materials, independent of bandgap, and shows that the efficiency of all materials studied is closely related to the onset of MEG. This chapter was originally published in Nano Letters and is reproduced here with minor formatting changes with permission from reference 30.

The third chapter explains the experimental details how the MEG efficiency is determined and how to avoid some of the systematic errors that have led to a large amount of error in photon-to-exciton quantum yields (QYs) in previous experiments. This chapter explores the creation of a long-lived photocharged state that can be formed because of the high intensity pulsed laser experiment. The dynamics of this state are determined and used to explain the previous variation. This paper also provides a method to avoid the creation of this photcharged state so that accurate MEG efficiencies can be determined and these results are given for PbSe QDs. This chapter was originally published in The Journal of Physical Chemistry C and is reproduced here with minor formatting changes with permission from reference 31.

The fourth chapter explores MEG efficiency in PbS and PbSSe alloy QDs and for the first time shows that a size dependence exists in the MEG efficiency of strongly confined lead chalcogenide QDs. Many theories predict this size dependence and finding proof of it lends validity to the MEG process. This size dependence is attributed to the amount of confinement

present in each quantum system, with PbSe showing more confinement than PbS due to the increased Bohr exciton radius found in PbSe.

The fifth chapter will focus on MEG in films of treated QDs. In order to make a QD solar cell, individual dots must be coupled together to allow transport through the film. To do this, the long organic ligands must be removed from the QD and replaced with shorter, more conductive ligands. These treatments change the electronic properties of the film and can dope the materials in different ways. This chapter examines the coupling between QDs in these films and how that affects the MEG efficiency. We find that while some treatments do not seem to affect the MEG yield, other treatments (notably 1,2-ethanedithiol) almost completely quench MEG. This chapter was originally published in Nano Letters and is reproduced here with minor formatting changes with permission from reference 32.

Chapter 2: Comparing Multiple Exciton Generation in Quantum Dots To Impact Ionization in Bulk Semiconductors: Implications for Enhancement of Solar Energy Conversion

2.1 Abstract

Multiple exciton generation (MEG) in quantum dots and impact ionization (II) in bulk semiconductors are processes that describe producing more than one electron-hole pair per absorbed photon. We derive expressions for the proper way to compare MEG in QDs with II in bulk semiconductors, and argue that there are important differences in the photophysics between bulk semiconductors and QDs. Our analysis demonstrates that the fundamental unit of energy required to produce an electron-hole pair is the bandgap energy. We find that the energy efficiency increases by a factor of 2 in PbSe QDs compared to bulk PbSe, while the competition between cooling and EHPM increases by a factor of 3. We demonstrate that power conversion efficiencies in QD solar cells exhibiting MEG can greatly exceed conversion efficiencies of their bulk counterparts, especially if the MEG threshold energy can be reduced toward twice the QD bandgap energy, which requires a further increase in the MEG efficiency. Finally, we discuss the research challenges associated with achieving the maximum benefit of MEG in solar energy conversion.

2.2 Introduction

Electron-hole pair multiplication (EHPM) occurs when more than one electron-hole pair (EHP) is produced by absorption of one photon with energy at least twice the semiconductor bandgap. In bulk semiconductors, EHPM is referred to as impact ionization, (II) a well known

phenomenon,[33,34] while in semiconductor nanocrystals, or quantum dots (QDs), EHPM is referred to as multiple exciton generation, MEG[1], carrier multiplication, CM[35], or direct carrier multiplication, DCM[36] to distinguish the phenomenon from II and highlight new proposed physics in quantum confined systems. In recent years, MEG has been reported in several QDs, such as PbSe,[1,35,37-39] PbS, [1,40] PbTe,[41] Si,[42] CdSe,[43-45] InAs[6,46], InP[47], and CdTe/CdSe core-shell QDs.[45] However, some authors report they cannot reproduce MEG in CdSe[48] and InAs[49,50] QDs, and for the lead chalcogenides, where MEG has been reported by all investigators, there is controversy concerning the value of the quantum yields (QY) as well the significance of MEG for improving the performance of photovoltaic cells. Some authors report QYs >> 1 for exciton formation in PbSe and PbS QDs,[1,4,32,35,37,38] while others have reported only small QYs (< 1.25).[39] These variations have been attributed to effects of surface chemistry on the exciton relaxation dynamics,[32,39] and in some cases to long-lived charging of the QDs caused by trapping of a photoexcited electron or hole at the QD surface leaving a delocalized hole or electron residing in the core (Chapter 3).[4] Extraneous effects such as charging can be reduced by flowing,[31] or stirring the sample[4] during the experiment and using low photon fluencies.

An enhancement in EHPM is expected in QDs over that achievable in bulk semiconductors due to beneficial quantum size effects, such as, relaxed momentum conservation, modified carrier-cooling rates, and enhanced Auger processes. In a recent report,[51] EHPM in bulk films of PbSe and PbS was measured using time-resolved THz spectroscopy and the QY, or number of electron-hole pairs produced per absorbed photon, were compared with previous reports of MEG in QDs of PbSe and PbS. The authors found that plots of the QYs of EHPM for the bulk semiconductors were equivalent or even larger than that reported for QDs for a given absolute photon energy. From that comparison, the authors concluded that EHPM processes are

not enhanced in QDs and EHPM processes are unlikely to significantly enhance solar energy conversion by boosting the photocurrent. In this report, we discuss what we claim is the appropriate way to compare MEG in QDs with II in bulk semiconductors. We show that plotting QY vs. hv/E_g (where E_g is the bandgap) provides information about the competition between producing multiple carriers and other energy relaxation channels. We present a rigorous derivation of the efficiency of EHPM, η_{EHPM} , whether for bulk semiconductors or QD samples, that allows for meaningful comparisons and show how η_{EHPM} is related both to the threshold energy needed to produce extra EHPs, hv_{th}, and the competition between EHPM and other relaxation channels. We find η_{EHPM} increases by ~2 in PbSe QDs compared to bulk PbSe. We discuss differences in the photophysics between MEG and II. Finally, we present thermodynamic detailed balance calculations, following the Shockley-Queisser analysis,[12,52,53] that demonstrate power conversion efficiencies in QD solar cells can greatly exceed that of their bulk semiconductor counterparts.

The recent report[51] on EHPM in bulk PbS and PbSe and a previous report on MEG in PbS and PbSe QDs[39], compare EPHM for bulk semiconductors and QDs on plots of QY vs. absolute photon energy (hv). Such a comparison is misleading, because for proper comparisons it is necessary to determine η_{EHPM} . The efficiency, η_{EHPM} , is defined as the minimum amount of energy required to produce an EHP (i.e. the bandgap), divided by the actual amount of energy required to produce an EHP, referred in the literature as the electron-hole pair creation energy ε_{EHPM} [54,55]($\eta_{EHPM} = E_g/\varepsilon_{EHPM}$). The fact that measurements of MEG QYs for PbSe and PbS QDs are at best equal to that found in the recent II measurements[51] when compared using hv scaling, does not imply an absence of quantum confinement effects or that EHPM is the same for QDs

and bulk. Too little is known about relaxation processes in QDs and the size-dependent MEG has not been sufficiently studied to support such a firm conclusion. Furthermore, QY data plotted vs. hv does not provide information about η_{EHPM}. When hv scaling is used, only the electron-hole pair creation energy, ε_{EHPM}, can be ascertained from the data; ε_{EHPM} is equal to inverse of the slope of QY vs. hv, $\left[\varepsilon_{EHPM} = \left(\Delta QY/\Delta hv\right)^{-1}\right]$. In contrast, as we will show below, the slope of QY vs. hv/E_g, is equal to the EHPM efficiency, $\eta_{EHPM} = \left[\Delta QY/\Delta\left(hv/E_g\right)\right]$. Thus, η_{EHPM}, is a measure of how well EHPM competes with other relaxation channels and provides a proper and meaningful comparison with respect to the photophysics of EHPM.

2.3 Discussion

2.3.1 EHPM Energy Considerations and Efficiency

A fundamental constraint for EHPM processes is the conservation of energy, and for systems with translational symmetry (bulk crystals) the conservation of momentum must also be satisfied. An energetic electon-hole pair, EHP^*, produced by absorption of a photon with sufficient excess energy above the bandgap, ΔE_g, can produce p additional EHPs. The EHPM process is described by the following scheme.

$$EHP^* \xrightarrow[EHPM]{} \left(p+1\right)e + \left(p+1\right)h \tag{2.1}$$

When EHP^* is produced by absorption of a photon with energy, $hv > E_g$, conservation of energy dictates that the total number of EHPs created, multiplied by their energy, must be less than or equal to the total input energy (energy of absorbed photons)

$$N(EHP)\cdot\varepsilon(e\cdot h)\le h\nu\cdot N_{photons} \tag{2.2}$$

where $\varepsilon(e\cdot h)$ is defined as the thermalized energy of an EHP (i.e. the bandgap). The inequality reflects the fact that some input energy is lost to heat. For photon energies greater than E_g and in the absence of EHPM, the excess energy is lost as heat. The energy loss per absorbed photon is $E_{loss}=\Delta E_{tot}=\left(h\nu-E_g\right)$. For EHPM, the excess energy must be greater than the electron-hole pair creation energy, $\Delta E_{tot}\ge\varepsilon_{EHPM}$. In the ideal case the efficiency equals one, $\eta_{EHPM}=1$, and the amount of energy needed to produce an additional EHP is the bandgap energy, $\varepsilon_{EHPM}=E_g$. Therefore, when the photon energy reaches $2E_g$ one additional EHP can be created utilizing all excess energy, thus, $E_{loss}=0$ at $h\nu=2E_g$. For photon energies exceeding $2E_g$, but less than $3E_g$, one additional EHP is formed and the rest is lost to heat, therefore, $E_{loss}=h\nu-2E_g$, which is the total lost energy after one EHPM event. At $h\nu=3E_g$, two additional EHPs can be produced with $E_{loss}=0$. Generalizing these observations, the total energy lost is $E_{loss}^{(m)}=h\nu-mE_g$,where m is the total number of EHPs allowed by energy conservation with a photon energy of $h\nu$, thus $m=\lfloor h\nu/E_g\rfloor$, where the operator, $\lfloor\ \rfloor$, denotes rounding down to the nearest integer. In general, the amount of energy loss, ΔE_{loss} is the total excess energy minus the number of EHPs multiplied by the energy needed to produce additional EHPs,

$$E_{loss}=\left(h\nu-E_g\right)N_p-pE_g=\left(h\nu-mE_g\right)N_{photons} \tag{2.3}$$
$$\text{for}\quad mE_g\le h\nu<(m+1)E_g$$

where N_p is the number of primary EHPs created by absorption of $N_{photons}$, p is the number of EHPs created by EHPM; $(p = m - 1)$. Solving for the quantum yield, $QY = \left(p + N_p\right)/N_{photons}$, we find $QY = m = \lfloor hv/E_g \rfloor$, and resembles a staircase that is shown as trace M_{max}, in Figure 2.3.1b.

For non-ideal cases, more energy than the bandgap is needed to produce an additional EHP, $\varepsilon_{EHPM} > E_g$, and this non-ideality is reflected in EHPM efficiencies less than one, $\eta_{EHPM} < 1$. Therefore, $p = 0$ for photon energies less than $E_g + \varepsilon_{EHPM}$ and, $p = 1$ for photon energies greater than $E_g + \varepsilon_{EHPM}$ but less than $E_g + 2\varepsilon_{EHPM}$. This can be generalized as above to find the maximum number of EHPs at a given photon energy.

$$\begin{aligned} E_{loss} &= \left(hv - E_g\right)N_p - p\varepsilon_{EHPM} \\ &= \left[hv - \left(E_g + \left(m' - 1\right)\varepsilon_{EHPM}\right)\right]N_{photons} \\ \text{for} \quad & E_g + \left(m' + 1\right)\varepsilon_{EHPM} \le hv < E_g + m'\varepsilon_{EHPM} \end{aligned} \tag{2.4}$$

where m' is the total allowed EHPs for the non-ideal case. Substituting $\varepsilon_{EHPM} = E_g/\eta_{EHPM}$ we find that $m' = \lfloor \left(hv/E_g - 1\right)\eta_{EHPM} \rfloor$, and therefore the maximum QY is,

$$QY_{\max} = \left\lfloor \left(\frac{hv}{E_g} - 1\right)\eta_{EHPM} \right\rfloor + 1 \tag{2.5}$$

Typically, experimental QYs for EHPM start at some energy threshold, hv_{th}, and increase linearly, rather than exhibiting the staircase features described above that leads to Equation (2.5). In these cases a phenomenological extension of Equation (2.5) can be made by

assuming that the energy loss is equal to $\Delta E_{loss} = h\nu_{th} - E_g$ for photon energies greater than $E_g + \varepsilon_{EHPM}$. Substituting into equation 4 and solving for QY we find,

$$QY = \left(\frac{h\nu}{E_g} - 1 \right) \eta_{EHPM} \tag{2.6}$$

By solving Equation (2.5) or (2.6) for when the QY ≥ 1, we find that the energy threshold, $h\nu_{th}$, is related to η_{EHPM}, and is,

$$h\nu_{th} = E_g + E_g / \eta_{EHPM} . \tag{2.7}$$

In terms of energy loss, Equation (2.5) assumes that there is no energy loss other than that contained in the efficiency term, while Equation (2.6) assumes a total loss of $E_{loss} = h\nu_{th} - E_g = E_g / \eta_{EHPM}$. Therefore we conclude that η_{EHPM} is obtained from slope of QY vs. $h\nu / E_g$.

2.3.2 EHPM Rates vs. Cooling rate

We also consider the competition between the rate of EHPM, k_{EHPM}, vs. alternative energy relaxation channels, such as cooling via phonon emission. Figure 2.3.1a shows a cascading kinetic scheme where the high-energy exciton either cools directly to the lowest state or produce a hot bi-exciton state, n_2^*. That state can either cool or undergo another EHPM event. The initially excited exciton eventually losses all of its excess energy. We do not include decay processes of the relaxed excitons such as Auger recombination and radiative recombination that we assume occur on longer timescales. The set of differential equations that describe the cascaded scheme shown in Figure 2.3.1 are,

$$
\begin{aligned}
\dot{n}_1^* &= -k_{cool} n_1^* - k_{EHPM} n_1^* + I_o \\
\dot{n}_1 &= k_{cool} n_1^* \\
\dot{n}_2^* &= k_{EHPM} n_1^* - k_{cool} n_2^* - k_{EHMP}^{(2)} n_2^* \\
\dot{n}_2 &= k_{cool} n_2^* \\
\dot{n}_3^* &= k_{EHPM}^{(2)} n_2^* - k_{cool} n_3^* - k_{EHPM}^{(3)} n_3^* \\
\dot{n}_3 &= k_{cool} n_3^* \\
&\vdots \\
\dot{n}_m^* &= k_{EHPM}^{(m-1)} n_{m-1}^* - k_{cool} n_m^* - k_{EHPM}^{(m)} n_m^* \\
\dot{n}_m &= k_{cool} \dot{n}_m^*
\end{aligned}
\tag{2.8}
$$

where I_0 is the photon fluence, n_1^* is the population of hot single exciton states, n_1 is the population of relaxed single exciton states, n_2^* is the population of hot bi-exciton states n_2 is the population of relaxed bi-exciton states, n_3^* is the population of hot tri-exciton states and n_3 is the population of relaxed tri-exciton states. In general, n_m^* is the hot *m*-exciton state and n_m is the cooled *m*-exciton state. The cooling rate is denoted k_{cool}, and the EHPM rates are denoted $k_{EHPM}^{(m)}$, where *m* is an integer. To find the QY we solve Equation (2.8) for the population of single, bi-, tri- and higher exciton states at times longer than EHMP and cooling,

$$
QY = \sum_{j=1}^{m'} j \cdot n_j \left(t > \tau_{EHPM}, \tau_{cool} \right) = \sum_{j=1}^{m'} j \cdot \frac{k_{cool} \prod_{i=1}^{j} k_{EHPM}^{(i-1)}}{\prod_{i=1}^{j} \left(k_{cool} + k_{EHPM}^{(i)} \right)}
\tag{2.9}
$$

where $k_{EHPM}^{(0)} = 1$. The maximum value of *m* is determined by the energy considerations discussed above. To use Equation (2.9) we need to know how k_{EHPM} and k_{cool} vary with excess energy. Keldysh found that for bulk semiconductors the EHPM rate follows,[56,57]

$$k_{EHPM} = \left(\frac{e^2}{4\pi\varepsilon} \right) \frac{m_e^*}{\hbar^3} \frac{I_c^2 I_v^2}{(1+2\gamma)^{3/2}} \frac{(h\nu - h\nu_{th})^2}{E_g^2} \tag{2.10}$$

where I_c and I_v are the overlap integrals between initial and final states in the conduction and valence bands, and $\gamma = m_e^*/m_h^*$ which are the effective masses in the conduction and valence bands. Now we need to know how k_{cool} varies with excess energy.

For bulk semiconductors the most important cooling relaxation channel is hot carrier cooling via phonon emission, k_{phonon}. The ratio of rates, k_{EHPM}/k_{phonon} is proportional to the ratio of the mean free path for phonon scattering, λ_{phonon} and the mean free path for EHPM, λ_{EHPM}, i.e., $k_{EHPM}/k_{phonon} \propto \lambda_{phonon}/\lambda_{EHPM}$. We can get an idea of the length scales by considering the behavior of free charge carriers in bulk semiconductors. The average distance a charge carrier travels prior to phonon scattering is equal to the velocity of the carrier multiplied by the average time between collisions, $\lambda_{phonon} = v\langle\tau\rangle$. λ_{phonon} is relatively independent of the kinetic energy of the charged carrier because the length scale for phonon scattering is determined by the properties of the lattice, so as v increases it is offset by a shorter $\langle\tau\rangle$. For bulk PbSe, λ_{phonon} can be estimated from the carrier mobility, and we find $\lambda_{phonon} \sim 67$ nm. In bulk semiconductors, λ_{EHPM} decreases with increasing carrier velocity (or excess kinetic energy),[58] corresponding to an increasing k_{EHPM}. In bulk PbSe, λ_{EHPM} has not been measured to our knowledge, however, for Si $\lambda_{EHPM} \sim 10$ nm[55] at a few eV above the bandedge and for GaAs, $\lambda_{EHPM} > 10$ nm for excess energies between 1 and 10 eV. [58] In accordance with the above observations, a Monte Carlo simulation of phonon cooling and impact ionization find the phonon relaxation rate to be independent of excess energy, while the II rate increased with increasing excess energy.[59] The

dimensions of QDs studied here are smaller than both λ_{phonon}, and λ_{EHPM}, of bulk materials indicating that EHPM and cooling in QDs are most likely different from bulk. Following Ridley[56] we parameterize k_{EHPM}/k_{cool} by the following expression,

$$k_{EHPM} = k_{cool} P \left(\frac{h\nu - h\nu_{th}}{h\nu_{th}} \right)^{s} \tag{2.11}$$

where the factor P determines whether the EHPM onset is hard or soft, for P>>1 the onset is hard, and P<1 the onset is soft. The exponent s in Equation (2.11) was found to be 2 in the original Keldysh treatment. However, that treatment was for an ideal semiconductor, in more detailed treatments, s can vary between 2 and 5. In our treatment we allow both s and P to be adjustable parameters. We now define an efficiency, η'_{EHPM}, based on the threshold parameter, P, that captures the competition between the k_{EHPM} and k_{cool},

$$\eta'_{EHPM} = \frac{P}{1+P} \tag{2.12}$$

where we use the prime to distinguish η'_{EHPM} from η_{EHPM} defined above in terms of ε_{EHPM}. The relationship between η'_{EHPM} and the energy threshold is the same as we found before but now each EHPM event has it's own energy threshold given by,

$$h\nu_{th}^{(m)} = E_g \left(1 + m/\eta'_{EHPM}\right) \tag{2.13}$$

where $k_{EHPM}^{(m)}$ is zero below $E_{th}^{(m)}$ and $k_{EHPM}^{(m)} = k_{cool} P \left[\left(h\nu - h\nu_{th}^{(m)} \right) / h\nu_{th} \right]^{s}$ above $h\nu_{th}^{(m)}$.

In Figure 2.3.1b we show plots of the QY from Equation (2.9) for various values of P (with s=2) and note the values of η'_{EHPM}. We vary P from 10,000 to 0.1, at P=10,000, η'_{EHPM} =1,

and EHPM dominates over cooling. For this scenario we recover the staircase behavior for an ideal behavior where Equation (2.3) gives the total energy loss. At P = 1, η'_{EHPM} =0.5, we find a roughly linear increase of the QY with $h\nu/E_g$, the onset however, is not as sharp as that predicted from Equation (2.6). For QY values less than ~150% and for P < 10, $k_{cool} > k_{EHPM}$, and QY increases ~quadratically with $h\nu/E_g$. At a QY = 150%, $k_{cool} \approx k_{EHPM}$, this can been seen by substituting $k_{cool} = k_{EHPM}$ and considering the first two terms of Equation (2.9), $QY = k_{cool}/\left(k_{cool} + k_{EHPM}^{(1)}\right) + 2k_{EHPM}^{(1)}/\left(k_{cool} + k_{EHPM}^{(1)}\right)$. The QY in this energy range increases approximately linear with $h\nu/E_g$ with a slope determined by P and s.

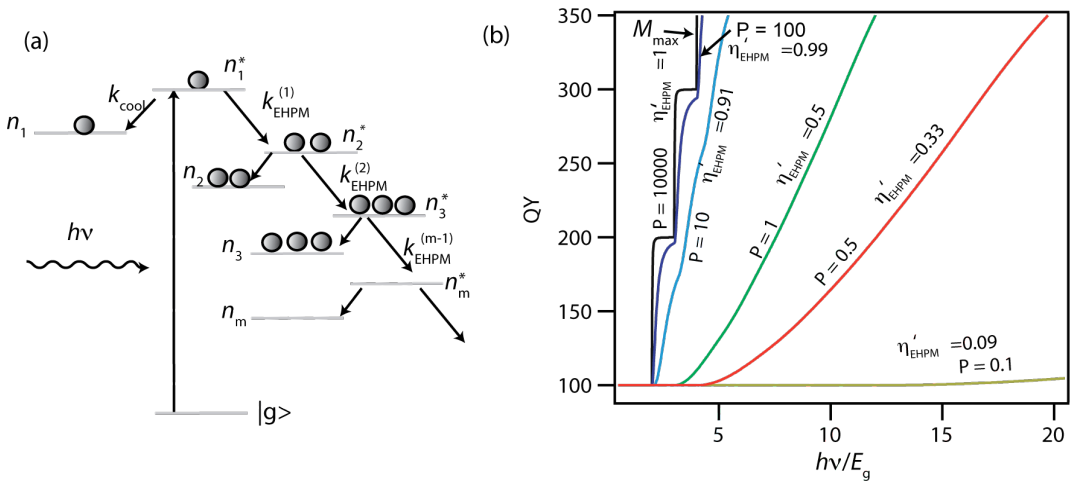

Figure 2.3.1: MEG Efficiency Calculations.
Part (a) cascade scheme for EHPM considered here. A high energy photon creates an exciton with excess energy, n_1^*. The hot exciton can lose energy by cooling or EHPM to form either n_1 or a hot biexciton, n_2^* and so on. Part (b) shows plots of Equation (2.11) for different values of P, η'_{EHPM} is shown at each P value.

2.4 Data Analysis

Figure 2.3.1 displays recent MEG QY data reported in reference 31 for 3 samples of different sizes PbSe QDs (filled brown squares). We employ a 1 mm flow cell to flow our samples at 150 ml/min during the transient absorption experiment. We also plot recent data reported in reference 4 from the Los Alamos group where their samples were stirred rather than flowed. The good agreement between these two data sets provides confidence in our reported results. EHPM QYs for bulk PbSe (filled black squares) and bulk PbS (open circles) are plotted and reproduced from reference 51 These data points were measured using a time-resolved THz experiment that is sensitive to the total number of carriers produced by the excitation pulse. Equation (2.6) was fit to each data set with only one adjustable parameter, η_{EHPM} , to obtain both the slope and hv_{th} and are shown as dotted lines. The solid lines are the best-fit lines using Equation (2.9) where *P* and *s* are allowed to vary. The fits using Equation (2.9) are slightly better because the predicted onset is not as abrupt. This appears to be more important for the QD samples than the bulk data. We report the best-fit parameters in Table 2.4.1 and tabulate η'_{EHPM} , hv_{th} , and hv'_{th} .

The efficiency, η_{EHPM} , is clearly better for the PbSe QD samples than for the bulk PbSe. We find η_{EHPM} increases from 0.19 to 0.41 in the QD samples (a factor of >2), while P increases from 0.45 to 1.5, an increase of >3. In accordance with our discussion above, hv_{th} decreases from $4.2\,E_g$ to $2.7\,E_g$. Through the analysis presented here comparing EHPM as a function of hv/E_g is more meaningful than hv . The hv/E_g scaling provides a clear way of comparing η_{EHPM} while the hv scaling does not. Furthermore, when considering data using the hv scaling the threshold values can be confusing and or obscured because there does not appear to be any correlation between the slope (or electron-hole pair creation energy) and hv_{th} . However, the

correlation is clearly visible with the $h\nu/E_g$ scaling. For example, considering the bulk PbS data we see it takes ~ 4.3 E_g for EHPM to begin and each new EHP occurs at each additional 3.3 E_g, in accordance with η_{EHPM} =0.29.

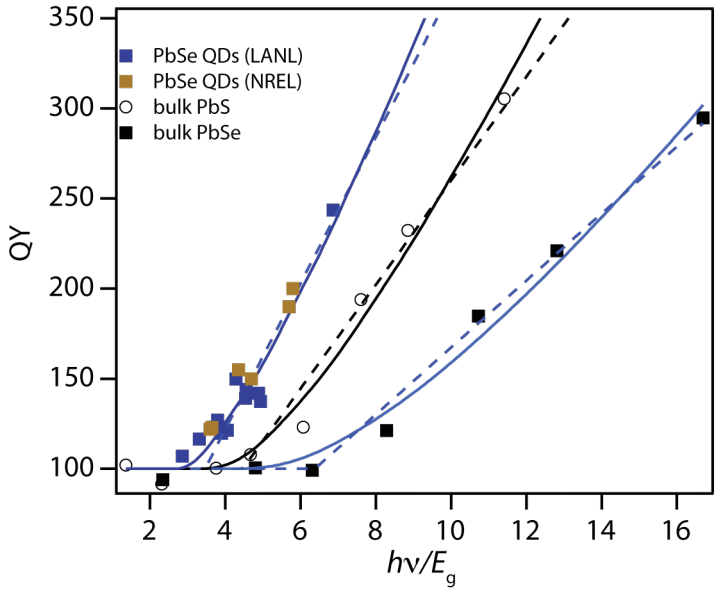

Figure 2.4.1: MEG and II Efficiency
(a) QY vs $h\nu/E_g$ for PbSe QD samples measured at LANL and reported in reference 4 (blue squares), and PbSe QDs measured at NREL and reported in reference 31 (brown squares). EHMP QYs for bulk PbSe and bulk PbS are reproduced from reference 51. The dotted lines are a linear-least squares best fit of Equation (2.6) to the data and the solid lines are Equation (2.9). The best-fit parameters are reported in Table 2.4.1.

Table 2.4.1: Best-fit parameters for lines shown in Figure 2.4.1

	η_{EHPM}	$h\nu_{th}$	η'_{EHPM}	P	s	$h\nu'_{th}$
Bulk PbSe	0.19	6.5 E_g	0.31	0.45	2.5	4.22 E_g
Bulk PbS	0.29	4.4 E_g	0.45	0.83	2.6	3.22 E_g
QD samples						
PbSe QDs	0.41	3.4 E_g	0.6	1.5	2.2	2.7 E_g

2.4.1 EHPM Energy Threshold Considerations

In the above analysis, we find a relationship between η_{EHPM} and hv_{th}/E_g. This relationship implies that hv_{th} is inextricably linked to η_{EHPM}. However, the link between the η_{EHPM} and hv_{th} can be broken if other factors besides the efficiency help determine hv_{th}. For example, if the relationship between ε_{EHPM} and the bandgap energy is $\varepsilon_{EHPM} = AE_g + B$ where B is the related to hv_{th}.[54,55,60] We could also consider a scenario where ε_{EHPM} is not a linear function but varies with the amount of excess energy so that η_{EHPM} increases with increasing energy, again plotting QY vs. hv_{th}/E_g will provide η_{EHPM}.

There are at least three possible contributions to hv_{th}; (1) conservation of energy, (2) conservation of momentum, and (3) η_{EHPM}, as discussed above. Energy conservation dictates that $hv_{th}/E_g \geq 2$; however, in a bulk semiconductor, $\Delta k = 0$ absorption selection rules increases hv_{th}. The excess energy in the conduction band is $\Delta E_e = \left(hv - E_g\right)\left(1 + m_e/m_h\right)$ and $\Delta E_h = \left(hv - E_g\right) - \Delta E_e$, where m_e is the effective mass of the electron and m_h is the effective mass of the hole. For parabolic bands, $m_e \approx m_h$, the situation for PbS and PbSe, and $hv_{th}/E_g \approx 3$ on energy conservation arguments alone. However, the bands may not be parabolic; hv_{th} depends upon the detailed band structure and there is a distribution of excess energies populated by absorption.[61] There may also be weak 2nd order transitions involving a phonon that relaxes the $\Delta k = 0$ selection rule.

Crystal momentum must be conserved for systems with translational symmetry and this additional constraint increases hv_{th} over the energy conservation limit for bulk semiconductors. The amount of increase in hv_{th} depends on the band structure, positions of split-off bands,

indirect vs. direct transitions, and other details that pertain to the semiconductor of interest. A review of the most common situations found in semiconductors has been tabulated in reference 34. For the case of isotropic bands the excess energy in the conduction or valence band is given by

$$\Delta E_e = \frac{(2m_e + m_h)}{m_e + m_h} E_g \qquad (2.14)$$

where ΔE_e is the excess kinetic energy necessary in the initiating electron. For PbS and PbSe the above condition results in an excess energy of $3E_g/2$, $E_g/2$ above the energy conservation limit. Therefore, energy and momentum constrain $hv_{th}/E_g \approx 4$ for PbSe and PbS. In QDs, momentum is no longer a good quantum number since a crystal lattice only exists for a few nanometers and therefore the momentum conservation limit is relaxed, and for PbSe QDs, hv_{th} has been observed to be $\sim 3E_g$ (reported here as $2.7E_g$), well below the momentum conservation limit. Thus one major advantage of QDs is the possibility to decrease hv_{th} below the momentum conservation limit defined for bulk systems.

2.4.2 Photophysics of Hot Electrons and Quantum Confinement Effects

In QDs there are at least three fundamental properties that are modified due to quantum confinement and affect the EHPM process. (A) Crystal momentum is no longer a good quantum number. For (A), there are three factors that can affect hv_{th} related to crystal momentum. (1) Absorption selection rules are modified; (2) conservation of crystal translational momentum is relaxed, allowing hv_{th} to be less than that required by momentum conservation. In fact, we find hv_{th} in QDs of PbSe is lower than that allowed by momentum conservation in bulk PbSe, and (3) single and mutli-excitonic states can be coupled through the Coloumb operator to form a superposition of states.[62] Such coupling is not possible in bulk systems with well-defined

momentum. (B) The discrete structure of semiconductor QD energy bands, due to quantum confinement and intimate control over surface states and surface ligands can be used to modify carrier relaxation rates and thereby increase *P*. Intimate control over surfaces and interactions is a research challenge rather than *a priori* a bad omen. (C) Increased Coulombic coupling between excitons in QDs increases Auger-related processes like MEG.

Our analysis so far does not consider whether k_{EHPM} is enhanced in QDs over bulk or whether k_{cool} decreases, and quantum confinement may effect both k_{cool} and k_{EHPM}. As we noted earlier the length scales for both EHPM and cooling in bulk PbSe are larger than the QD diameter, therefore we expect some dependence of these processes with size. If no new physical processes are invoked then we would expect the surfaces of the QDs to dominate these relaxation pathways. The photoexcited carrier should reach the QD surface balistically, and both k_{cool} and k_{EHPM} could increase. The resulting QY would depend on whether k_{EHPM}/k_{cool} increased, decreased, or remained constant. However, size effects do introduce new relaxation pathways that are not found in corresponding bulk semiconductors. One of the arguments for enhanced EHPM in QDs is the sparse density of states that can slow or inhibit phonon mediated relaxation (referred as the phonon bottleneck).[2,15] The presence of the phonon bottleneck is masked by enhanced Coulombic coupling between the electron and hole wavefunctions providing an Auger-like relaxation channel[18] that relies on a large difference in m_e and m_h. Slowed cooling has been observed in QD systems where the electron and hole are separated,[23] the effective masses are similar,[63] or surface relaxation channels are suppressed[64], combining these approaches, the 1P to 1S cooling was slowed to ~ 1ns.[65] However, the majority of hot carrier relaxation studies have used low excess energies, while MEG measurements are performed at high excess energies. One of the criticisms of enhanced MEG in QDs is that the density of states at these high excess

energies is sufficiently dense to allow fast relaxation via phonon emission (the absorption spectra of QDs approach that of bulk at high excess energies[66]). However, we argue that it is the relative lengths scales that are important, and as we have shown the ratio increases for QDs. It stands to reason that QD surfaces play a significant role in all carrier relaxation processes at these high energies. Recent theoretical treatments of QD-ligand interactions demonstrate that the QDs cannot be considered as isolated semiconductors within very high barrier confinement levels.[67] A significant research challenge is to better understand these high excess energy states and to determine what factors may influence MEG vs. other relaxation channels and thereby learn how to further increase *P*.

Based on our arguments above EHPM should follow fundamentally different physics in QDs than in bulk semiconductors, and the theoretical model for MEG developed by Efros, Shabaev, and Nozik [62] shows how the photophysics governing MEG in QDs is new and different from EHPM in bulk. The strong Coulomb coupling of multiple excitons driving MEG in QDs is not present in the bulk. Other models for MEG/CM[68,69] also show different physics for bulk semiconductors compared to QDs. For example, in the Klimov model, CM occurs through excitation of virtual states that are transferred to biexciton states via intraband transitions. η_{EHPM} is higher in QDs because of enhanced intraband transition oscillator strengths in QDs vs. bulk semiconductors. Zunger et. al. use an impact ionization approach to calculate enhancements in EHPM in QDs due to a higher density of final states.[70]

2.4.3 Implications for Improved Solar Energy Conversion

Concerning the issue of whether MEG can enhance solar power conversion efficiencies, we now demonstrate that solar cells produced from QDs can have much higher power conversion efficiencies than their bulk counterparts. The results are based on Shockley-Queisser (SQ)

Detailed Balance calculations and are summarized in Figure 2.4.2. We[53] and Klimov[71] have previously conducted thermodynamic efficiency calculations comparing bulk semiconductors and QDs using the approach, and we extend theses calculations for various values of hv_{th} and η_{EHPM}. In Figure 2.4.2, curve 6 (black solid line) is the conventional Shockley-Queisser (SQ) calculation with just 1 EHP created per photon at the bandgap; curve 1 (solid red curve) assumes the maximum multiplication energetically allowed and is based on $M_{\max}$. Curve 2 (solid green line) is based on $hv_{th} = 2E_g$ followed by creation of one extra exciton created per E_g (defined as the L2 characteristic); curve 3 (solid blue line) is based on a threshold of 2.5 E_g with slope defined in Equation (2.6), $\eta_{EHPM} = 1$; curve 4 is based on a threshold of 3 E_g (defined as the L3 characteristic); curve 5 is based on a threshold of 4.5 E_g with $\eta_{EHPM} = 0.19$ (defined as the L5 characteristic and is the experimental bulk characteristic for PbSe, see Figure 2.4.1b). For each LX case E_g/η_{EHPM} is lost to heat as discussed above (Equation (2.6)). Our analysis suggests that the slope has a smaller effect on power conversion efficiency than does hv_{th}. Thus identifying QD systems where hv_{th} can be lowered (also implying a higher η_{EHPM}) is imperative.

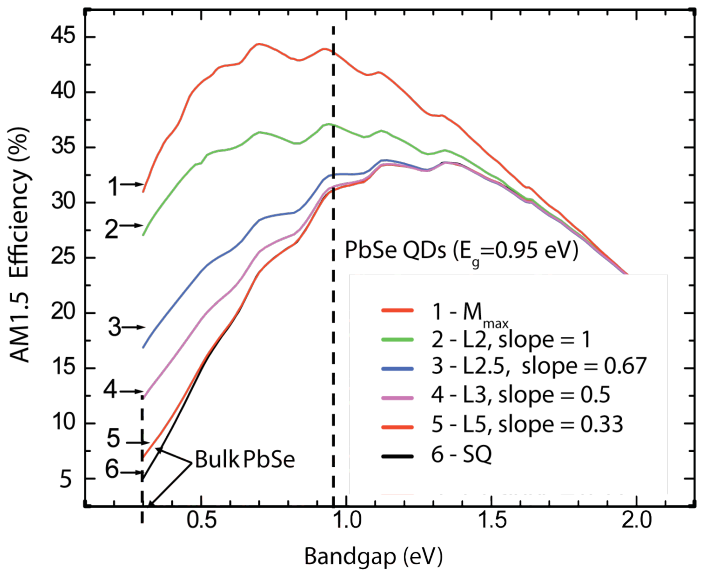

Figure 2.4.2: Solar Cell Efficiency Utilizing MEG Photovoltaic PCEs at AM1.5 vs bandgap for various characteristics of MEG QY. Curve SQ is the Shockley-Queisser limit, and curves L2, L2.5, L3, L5, and M_{max} are defined in the text.

As seen in Figure 2.4.2, the maximum thermodynamic conversion efficiency of ~ 5% for bulk PbSe is only marginally enhanced when the experimentally measured EHPM is included. Thus, EHPM in bulk PbSe cannot produce a significant enhancement of conversion efficiency. In contrast, for PbSe QDs with a quantized bandgap of 0.95 eV, the maximum thermodynamic conversion efficiency is 31% for the SQ calculation, 37% for the L2 characteristic (solid green line), 32% for the L3 characteristic (solid purple line), and 42% for the $M_{\max}$ characteristic (solid red line). These calculations show that PbSe QDs will always have a much higher theoretical conversion efficiency compared to bulk PbSe (by factors ranging from 2.7 (L3 characteristic) to 3.5 ($M_{\max}$ characteristic)). The calculated conversion efficiencies also show that the maximum possible efficiency for present QDs (L3 characteristic) is barely enhanced compared to the SQ efficiency (32% vs 31%, respectively). However, if hv_{th} can be reduced to $2E_g$ (L2 characteristic), the maximum efficiency is increased to 37%, and if the MEG QY characteristic can become staircase-like (M_{max}), the maximum conversion efficiency increases further to 42%. All these scenarios represent major increases of thermodynamic conversion efficiencies for PbSe QD solar cells compared to bulk PbSe solar cells. For MEG thresholds that are close to $2E_g$, the maximum conversion efficiency can be greatly enhanced over the SQ limit (~ a 19% relative increase for L2 and ~ a 35% relative increase for M_{max}). We note that an M_{max} characteristic has been reported for MEG in the photocurrent measured in single single-walled carbon nanotubes (SWCNT), where after a photon energy threshold of $2E_g$ was reached, stepwise increases in photocurrent were measured at each subsequent increase of one E_g of applied voltage to the SWCNT p-n junction.[72] The research challenge for MEG in QD-based solar cells is to find materials and conditions that produce L2 and ultimately M_{max} MEG characteristics. Recent efforts towards producing efficient solar cells utilizing Pb-chalcogenide QDs as the active

element show V_{oc}'s that are higher than possible for a solar cell made from a bulk Pb-chalcogenide.[73] The higher bandgap and resulting higher Voc attainable with QDs result in a higher PCE as seen in Figure 2.4.2. The higher EHPM efficiency in QDs vs. bulk semiconductors allows for a lower hv_{th} and thus drives the maximum possible PCE higher than the SQ limit for a bulk semiconductor of that given bandgap.

2.5 Conclusions

We have shown that the correct way to compare EHPM processes between semiconductor QDs and bulk semiconductors is to plot the QY vs. hv/E_g as this provides a direct determination of the EHPM efficiency, η_{EHPM} , and allow for determination of the relative contributions of EHPM and competing relaxation channels η_{EHPM} . We show that there are large increases in theoretical thermodynamic photovoltaic conversion efficiencies for solar cells based on QDs compared to those based on bulk semiconductors. In contrast to previous publications,[39,51] we present data and detailed analyses in support of our belief that there are fundamental differences in the photophysics between EHPM processes in QDs and bulk semiconductors, in addition to major differences in theoretical solar conversion efficiency. The largest benefit to solar energy conversion would be a lowering of the photon energy onset for MEG, producing a staircase characteristic of QY vs hv/E_g. For non-ideal cases, the energy onset relative to the band gap must be between 2 and 2.5 E_g to have the greatest impact. We argue that the unique properties of QDs allow for lower threshold energy and higher η_{EHPM} . One theoretical study[74] surveyed 12 QD systems to determine which could produce an onset close to $2E_g$ and more such studies, both theoretical and experimental are needed along these lines.

Chapter 3: Flowing verses Static Conditions for Measuring Multiple Exciton Generation in PbSe Quantum Dots

3.1 Abstract

Recent reports question the validity of pulsed fs-laser experiments for measuring the photon-to-exciton quantum yields (QYs) that result from multiple exciton generation (MEG). The repetitive nature of these experiments opens up an alternative relaxation pathway that may produce artificially high results. We present transient-absorption (TA) data for 4.6 nm and 6.6 nm diameter PbSe quantum dots (QDs) at a variety of pump photon energies. The data are collected under laminar flow conditions with volumetric flow rates ranging from 0 to 150 ml/min (resulting in Reynolds numbers up to 460). The results are modeled with a spatially resolved population balance of generation, recombination, convective replacement, and accumulation of long-lived excited QDs. By comparing the simulations and experiments, the steady-state population of the long-lived QD-excited states and their kinetics are determined for different experimental conditions. We also improve upon reported photon-to-exciton QYs for PbSe QDs. We find differences in the observed TA dynamics between flowing and static conditions that depend upon photon fluence, pump photon energy, and quality of the QD surfaces. For excitation energies below 2 E_g, independent of QD size or photon fluence, we observe no flow rate dependence in the TA dynamics. At excitation energies of $h\nu > 3\,E_g$, we observe differences between static and flowing conditions that are most pronounced for high photon fluences. At 3.7 E_g and for 4.6 nm PbSe QDs we find a QY of 1.2 ± 0.1 and at 4.5 E_g the QY is 1.55 ± 0.05. With 6.6 nm QDs excited at 4.7 E_g we observe no difference between static and flowing conditions and find a QY of 1.61 ± 0.05. We also find that by treating the surface of QDs, we can decrease

the charging probability ($P_g \approx 5 \times 10^{-5}$) by a factor of 3-4. The observed variations suggest that different QD samples vary regarding their susceptibility to the creation of long-lived states.

3.2 Introduction

Multiple exciton generation (also called carrier multiplication) is a process by which a single high-energy photon, with energy ($E_{ph} = h\nu$) at least twice the bandgap $\left(h\nu \geq 2\, E_g\right)$, can produce multiple electron-hole pairs (excitons) in semiconductor nanocrystals (also called quantum dots (QDs)). MEG has been studied in several QD materials including PbSe,[1,4,35,37-39,75] PbS,[1,40] PbTe,[41] Si,[42] CdSe,[43,44] InAs[6,46] CdSe/CdTe core/shell type II hetereostructures[45] and InP.[47] Two recent studies[72,76] on semiconducting single-walled carbon nanotubes have also reported efficient MEG and provide a promising material for future work. All of the studies involving lead chalcogenides have reported QYs>1. However, the reported QYs vary for similar QD sizes and for similar photon excitation energies.[4,39] In this work we provide a partial explanation for the different MEG results.

In typical MEG measurements, the photon-to-exciton quantum yields (QYs) are deduced by measuring the ratio of the transient bleach (reduction of interband absorption), induced absorption (increased intraband absorption), or emission intensity, at early pump-probe delay times to the respective signal at long pump-probe delay times. The signal at early pump-probe delays is proportional to the number of excitons produced by the laser pulse while at long delay times it is proportional to the total number of QDs excited by the laser pulse.[3,77] The long pump-probe delay time is chosen to be at least 3 times the bi-exciton lifetime so that while very few single-excitons have decayed, all multi-excitons have decayed. This ratio, R_{pop}, is therefore proportional to the average number of excitons created within each excited QD. Multiple

excitons within a QD decay efficiently via a non-radiative Auger multi-particle interaction, that scales linearly with the volume of the QD.[3,16,35,42] By reducing the photon fluence of the excitation pulse, we enter a regime where the average excitation level averaged over the ensemble solution of QDs is less than 0.1. In this regime, only 1 in 10 QDs absorb photons during a single excitation pulse and of those that absorb a photon, less than 5% absorb more than one. If $R_{pop} > 1$ for these low photon fluences, this implies that multiple-excitons were produced per absorbed photon. There are three experimentally measured features that provide strong evidence for the direct production of multiple-excitons per absorbed photon. (1) R_{pop} increases above one with increasing photon energy after exceeding some energy threshold and is one below that threshold. (2) The time constant corresponding to the increasing R_{pop} is equivalent to that of the bi-exciton lifetime, measured in a separate experiment with pump photons below the ideal MEG threshold ($h\nu < 2\ E_g$) and by increasing the pump fluence so that on average each QD absorbs more than 1 photon. (3) The energy threshold for MEG appears to correlate with QD material. Mechanisms other than MEG must be able to account for these observations.

Recently, McGuire et. al.[4,75] proposed that due to the repetitive nature of the experiment (in our case, the excitation laser repetition rate is 500 Hz), a steady state population of photocharged QDs can be established, through a low probability photoionization event, if the lifetime of the photocharged QD is longer than the time between excitation pulses (2 ms). The proposed scheme is shown in Figure 3.2.1, in the following the various *n's* refer to the population of various states and the γ's represent transition rates between states. Unexcited QDs (labeled n_0) are excited to n^*, a hot-exciton produced by absorption of a photon with $h\nu > E_g$. There may be numerous pathways for n^* to relax; the hot-exciton may cool to the

bandgap (γ_{cool}) via processes that do not involve MEG, creating a single-exciton state, n_1, at the bottom of the conduction band, or the hot-exciton may undergo MEG (γ_{MEG}) to create two or more excitons (n_2). The mechanism for the MEG process is unclear, but for simplicity, we represent it as a two state process with a hot-exciton intermediate. An alternative pathway, with rate γ_g, produces a long-lived state where either the electron or hole is removed from the core of the QD (this is labeled as n_T). QDs in the n_T state accumulate during the experiment because their lifetime exceeds that of the laser repetition rate. For simplicity, we will refer to this state as a photocharged QD, but as is discussed later, there is not enough information available to determine the exact nature of this state. It is unlikely that it is a fully ionized species, but instead, a dipole formed by the charged QD core and the trapped charge on the surface or ligand. If a QD in the n_T state absorbs another photon from the next laser pulse, a trion-like state (labeled n_{2T}) is produced. The n_{2T} state undergoes a non-radiative Auger-recombination (γ_{trion}) process that may have similar dynamics to bi-exciton recombination. Such a process could produce a similar dynamical signature, that otherwise is ascribed solely to the creation of multiple-excitons by a single photon, leading to an artificially high MEG yield.[4,75] This alternative pathway, can be avoided by not allowing QDs to be exposed to multiple laser pulses either by stirring, or in the case of the results presented here, carefully flowing the QD solution with a well-defined flow profile during the laser experiment.

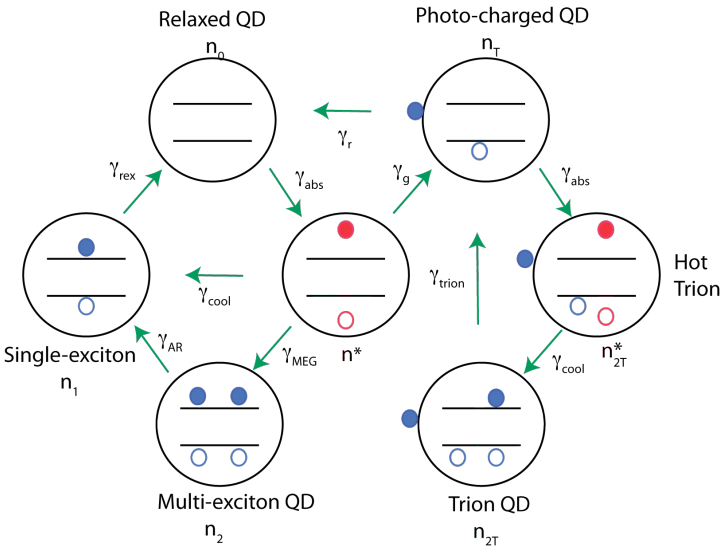

Figure 3.2.1: Photocharging Meachanism

Unexcited QDs (n_0) are excited to n^*, a hot-exciton produced by absorption of a photon with $h\nu > E_g$. The hot-exciton may relax by cooling to the bandgap (γ_{cool}), creating a single-exciton state (n_1), undergoing MEG (γ_{MEG}) to create two or more excitons (n_2), or producing (γ_g) a long-lived state where either the electron or hole is removed from the core of the QD (n_T). When re-excited, a trion state (n_{2T}) can be created, before decaying non-radiatively (γ_{trion}) back to the trap state (n_{2T}).

3.3 Experimental

3.3.1 Methods

Both 4.6 nm and 6.6 nm PbSe QDs (0.84 eV and 0.66 eV first exciton respectively) were synthesized according to a standard pre-published preparation.[78] To make the $Cd(Oleate)_2$ treatment, a mixture of 1.5g CdO, 8.05 g Oleic Acid and 17.4 g octadecene (ODE) were heated to dissolve CdO. Once cooled, approximately 20 mg of this solid was added to a tetrachloroethylene (TCE) solution with 25 mg PbSe.[79] This yields a ~20:1 molar ratio of PbSe to Cd. The interband bleaching of these QD solutions were probed using transient absorption (TA) (the experimental apparatus has been described previously and in the introduction[3,32,80]). The 4.6 nm PbSe QDs were excited with 330 nm, 400 nm and 800 nm light corresponding to ~4.5 E_g, ~3.7 E_g and ~1.8 E_g while the 6.6 nm QDs were excited with 330 nm, 400 nm and 1300 nm light

corresponding to ~5.7 E_g, ~4.7 E_g and ~1.5 E_g. For the smaller QDs, these experiments were done with and without the $Cd(Oleate)_2$ treatment while the larger QDs were only studied with a cadmium surface treatment. The $Cd(Oleate)_2$ treatment blue shifted the first exciton peak by ~10-20 nm and the samples were always probed at the band edge maximum. Excitation wavelengths below the MEG threshold ($h\nu < 2\ E_g$) were used to experimentally determine single and bi-exciton lifetimes. During TA experiments, the QD solutions were flowed through a quartz flow cell, with a channel 2 mm thick (L_z) by 10 mm wide (L_y) by 35 mm long (L_x), with either a peristaltic pump or a syringe pump depending on the flow rate needed. Dimension and flow conditions were chosen such that the flow was laminar (Reynolds number less than 1400) resulting in a well-defined unidirectional parabolic flow profile found from solving the Navier-Stokes equation for pressure driven flow between two parallel plates with no-slip boundary conditions. The Reynolds number $\left(\mathrm{Re} = \frac{\rho v L_z}{\mu}\right)$ was calculated using the density (ρ) and dynamic viscosity (μ) of TCE, approximately 1.622 g/cm^3 and 0.0089 g/cm-s). The average velocity (v) and cell thickness were used to calculate *Re*. The peristaltic pump was used for faster flow rates and was calibrated at two different flow rates: 40 mL/min (*Re* = 121) and 150 mL/min (*Re* = 456) by timing the flow of a known volume between two beakers at different settings. The pump spot size was 1.0 mm in diameter while the probe spot size was less than 150 μm, and both were located in the center (with regard to length and width) of the flow cell to minimize any end-effects. The width of the channel at the inlet and outlet are also tapered to reduce end-effects. As a result, the volume of the cell was 0.6 ml (slightly less than the rectangular dimension).

3.3.2 Transient Absorption and population dynamics

In these experiments, the TA signal is the difference in intensity of a transmitted pulse with and without photoexcitation divided by the transmitted probe pulse without photoexcitation.

$$\frac{\Delta T\left(\tau_p\right)}{T} = \frac{J^*_{probe}\left(\tau_p\right) - J_{probe}}{J_{probe}} \tag{3.1}$$

where J_{probe} is the transmitted probe fluence measured while the pump beam is blocked and J^*_{probe} is the transmitted probe fluence measured at a pump-delay time τ_p from the pump pulse. Beer's law states that the transmission of light through an element dz is linearly proportional to the absorption cross section at the probing wavelength, σ_{probe}, the intensity of the incident light, J_{probe}, and the difference in the ground and excited states,

$$dJ_{probe} = -\sigma_{probe} J_{probe}\left(n_0 - n_{ex}(z,\tau_p) - \frac{1}{2} n_T(z,Q)\right) dz \tag{3.2}$$

where σ_{probe} is the absorption cross section at the first exciton transition and n_0 is the density of states at the first exciton transition. Therefore, $n_0 = 8N_{QDs}$, because of the eight-fold degeneracy of the first exciton transition in PbSe.[81] N_{QDs} is the concentration of quantum dots in number per mL, $n_{ex}\left(z,\tau_p\right)$ is the density of excited states induced by the pump pulse at pump-probe delay time, τ_p, and position along the beampath z, and $n_T\left(z,Q\right)$ is the density of photocharged states at position z and volumetric flow rate Q. We assume here that the contribution to the bleach from photocharged QDs is ½ because the excited exciton state is half occupied. However, the exact value of the bleach contribution will not change our results because the TA experiment subtracts off this contribution through the measurement of a

pulse. We can solve for J^{*}_{probe} and J_{probe} to yield:

$$J^{*}_{probe}\left(\tau_p\right) = J^{0}_{probe}\exp\left(-\sigma_{probe}\int_0^{L_z}\left(n_0 - n_{ex}\left(z,\tau_p\right) - \frac{1}{2}n_T(z,Q)\right)dz\right) \tag{3.3}$$

$$J_{probe} = J^{0}_{probe}\exp\left(-\sigma_{probe}\int_0^{L_z}\left(n_0 - \frac{1}{2}n_T(z,Q)\right)dz\right) \tag{3.4}$$

where L_z is the thickness of the flow cell channel and J^{0}_{probe} is the fluence at the front of the cell. The pump pulse induces a spatially varying population of excited states that at early pump-delay times, before Auger recombination (and at not too high of pump fluences), obeys Beer's law; the distribution decays exponentially along the beam path in the flow cell.

$$n_{ex}\left(z,\tau_p < \tau_{AR}\right) = J^{0}_{pump}\sigma_{pump}N_{QD}QY\exp\left(-\sigma_{probe}N_{QD}z\right) \tag{3.5}$$

n_{ex} contains terms for single, n_1, and multiple-excitons, n_2, as well as terms for trions, n_{2T}, and possibly higher charged multiplicities as well, and QY is the photon-to-exciton quantum yield. We neglect here contributions from the hot-exciton, n^{*}, which can induce a Stark shift in the first exciton transition energy level at early delay times.[1] We do not consider here the saturation of the TA signal that occurs at higher multiplicities because for MEG measurements, it is the low photon fluence limit that is of primary interest. The appendix shows how Equation (3.5) was modified to include saturation of the 1S exciton level and a future publication will deal with the saturation behavior and Poisson statistics in PbSe QDs. We do show here how the TA results can depend weakly on the optical density, OD_{pump}, at the pump wavelength. Inserting Equation (3.5) into Equation (3.3) and solving we find:

$$J^{*}_{probe}(\tau_p < \tau_{AR}) = J^{0}_{probe}\exp\left\{-\sigma_{probe}8N_{QD}\left[L_z - \frac{b_T}{16N_{QD}} - \frac{QYJ^{0}_{pump}}{8N_{QD}}\left[1-\exp(-\sigma_{pump}N_{QD}L_z)\right]\right]\right\} \tag{3.6}$$

where $b_T = \int_0^{L_z} n_T\left(z\right)dz$ and the non-photoexcited case is,

$$J^{*}_{probe} = J^{0}_{probe}\exp\left\{-\sigma_{probe}8N_{QD}\left(L_z - \frac{b_T}{16N_{QD}}\right)\right\} \tag{3.7}$$

The spatial distribution of $n_{ex}\left(z,\tau_p\right)$ at longer pump-delay times can deviate from the simple exponential behavior described in Equation (3.5) because those QDs that have absorbed more than one photon undergo Auger recombination, so that only single-exciton states remain. Furthermore, if a charged QD absorbs a photon to produce a trion-like state, that will also undergo non-radiative Auger recombination. We now separate out the distribution of excited states into single, bi-exciton and trion components

$$n_{ex}\left(\tau_p,z\right) = n_1\left(\tau_p,z\right) + n_2\left(\tau_p,z\right) + n_{2T}\left(\tau_p,z\right) \tag{3.8}$$

for delay times greater than the Auger recombination time, $n_2\left(\tau_p > \tau_{AR},z\right) = 0$ and $n_{2T}\left(\tau_p > \tau_{AR},z\right) = 0$. The spatial variation of the remaining single-exciton states is given by

$$n_1\left(\tau_p > \tau_{AR},z\right) = N_{QD}\left(1 - P_0(z)\right)\left(1 - x_T(z,Q)\right) \tag{3.9}$$

where we have introduced the Poisson distribution function $P_0\left(z\right) = \exp\left(-J_{pump}\left(z\right)\sigma_{pump}\right)$ and the mole fraction, $x_T = N_T/N_{QDs}$ of photocharged QDs. Comparing Equation (3.8) and (3.9) we see that photocharged QDs contribute to the TA signal at early pump-delay times, but not at long delay times. We can now calculate the measured $\Delta T/T$ at early times (prior to Auger recombination) and late times (after Auger recombination).

$$\left.\frac{\Delta T}{T}\right|_{t_p < \tau_{AR}} = \exp\left\{QY\,\sigma_{probe}J^0_{pump}\left[1 - \exp\left(-\sigma_{pump}N_{QD}L_z\right)\right]\right\} - 1 \tag{3.10}$$

$$\left.\frac{\Delta T}{T}\right|_{t_p >> \tau_{AR}} = \exp\left\{\sigma_{probe}N_{QDs}\int_0^{L_z}\left(1 - x_T(z)\right)\left[1 - \exp\left(-\sigma_{pump}J^0_{pump}\exp\left[-\sigma_{pump}N_{QD}z\right]\right)\right]dz\right\} - 1 \tag{3.11}$$

The ratio of the TA signal at early to late times is R_{pop}.

$$R_{pop} = \frac{\left.\frac{\Delta T}{T}\right|_{\tau_p < \tau_{AR}}}{\left.\frac{\Delta T}{T}\right|_{\tau_p >> \tau_{AR}}} \tag{3.12}$$

The ratio is a function of pump fluence, pump wavelength, and flow rate. For low and/or high OD_{pump} and for the case of no photocharging, Equation (3.12) reduces to $R_{pop} = J_0\sigma_{pump}QY / \left(1 - \exp\left(-J_0\sigma_{pump}\right)\right)$ as we have shown previously. At high fluences $J_0\sigma_{pump} > 1$ this equations is linear in J_0 while at low fluences $R_{pop} \to QY$. The OD_{pump} enters Equation (3.10) and (3.11) through the following relationship, $\sigma_{pump}N_{QDs}L_z = \ln(10)OD_{pump}$ and for low OD_{pump} , $\frac{\Delta T}{T}\left(\tau_p\right) \cong OD_{probe}\ln(10)\cdot n_{1s}\left(\tau_p\right)$. The denominator of Equation (3.12) is reduced when photocharging occurs, resulting in a higher R_{pop} and thus an over estimation of QY.

We now determine $x_T\left(z\right)$ as a function of flow rate and photon fluence. To calculate this, we need to know the flow velocity profile of the QDs through the cell, the penetration profile of the pump beam, the diffusion of the QDs and generation and recombination rates. If we assume QDs exist in two quasi-static states during these experiments; a ground state (N_0), and a photocharged state (N_T), then the total number of QD is

$$N_{QDs} = N_0 + N_T \tag{3.13}$$

The flow is in the *x* direction (along the length of the flow cell) while the pump pulse travels in the *z* direction (along the thickness of the cell). The most general expression that accounts for the generation, recombination, transport by flow, diffusion and accumulation is given by:

$$\frac{\partial N_T}{\partial t} + \vec{V} \bullet \vec{\nabla} N_T = D\nabla^2 N_T + R_g - R_r \tag{3.14}$$

where D is the diffusivity of the QDs (~7x10^{-7} cm^2/s, calculated using the Einstein-Stokes relation for particle diffusion due to Brownian motion for 4.6 nm QDs with ligands attached in TCE solvent) and R_g and R_r are the volumetric rates of generation from the ground state and recombination back to the ground state (both with units of cm^{-3}s^{-1}). $\vec{V}$ is the velocity vector of the forced convection through the flow cell. At the highest flows tested (150 ml/min) the Reynolds number is 456 and will be laminar. Therefore, after the flow field is fully developed, convective transport of nanocrystals in the y and z directions can be neglected. The resulting unidirectional velocity profile for pressure driven flow between parallel plates is:

$$V_x(z) = \frac{6Q(L_z - z)z}{L_y L_z^3} \tag{3.15}$$

Q is the volumetric flow rate, L_z and L_y are the dimensions of the flow cell and z varies from 0 at the front face of the cell to L_z, so that $V_x = 0$ at $z = 0$ and at $z = L_z$. Combining (3.14) and (3.15) leads to:

$$\frac{\partial N_T}{\partial t} + V_x \frac{\partial N_T}{\partial x} = D\nabla^2 N_T + R_g - R_r \tag{3.16}$$

Diffusion in the x and y directions can be neglected since the forced convection in the x direction is by far the dominant form of transport for QDs at any place other than the cell walls, due to the no-slip boundary condition for the fluid flow. At the wall (z=0) or for static conditions, the time scale for convective replacement (δ_x/V_x, where δ_x is the diameter of the pump beam) goes to infinity since $V_x \to 0$. However, the time scale decreases rapidly with increasing flow rate or distance along z from the wall. For small flow rates and regions relatively close to the surface of the flow cell, the time scale for convective replacement drops to a few minutes. In

contrast, the time scale for QD diffusion across the thickness of the pump beam ($\delta_x^2/2D$) is over 1 hour. Thus, Equation (3.16) can be simplified to:

$$\frac{\partial N_T}{\partial t} + V_x \frac{\partial N_T}{\partial x} = D\frac{\partial^2 N_T}{\partial z^2} + R_g - R_r \tag{3.17}$$

Only the integral of N_T over the region of the x-y plane spanned by the probe beam is important, and we can gain further simplification and insight by integrating Equation (3.17) over x and y from 0 to δx and 0 to δy, respectively. Since V_x, R_g, and R_r are only functions of t and z (neglecting any spatial heterogeneity of the beam), the integration is straightforward for all terms except for the integral of the velocity term over x, which must be integrated by parts to give:

$$V_x N_T\Big|_0^{\delta x} - \int_0^{\delta x} (0) V_x N_T dx = V_x N_T \tag{3.18}$$

Thus, after integrating and dividing by $\delta x \delta y$ (the dimensions of the pump beam), Equation (3.17) simplifies to:

$$\frac{\partial N_T}{\partial t} + \frac{V_x}{\delta x} N_T = D\frac{\partial^2 N_T}{\partial z^2} + R_g - R_r \tag{3.19}$$

A solution to this PDE can be written in terms of an eigenfunction expansion or solved numerically with finite difference or finite element methods. However, these are not necessary since the convection and reaction terms are much more significant than the accumulation or diffusion terms (see appendix for justification) and therefore,

$$\frac{V_x(z)}{\delta x} N_T(z) = R_g - R_r \tag{3.20}$$

Now, to express the generation or recombination more explicitly requires a mechanistic model for each process. To develop such a mechanistic expression, we assume that the generation of photocharged QDs (N_T) is preceded by the absorption of a pump photon to create a hot-exciton

(N^*) and that the hot-exciton dissociates and ejects an electron or hole into a surface state or ligand with some probability (P_g).

$$N_0 + h\nu_{pump} \rightarrow N^* \xrightarrow{P_g} N_T \tag{3.21}$$

The spatial distribution of hot-exciton states is just the spatial distribution of excited QDs induced by the pump pulse and determined by the $OD_{pump} = \sigma_{pump} N_{QDs} L_z / \ln(10)$,

$$N^*(z) = \left(1 - \exp\left[-\sigma_{pump} J^0_{pump} e^{-N_{QDs}\sigma_{pump} z}\right]\right)\left(N_0 - N_T(z)\right) \tag{3.22}$$

where σ_{pump} is the absorption cross section at the pump wavelength and J^0_{pump} is the fluence incident at the front of the flow cell. We assume a constant probability P_g that an excited QD, *N*(z)* will decay into a trap state. Since the experiment is repeated many times a second, we need to multiply by the repetition rate of the pump laser pulse (r_p= 500 Hz) to obtain the overall volumetric generation rate based on the mechanism shown in Equation (3.21):

$$R_g(z) = P_g r_p N^*(z) \tag{3.23}$$

Thus, the generation rate has units of $cm^{-3}s^{-1}$ and contains only one adjustable parameter, the transition probability P_g. This simple model is basically a first order kinetic expression for the generation. Plugging in for the hot-exciton states, we obtain the following expression for the volumetric generation rate and define a depth dependent generation rate constant, $\gamma_g(z)$:

$$\begin{aligned} R_g(z) &= P_g r_p \left(1 - \exp\left[-\sigma_{pump} J^0_{pump} e^{-N_{QDs}\sigma_{pump} z}\right]\right)\left(N_{QDs} - N_T(z)\right) \\ &= \gamma_g(z)\left(N_{QDs} - N_T(z)\right) \end{aligned} \tag{3.24}$$

where all parameters other than P_g are determined experimentally and fixed.

Similarly, the simplest reasonable mechanistic expression for the recombination is also a first order kinetic expression given by:

$$R_r(z) = \gamma_r N_T(z) \tag{3.25}$$

where γ_r is constant and has units of inverse seconds and hence $1/\gamma_r$ may be considered as a characteristic time scale for relaxation of the photocharged QD. Here we have assumed that the recombination does not require the absorption of a pump photon. These are the simplest kinetic expressions that we think are capable of explaining the experimentally observed trends, but more complicated mechanisms should not be ruled out. Such alternative kinetic expressions can be derived and checked against these experiments in a manner similar to what we show below.

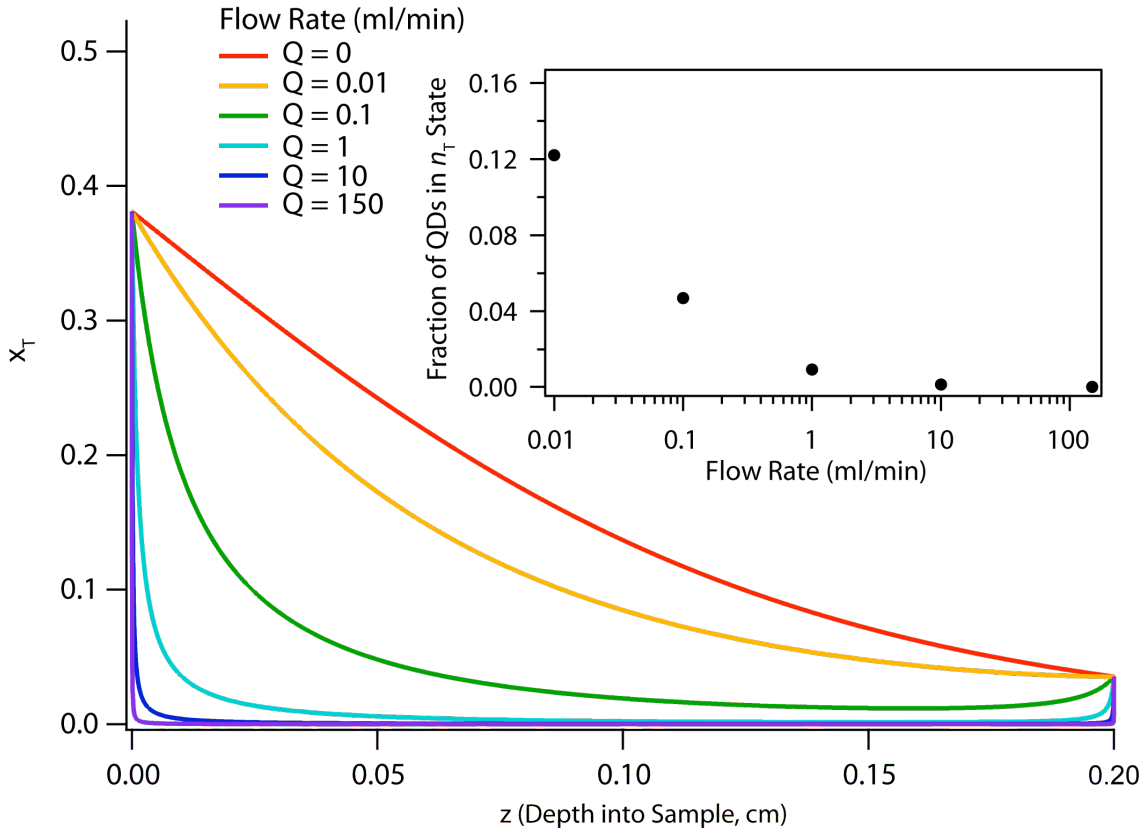

Figure 3.3.1: Model for the Fraction of Photocharged QDs

Mole fraction of photocharged QDs, x_T , for a variety of flow rates where the red-line is for static conditions. The simulation is for photon fluence that corresponds to an $\langle N_0 \rangle = 0.24$ and an OD of 1.3, γ_r= 0.027 and P_g =1x10^{-5}. Inset displays the total fraction of photocharged QDs, $f_T = \int_0^{Lz} x_T(z)dz$, as a function of volumetric flow rate. Note that as the flow rate increases, the TA response will contain less and less contribution from the photocharged QDs.

Substituting the equation for R_g (3.24) and R_r (3.25) into Equation (3.20) and dividing by N_{QDs} we are left with:

$$\frac{V_x(z)}{\delta x}\frac{N_T(z)}{N_{QDs}} = \gamma_g(z)\left(1-\frac{N_T(z)}{N_{QDs}}\right) - \gamma_r\left(\frac{N_T(z)}{N_{QDs}}\right) \tag{3.26}$$

which we can solve for the mole fraction $x_T = N_T/N_{QDs}$.

$$x_T(z) = \frac{\gamma_g(z)}{\gamma_g(z) + \gamma_r + \frac{V_x(z)}{\delta x}} \tag{3.27}$$

Figure 3.3.1 displays $x_T(z)$ at an excitation intensity of $\langle N_0 \rangle = 0.24$, $OD_{pump} = 1.3$ for a variety of flow rates. The inset shows the total fraction of photocharged QDs as a function of Q. At Q = 0 ml/min, approximately 16% of the QDs are photocharged while at Q > 1 mL/min, that fraction has decreased to less than 1% and by 150 mL/min and there are no noticeable photocharged QDs.

3.4 Results

We find under some experimental conditions that flowing the sample produces a transient that differs from that of a static sample. Figure 3.4.1 shows a transient bleaching experiment of a 4.6 nm PbSe QD sample with a first exciton transition energy of, E_g = 0.84 eV. The samples were excited with 3.1 eV excitation light (~3.7 E_g). In panel (a), the samples were flowed at a volumetric flow rate of Q = 150 mL/ min, while in panel (b), the experiment was performed under static conditions. The excitation fluences varied from 2.1 x 10^{12} to 3.7 x 10^{13} photons cm^{-2} $pulse^{-1}$, for which we estimate the average occupation number, $\langle N_0 \rangle$, to range from 0.04 to 0.58. Panel (c) compares $\Delta T/T$ at the highest fluence corresponding to $\langle N_0 \rangle = 0.58$. The data deviate at high photon fluence and for longer pump-delay times. We show in the supplemental section

for reference 31 (Figure S.3) data for a pump wavelength of 800 nm, which corresponds to excitation at 1.8 E_g. In that experiment, we see no differences between static and flowing conditions until well past where the TA response saturates, furthermore, the deviation is substantially different than what is observed in Figure 3.4.1 and therefore is of a different origin that what is studied here. To ensure that our data is in the linear regime we do not consider data for $\langle N_0 \rangle > 2.5$.

In order to model the data in Figure 3.4.1, we first need to extract the first exciton lifetime, τ_1, and the Auger recombination lifetime from the TA data where $h\nu_{pump} < 2\,E_g$ (Figure S.3)[31]. In the case where MEG is not energetically allowed, the time-dependent population of the first exciton level is to a very good approximation given by $n_{1s}(\tau_p) = n_0 \sum A_i \exp(-\tau_p / \tau_i)$ where $A_i = \sum_{j=i}^{\infty} p_j$ and p_j is the jth term of the Poisson distribution, $p_j = \langle N_0 \rangle^j \exp(-\langle N_0 \rangle) / j!$. A non-linear least squares global fitting function is employed to model all of the transients simultaneously, where τ_1 and τ_2 (single-exciton and bi-exciton lifetimes) are varied globally, and $\tau_i = 4\tau_2 / i^2$ for $i > 2$, while $\langle N_0 \rangle$ is independently varied for each transient. This global fitting approach returns consistent results for τ_1 and τ_2 with small uncertainties. We find τ_1 = 38 (±2) ns and τ_2 = 73 (±2) ps. The value of τ_2 agrees well with our previous results for similarly sized PbSe QDs.[3] All subsequent analysis of data for the 4.6 nm QDs have fixed τ_1 and τ_2.

To model the data in Figure 3.4.1b, we need only include a term to the $A_i's$ that accounts for the non-poisson nature of MEG, and therefore accounts for multiple-excitons produced per absorbed photon (this approach has been described in detail elsewhere[1]). We again globally fit

our model to the data with the $\tau_i^{'}$s fixed at the values determined in the experiment above and allow the MEG efficiency to vary globally while $\langle N_0 \rangle$ is varied for each trace. The results of the fit are shown as the dotted lines in Figure 3.4.1b. To model the data for the static condition (Figure 3.4.1a), we modify the above equation to include a term that represents photo-generated trapped states; $n_{1s}(\tau_p) = (1 - f_T)\sum A_i \exp(-\tau_p/\tau_i) + f_T \exp(-\tau_p/\tau_{2T})$, where f_T is the total steady-state fraction of photocharged QDs, while τ_{2T} is the lifetime of their excited state (labeled n_{2T} in Figure 3.2.1). The lifetime, τ_{2T}, is a global variable while f_T is allowed to vary for each individual trace. The values of $\langle N_0 \rangle$ for each trace are held constant from what was found while performing the global fit to the data of Figure 3.4.1a. We find τ_{2T} = 217 (±3) ps and plot the value of f_T for each $\langle N_0 \rangle$ in Figure 3.4.1d, the error bars represent ± one standard deviation from the fitting routine. To model f_T as a function of fluence, we calculate x_T from Equation (3.27) setting Q = 0 and $f_T = \int_0^{L_z} x_T(z)dz$ and vary P_g to model our data with the value of γ_r fixed at 0.027 s^{-1}, determined in a separate experiment (see below), since for this data set γ_r and γ_g cannot be determined independently. The best-fit line is displayed in Figure 3.4.1d. The dashed line in Figure 3.4.1d are the calculated values for f_T setting Q = 150 ml/min, demonstrating that under flowing conditions the contribution from long-lived photocharged states is essentially zero.

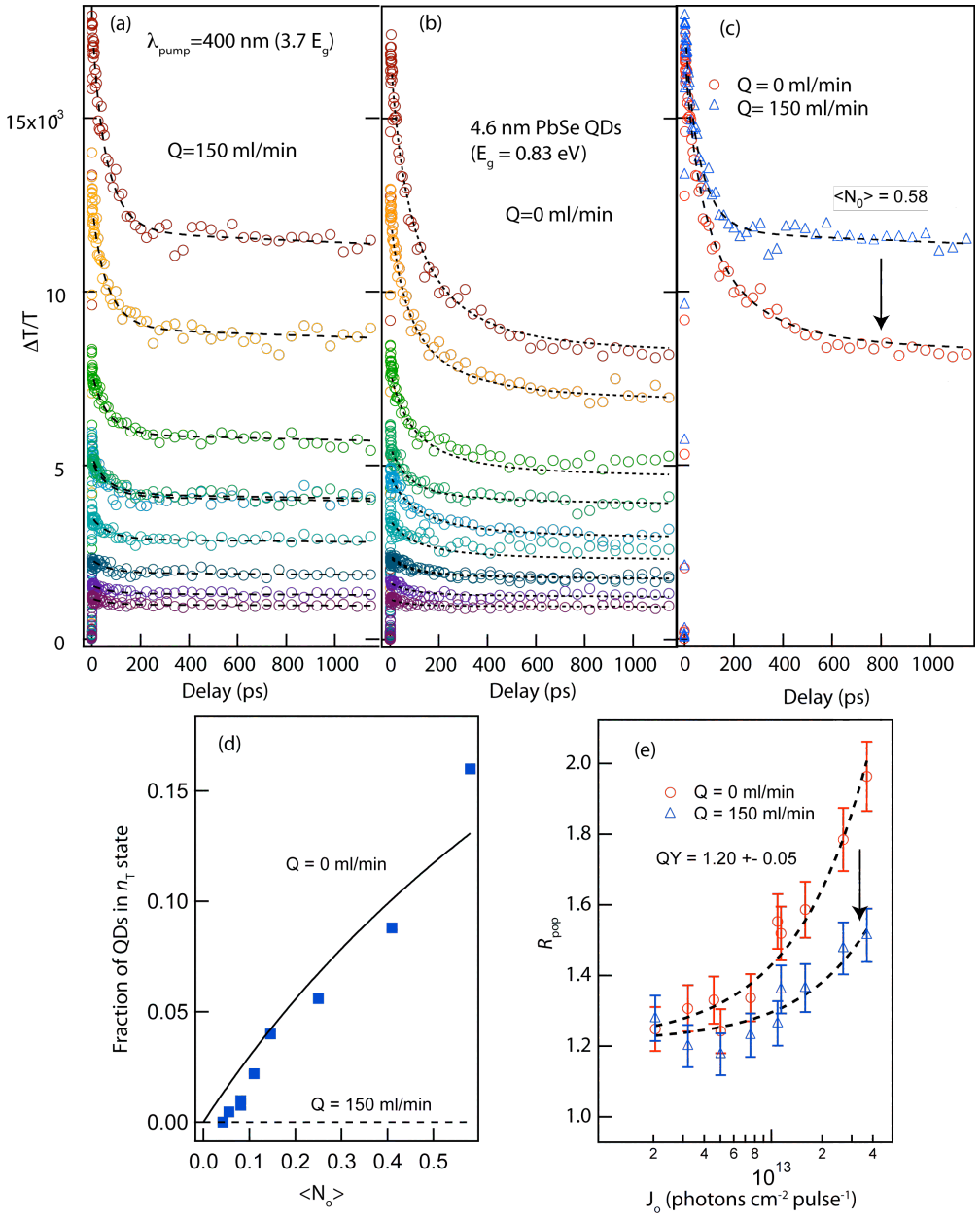

Figure 3.4.1: Transient Absorption Data for 4.6nm PbSe
PbSe excited at 400 nm (3.7 E_g); panel (a) is for flowing conditions (Q=150 mL/min) and (b) is for static conditions. Panel (c) displays the data for the higher fluence from panels (a) and (b). The dotted lines in panels (a), (b) and (c) are the model described in the text. In panel (d), we display the total steady-state fraction of QDs in state N_T as a function of fluence. The solid line is a result of our model with a flow rate of zero, while the dotted line shows the model for flowing conditions. Panel (e) displays R_{pop} for the flowing and static cases. The R_{pop} values are extracted from panels (a) and (b). The dotted lines are the results of the model used to extract the QY when both data sets are modeled simultaneously with the same set of parameters. We find that the QY = 1.20 (±0.05).

In Figure 3.4.1e we display R_{pop} for the two data sets in Figure 3.4.1a and b. The values of R_{pop} for the flowing and static cases approach each other at low photon fluences consistent

with the data presented in Figure 3.4.1d that shows f_T decreases towards zero for low photon fluences. The data in Figure 3.4.1e are modeled by calculating R_{pop} as a function of photon fluence from Equation (3.12) where x_T is calculated from Equation (3.27). Both data sets are modeled simultaneously with the same set of parameters and only the experimentally determined flow rate is changed between the two data sets. We allow the pump cross section, σ_{pump}, the probability of generation, P_g, and the QY to vary; σ_{pump} is determined by how fast R_{pop} deviates from its low fluence values, P_g determines the difference between the static and flowing curves, and the QY is determined by the value of R_{pop} as $J_0 \to 0$. As before, the value of γ_r is fixed at 0.027 s^{-1}. The dotted lines are the results of the model and we report the best-fit values in Table 3.4.1. We find good agreement between all of our measured data and the result of our model. Additionally, we find good agreement between the different ways in which we have analyzed our data to extract out the parameters of the model and we report the best-fit values in Table 3.4.1. We discuss our results below.

Figure 3.4.2 is the TA data for the 4.6 nm PbSe QDs excited at 330 nm (4.5 E_g). Part (a) is for flowing conditions and part (b) is under static conditions. Figure 3.4.2c compares $\Delta T/T$ for $\langle N_0 \rangle$=1.6 for flowing and static conditions. In contrast to what was observed with 400 nm excitation (see Figure 3.4.1c), the differences between flowing and static are more dramatic at the higher pump photon energies. In fact, the transients differ for all pump-probe delay times. However, we find that as the photon fluence decreases, the differences are diminished as in the 400 nm case. The data were globally modeled in a similar fashion as was done for the data in Figure 3.4.1, however the values of $\langle N_0 \rangle$ were not the same when modeling the flowing and static data even though the fluences were the same, this most likely indicates that the

photocharged QDs do not have the same absorption cross section as neutral QDs. Figure 3.4.2d displays f_T as a function of $\langle N_0 \rangle$ and the solid line is our model as described above. Finally, Figure 3.4.2e displays R_{pop} for flowing and static conditions and the dotted lines are the best-fit results. We find the QY to be 1.55 (±0.05) and the other parameters of the fitting are reported in Table 3.4.1.

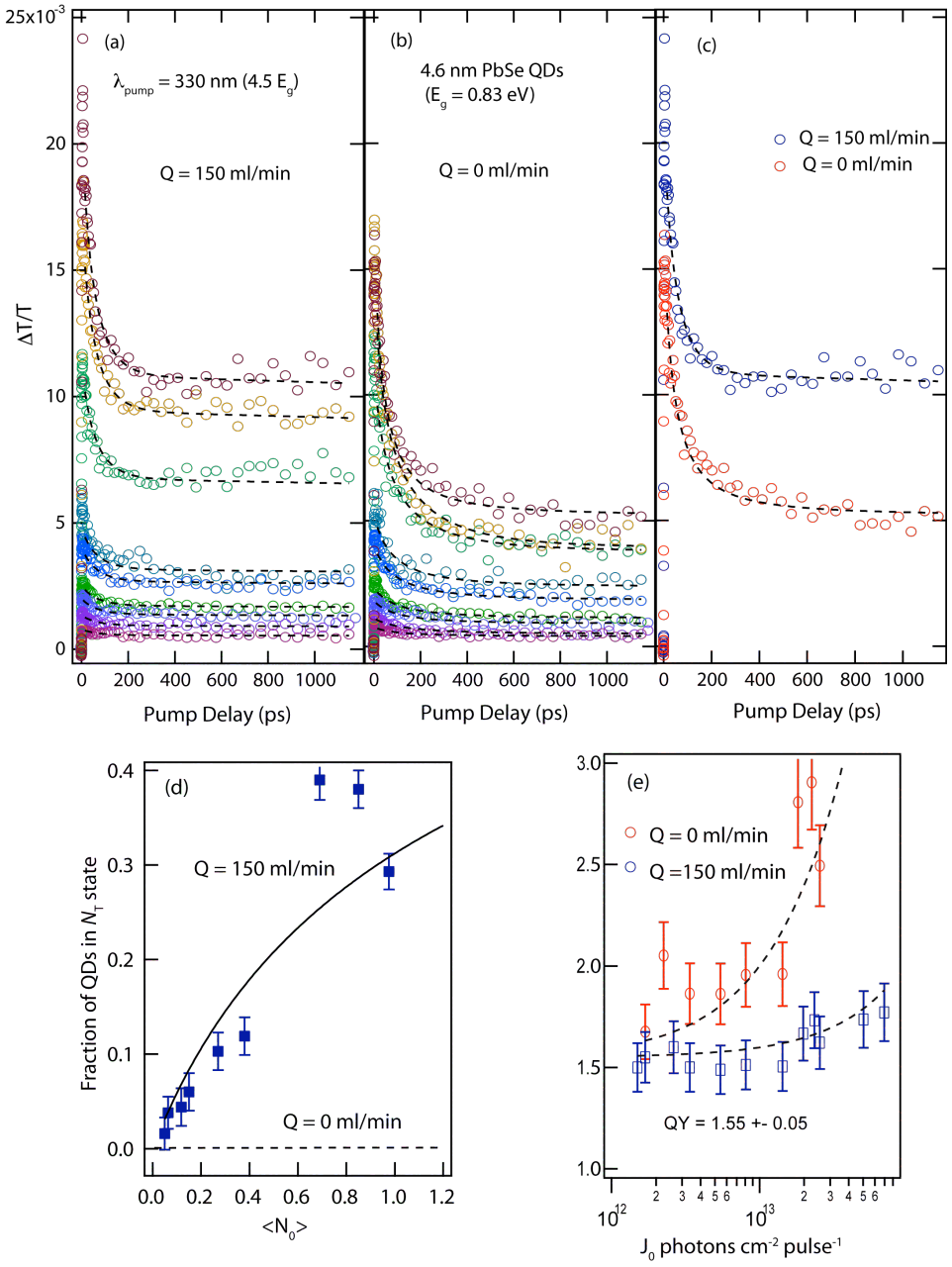

Figure 3.4.2: High Energy TA Data for 4.6 nm PbSe QDs
PbSe QDs excited at 330 nm (4.5 E_g); panels (a), (b), (c), and (d) are similar as described for Figure 3.4.1. The main difference between this data set and that shown in Figure 3.4.1 is the higher degree of photocharging observed. We find the QY to be 1.55 (±0.05).

We repeated the experiments for the 4.6 nm PbSe QDs described above, but used QDs that had been treated with $Cd(Oleate)_2$ as described in the experimental section. The results are presented in Figure 3.4.3 and Figure 3.4.4, and the data were analyzed identically as for the untreated QDs discussed above. There are some significant differences between the data for PbSe QDs with and without the addition of $Cd(Oleate)_2$. Comparing Figure 3.4.1 and Figure 3.4.3 (λ_{pump} = 400 nm) we see that with the Cd-treatment the effects of photocharging in a static sample are minimized. In Figure 3.4.3(e), we see that R_{pop} is nearly identical when flowing or static and the degree of photocharging is smaller by a factor of ~2 as seen in Figure 3.4.3(d). Comparing Figure 3.4.2 and Figure 3.4.4, where λ_{pump} = 330 nm, also shows similar improvements when using the Cd-treatment. For as-made QDs, the degree of photocharging is significant and can be reduced by a factor ~ 10 with the Cd-treatment. We also find that the QY is slightly higher for the Cd-treated QDs; for λ_{pump} = 400 nm the QY increases from 1.20 to 1.27, a 6% relative increase, while for λ_{pump} = 330 nm the QY increases from 1.55 to 1.64, also a 6% relative increase. We discuss possible mechanisms for this increase later, but due to the noise associated with the data we are unable to determine if this difference is statistically significant.

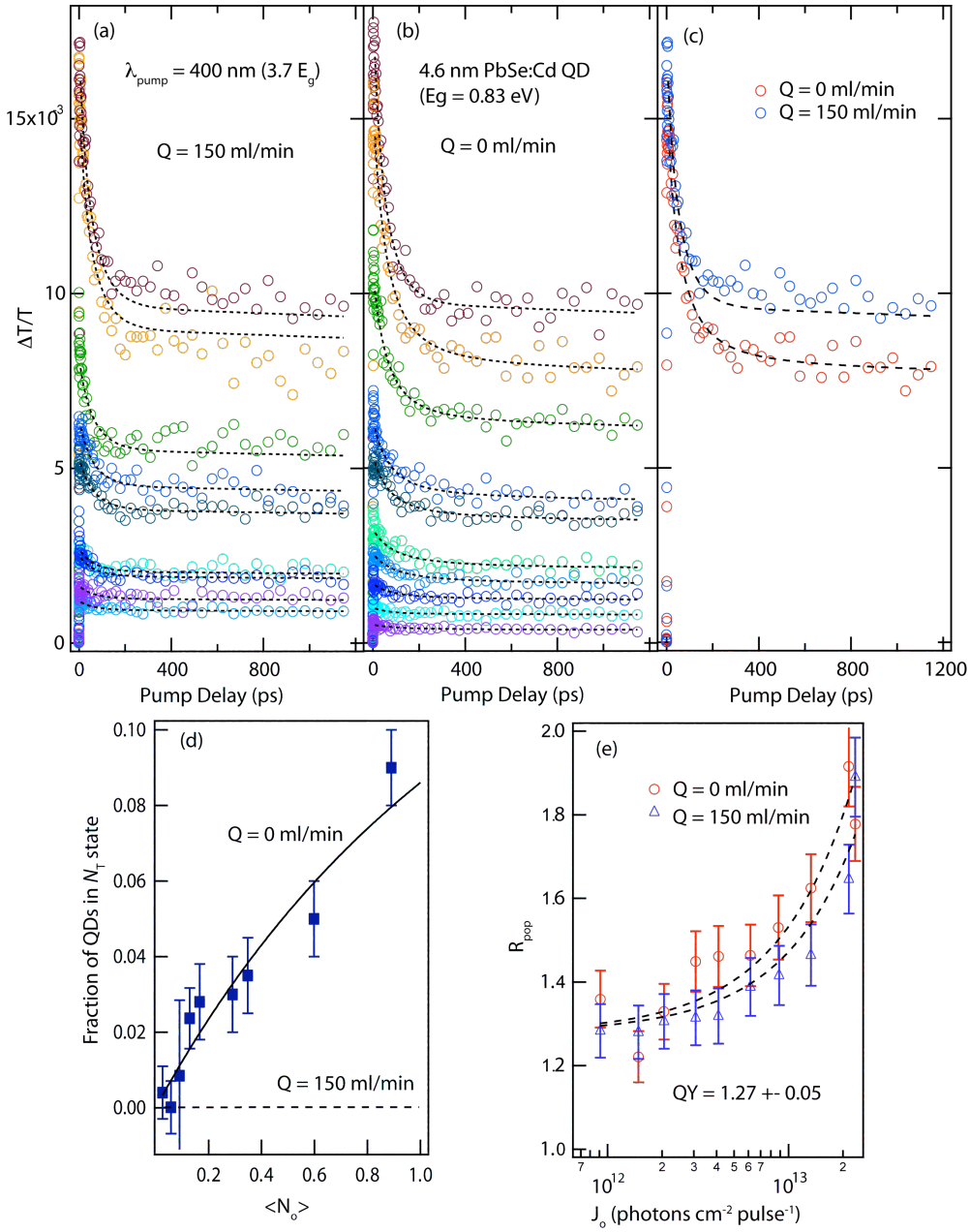

Figure 3.4.3: Transient Absorption Data for 4.6 nm PbSe-Cd(oleate)$_2$ QDs
PbSe QDs treated with Cd(oleate)$_2$ and excited at 400 nm (3.7 E_g). Panels (a), (b), (c), and (d) are similar as described for Figure 3.4.1. This data set is compared to the untreated PbSe QDs displayed in Figure 3.4.1. Treating the QDs with Cd^{2+} reduces the differences between flowing and static conditions. We find a 6% relative increase in QY = 1.27 (±0.05) compared the untreated QDs.

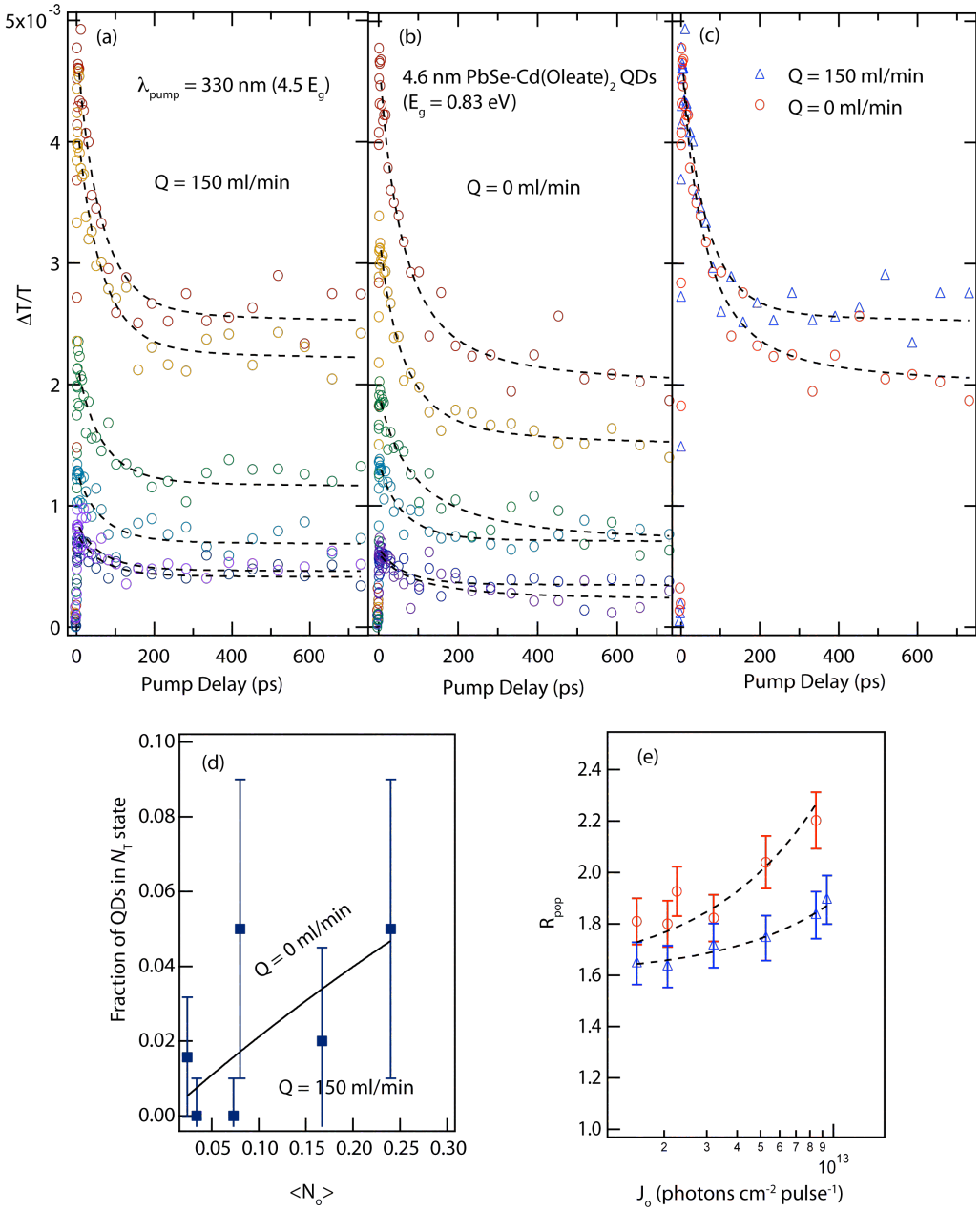

Figure 3.4.4: High Energy TA Data for 4.6 nm PbSe-Cd(oleate)$_2$ QDs
PbSe QDs treated with Cd(oleate)$_2$ and excited at 330 nm (4.4 E_g). Panels (a), (b), (c), and (d) are similar as described for Figure 3.4.1. Note that the transient were only collected to 700 ps in contrast to the 1200 ps data window shown in Figure 3.4.1, Figure 3.4.2 and Figure 3.4.3. This data set can be compared to the untreated PbSe QDs displayed in Figure 3.4.2. Again, we find that the Cd^{2+} treatment reduces the differences between flowing and static conditions. The degree of photocharging is a factor of 10 less with the Cd^{2+} treatment. As for the 400 nm excitation we find a 6% relative increase in QY = 1.64 (±0.02).

We also studied 6.6 nm PbSe QDs, (E_g = 0.66 eV) however, we only studied QDs that had a Cd-oleate treatment. We show 1300 nm transient absorption data in the supporting

information, and display the R_{pop} analysis in Figure 3.4.5 for 400 nm and 330 nm excitation, corresponding to 4.7 and 5.7 E_g. The data for 400 nm excitation does not show a large difference between flowing and static conditions and we were unable to extract a value for τ_{2T} from the TA data for the larger QDs because the degree of photocharging was not significant. At 330 nm we only collected data under flowing conditions in order to obtain a QY and we find QY = 1.61 and 1.95 for the two excitation energies.

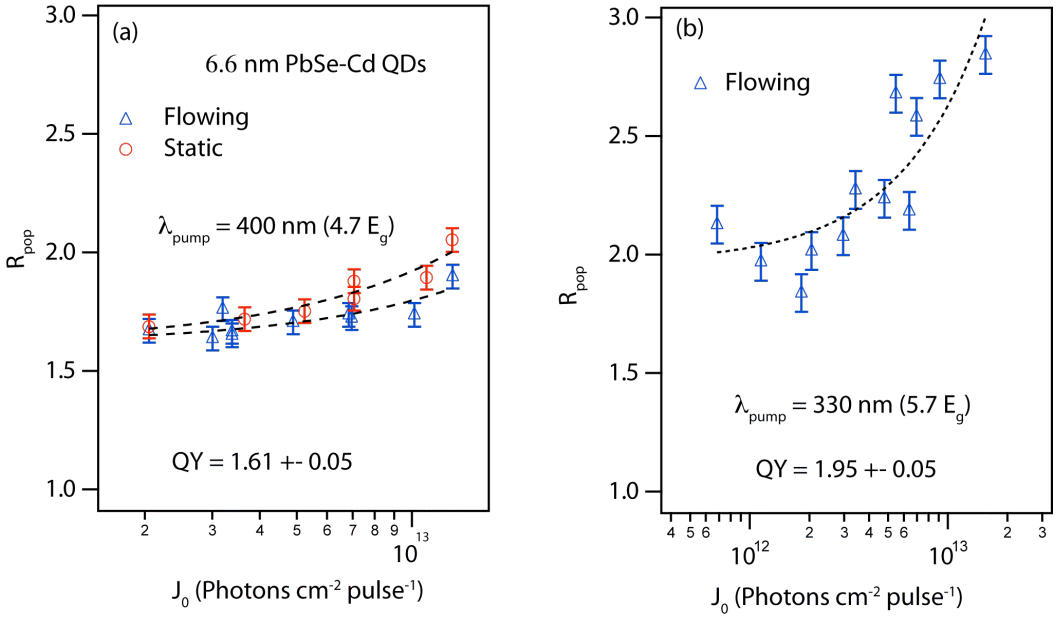

Figure 3.4.5: R_{pop} for 6.6 nm PbSe-Cd(Oleate)$_2$ QDs

Transient Absorption data for treated 6.6 nm QDs excited at (a) $\lambda_{Pump} = 400$ nm corresponding to 4.7 E_g. The data were collected for both flowing and static conditions and the QY = 1.61 (±0.05). Panel (b) is for λ_{pump} = 330 nm corresponding to 5.7 E_g and the QY = 1.95 (±0.05). The data in panel (b) are for flowing only.

To further study the generation and recombination of the photocharged states, we measured R_{pop} as a function of flow rate for a fluence that is high enough to see a reasonable difference between flowing and static conditions, since we find little difference at low excitation fluences. Figure 3.4.6 displays R_{pop} as a function of flow rate for a few select QD samples and

excitation wavelengths. Part (a) is for the 4.6 nm PbSe QDs with λ_{pump} = 330 nm and at $\langle N_0 \rangle$ = 0.24, part (b) is for 4.6 PbSe-Cd(oleate)2 QDs and λ_{pump} = 330 nm but with $\langle N_0 \rangle$ = 0.55, part (c) is the same as part (b) but with $\langle N_0 \rangle$ = 0.17 and part (d) display data for 6.6 nm PbSe-Cd(oleate)2, λ_{pump} = 400 nm with $\langle N_0 \rangle$ = 1.2. The value plotted for a flow rate of 10-5 ml/min in each of the four experiments corresponds to the static condition. The data are modeled using Equation (3.12) and (3.27) and we vary Pg, γr, and QY, while the photon fluence is an input into the model. The overall difference in R_{pop} between flowing and static is mainly determined by Pg, the flow rate at which R_{pop} decreases determines γr, and the lower value of R_{pop} is set by the input fluence and the QY. One of the striking results of the present study is that only slow flow rates are needed in order to reduce the photocharging to near zero. A flow rate of only 10 ml/min reduced photocharging to about the same value as a flow rate of 150 ml/min (maximum flow rate obtained in this study). A flow rate of 10 ml/min refreshes the entire volume in the cuvette every 3.6 s, and the excitation volume is refreshed every 0.5 s.

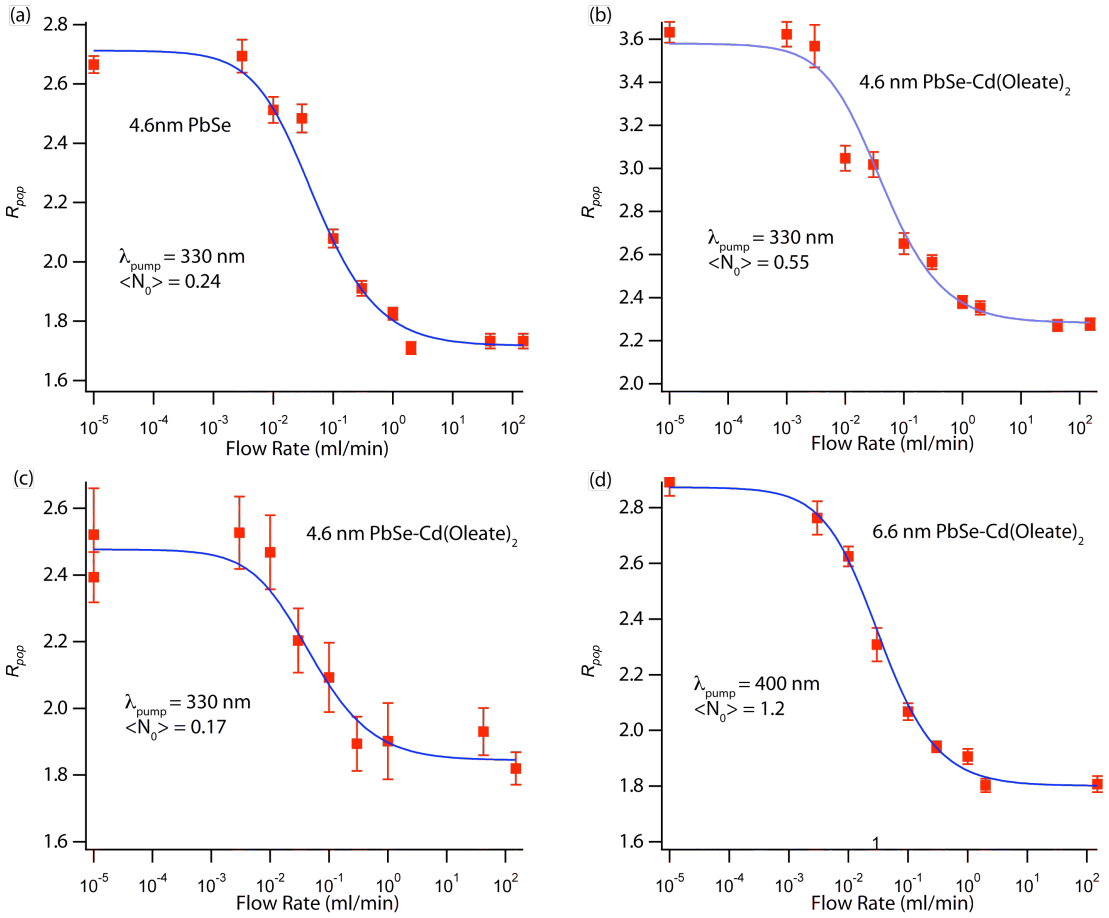

Figure 3.4.6: R_{pop} vs. Flow Rate Data
Flow rate data for, (a) as-made 4.6 nm PbSe excited at 3.8 eV and $\langle N_0 \rangle = 0.24$, (b) 4.6 nm PbSe treated with Cd(Oleate)$_2$ and excited at 3.8 eV and $\langle N_0 \rangle = 0.55$, (c) 4.6 nm PbSe treated with Cd(Oleate)$_2$ and excited at 3.8 eV and $\langle N_0 \rangle = 0.17$ and (d) 6.6 nm PbSe treated with Cd(Oleate)$_2$ and excited at 3.1 eV and $\langle N_0 \rangle = 1.23$.

In the model above, we assumed the generation rate to be first order with respect to the photon fluence. This implies that the generation process is not a multi-photon process that might be expected for an Auger-ionization (AI) event (absent a MEG-AI pathway). To check for AI we studied the QD samples under high fluence ($\langle N_0 \rangle > 2$). For low photon energies ($hv < 2E_g$) no signature of photocharging was observed. Thus, we conclude that either (1) AI produces an ionized state that is unlike what we observe here, or (2) AI is not a dominate pathway for these QD samples, and (3) the photocharging observed here is a direct process originating from the initially hot-exciton state. The generation probability P_g is low (10^{-5}) and increases with photon

energy. For example, for the 4.6 nm PbSe-Cd(Oleate)$_2$ QDs, P_g increases from 1.6x10^{-5} at λ_{pump} = 400 nm to 8x10^{-5} at λ_{pump} = 330 nm. We find the degree of photocharging can be reduced by protecting the surface of the QDs, in our case, treating with Cd(oleate)$_2$. At λ_{pump} = 400 nm, P_g is reduced from 6.6 x10^{-5} to 1.6x10^{-5} and at λ_{pump} = 330 nm, P_g is reduced from 2.2 x 10^{-4} to 8 x 10^{-5} by the Cd-treatment. The time scale for establishing the steady state population is $1/\gamma_g$, which is dependent on the penetration depth z, and ranges from 30 seconds to several minutes. The recombination rate constant is not fluence dependent, and does not depend on the pump photon-energy or surface treatment, suggesting that the recombination process is inherent to the QD or assisted by the probe photons. Any charge carriers trapped on the QD-surface or ligand will naturally recombine with the core carrier in order to conserve charge neutrality over a characteristic timescale, $\tau_r = 1/\gamma_r \approx 37$ s.

Table 3.4.1: Experimental Parameters From Modeling Data.
(values in parentheses represent one standard deviation from the non-linear fitting routine)

Sample	λ (nm)	τ_1 (ns)	τ_2 (ps)	p_g	γ_r (1/s)	σ (cm^2)	QY
d = 4.6 nm							
untreated	400	38 (2)	73(2)	6.6(.1)x10^{-5}	0.027	3.9 x 10^{-14}	1.20(.05)
Cd(Oleate)$_2$	400	38 (2)	73(2)	1.6(.1)x10^{-5}	0.027	3.9 x 10^{-14}	1.27(.05)
untreated	330	38 (2)	73(2)	2.2(.1)x10^{-4}	0.027	5.5 x 10^{-14}	1.55(.05)
Cd(Oleate)$_2$	330	38 (2)	73(2)	8(1)x10^{-5}	0.027	5.5 x 10^{-14}	1.64(.02)
d = 6.6 nm							
Cd(Oleate)$_2$	400	38 (2)	144(3)	2.7(.8)x10^{-5}	0.027	3.0 x 10^{-14}	1.61(.05)
Cd(Oleate)$_2$	330	38 (2)	144(3)		0.027	8.4 x 10^{-14}	1.95(.05)

We plot the extracted QYs from this work in Figure 3.4.7. The brown squares are for the untreated PbSe QDs while the red triangles are for the $Cd(oleate)_2$ treated QDs. We have also plotted recent data from LANL[4] where the PbSe QDs samples were stirred rather than flowed and find reasonable agreement between these two data sets. The most recent paper[75] from this group also finds similar values for multiple samples of stirred PbSe QDs. When comparing these results to previous static QYs, it is clear that some variations in the reported QYs can be traced to photocharging. The degree of photocharging is minimized in static samples by using low photon-fluences ($\langle N_0 \rangle < 0.1$). In our original report of MEG in PbSe and PbS QDs, we found a wide variation in QYs among three different samples and we plot those results in Figure 3.4.7(E_g = 0.91 eV (open red circles), 0.82eV (open blue circles), and 0.72eV (open green circles)). We found in the smallest size QDs the apparent QY reached 300% at $4E_g$ while in the larger QDs the QY was only ~175% at $4E_g$. Subsequent work almost always reproduced the lower QY values[80]. We now believe that the higher yields from previous static results most likely resulted from the photocharging phenomenon studied here. The QYs in our original work were determined at $\langle N_0 \rangle$ = 0.25, and as we have shown here, all samples should be flowed or stirred and that for static samples $\langle N_0 \rangle$ should be less than 0.1 to give the best chance at achieving accurate QY measurements. Subsequent work always determined the QY using lower $\langle N_0 \rangle$ values. The QY values reported here do not have contributions from photocharging and are determined at low $\langle N_0 \rangle$ values and thus any extraneous contributions should be minimized. The variations in apparent QYs presumably are due to either differing experimental or synthesis conditions.

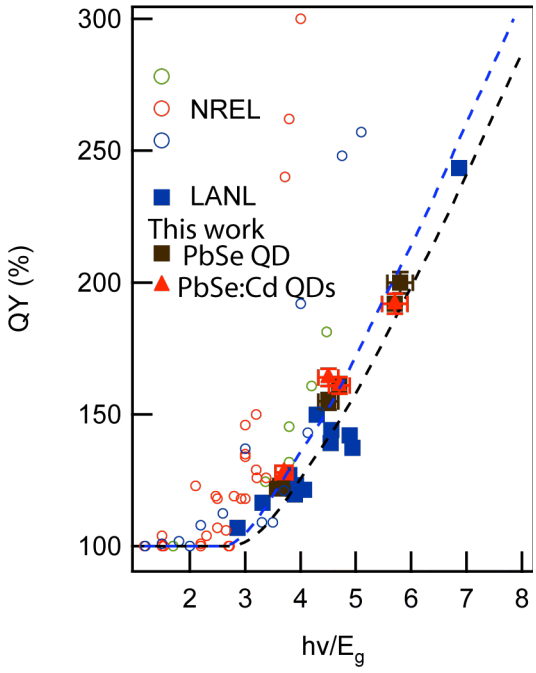

Figure 3.4.7: Value of QY vs for PbSe QDs

Brown squares are for the as-made PbSe QD samples while the red triangles are for the Cd-treated QD samples. The blue squares are data reported from LANL and reported in reference 4. The dotted lines are a guide to the eye.

The transient absorption spectra of a photocharged QD are expected to be different than that of fully relaxed QDs due to locally generated electric fields (carrier-induced stark effect) and the lower density of available states due to state filling.[66,82] However, in PbSe QDs, the difference between photocharged and relaxed QDs maybe small because Coulomb interactions are screened (charging energy $E_c \leq 4\ mV$) due to a high static dielectric constant (~250 in bulk which is reduced to ~<100 in QDs by surface polarization effects).[83,84] Figure 3.4.8 displays TA spectra of four experiments, in part (a) we display the un-normalized data while in part (b) the data are normalized. The four spectra correspond to 4.6 nm PbSe QDs with $\lambda_{pump} = 330$ nm and for pump-probe delay, $\tau_p = 3$ ps , (black lines) and $\tau_p = 600$ ps (blue lines) for flowing (dotted lines) and static conditions (solid lines). The photon fluence is for $\langle N_0 \rangle \sim 2.5$ so that ~92% of all QDs in the excitation volume absorb a photon and ~71% have absorbed more than one photon. There is a red-shift between the bi-exciton spectra (τ_p=3 ps) and the single-exciton spectrum (τ_p= 600 ps), ΔE= 80 meV, that arises due to Coulomb interaction between the

electrons and holes corresponding to the bi-exciton binding energy. A carrier-induced transient Stark-shift has also been observed in PbSe QDs and is found to be ~ 30 meV.[1] For static conditions, the τ_p =3 ps spectra should be shifted in energy due to charged QDs, while the τ_p = 600 ps spectra is not influenced because any excitons in charged QDs have already decayed making them undetectable by TA. Therefore, any shift in the TA spectrum between static and flowing conditions would be observed at τ_p = 3 ps. However, we find no shift in the transient absorption spectra of the 4.6 nm QDs studied here. The only difference between flowing and static conditions is a small decrease in intensity at τ_p = 3 ps and a larger decrease at 600 ps. Using the flow model developed here, we estimate f_T is approximately 50% for these conditions. Since there is no observed stark shift between charged and uncharged QDs, we see three possible explanations. (1) Since we are looking for variations in the Stark-shift between the trion and the bi-exciton spectrum, there may not be enough spectral resolution to notice a difference. In recent scanning tunneling microscopy (STM) and spectroscopy (STS) experiments on PbSe-CdSe core-shell QDs, the charge induced stark effect was calculated to be < 1 meV and was therefore neglected in that experiment.[85] (2) The contribution from charged QDs to the bi-exciton spectrum is at most 50% which would reduce the observable Stark-shift. (3) The absence of a Stark-shift indicates the lack of charged QDs and it is possible that some other trapped state is responsible for the phenomenon reported here.

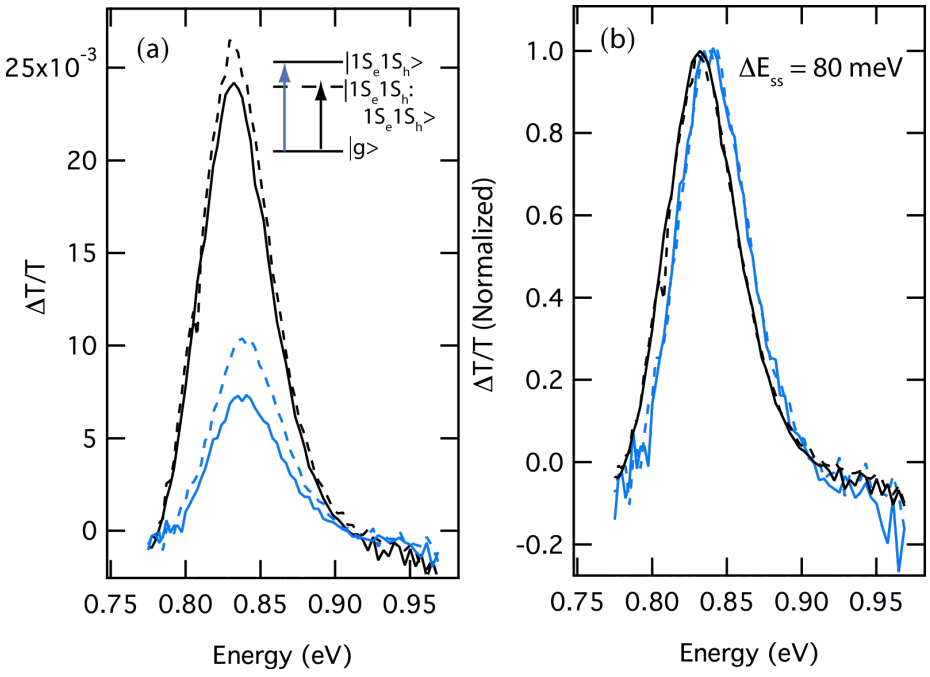

Figure 3.4.8: Transient Absorption Spectra

Transient absorption spectra of 4.6 nm PbSe for λ_{pump} = 330 nm and $\langle N_0 \rangle$ =2.5 at τ_p = 3 ps (black lines) and times and τ_p = 600 ps (blue lines). Part (a) is for the raw data while part (b) displays the normalized data.

3.5 Discussion

Surfaces of QDs play a role in determining photoluminescence quantum yields[79,86] and MEG efficiency,[32] and passivation of electron or hole traps in colloidal QDs may affect a multitude of experiments. In particular, passivation may increase PL[86,79] and yield longer exciton lifetimes as seen in transient absorption or TRPL.[87] Passivation can be accomplished with the addition of a small amount of an electron donating ligand, however, addition of an excess of passivating ligand, or in systems with poor band edge alignment,[87] can lead to the formation hole traps that quench PL. Alternately, inorganic passivation is employed by growing a shell of a larger bandgap material on the QD surfaces. For PbSe, CdSe is an ideal passivating-shell for three reasons. (1) CdSe exhibits high stability to ambient conditions, (2) the larger bulk bandgap of CdSe straddles that of PbSe effectively confining the charge carriers to the core of the PbSe in

a type I arrangement (see supporting information[31]), and (3) the lattice mismatch is small (~1%).[79] In our results, we find that the band edge absorption blue shifts 10-20 nm based on the size of the QD and amount of $Cd(Oleate)_2$ added due to ion exchange of the outer Pb^{2+} layers with Cd^{2+}, which effectively shrinks the core. This is supported by the fact that excess cadmium and the larger lattice energy of CdSe would favor an exchange of lead with cadmium. Based on the shift found in the QD absorbance spectra, we estimate the average thickness of this shell to be approximately 0.5-1 Å. Considering that the lattice constant of either PbSe or CdSe is approximately 6 Å, we expect that there is less than a complete monolayer. The Cd-shell increases the PLQY of our QD samples (see supporting information), reduces the apparent photocharging in the 4.6 nm QDs (see Table 3.4.1), and may increase MEG efficiency. The binding of $Cd(Oleate)_2$ to any dangling bonds would passivate available trap sites, and the substitution of Cd^{2+} for Pb^{2+} would effectively increase the exciton binding energy and thereby reduce P_g. A small decrease in γ_{cool} (see Figure 3.2.1) can effect the MEG efficiency. Hot carrier cooling in bulk semiconductors occurs via phonon emission and is determined by a characteristic phonon scattering length. In bulk PbSe the scattering length is ~ 67 nm which is larger than the QD samples studied here,[30] indicating that the surfaces of the QDs must play a role in the carrier relaxation.

The proposed mechanism and lifetime of the photocharging process observed in these experiments is similar to the results found in fluorescence intermittency experiments and this relationship necessitates further examination. Fluorescence intermittency, or QD blinking,[88] is thought to be caused by the formation of a trapped carrier in isolated QDs (for a comprehensive review see references 89, 90). While there is debate over the exact mechanism, the 'off', or dark, state found in QD fluorescence, it is believed to be a charged QD created when an Auger event

(Auger-ionization) ejects a core electron (or hole) into a surface state of the QD and quenches luminescence by opening up a non-radiative trion (charged-exciton) decay pathway that dominates recombination. The lifetime of the trion is thought to be different for positive and negatively charged trions and related to the bi-exciton lifetime by $\frac{1}{\tau_2} = \frac{2}{\tau_{2T^-}} + \frac{2}{\tau_{2T^+}}$.[91] In CdSe QDs one observation found the negative trion to be 7.5 times longer than the bi-exciton lifetime.[92] The charge carrier is trapped near the QD surface and has some probability of neutralizing the QD core and therefore making the QDs bright again.[93, 94] The "off" times reflect the average lifetime of the photoionized state and can be very long (μs to min.). Similar mechanisms may explain our observation of QD photocharging. From the experimental results presented above, the lifetime of the photocharged state in our PbSe QDs is about 30 s ($1/\gamma_r$), while we find the trion lifetime to be 217 ps and consistent with the blinking model.

The photocharging observed in our TA experiments presented here likely does not involve a fully ionized QD, because the formation of charged QDs depends upon charge stabilization in the solvent. Brus et. al.[95] studied the charging dynamics of CdSe core/shell QDs with electric force microscopy in order to better understand the relationship between the electrical and optical properties and find that charging dynamics do not correlate with QD blinking. They selectively photocharged QD films with visible and UV light and monitored charges over time. The study finds a huge range of behavior in charging dynamics of individual QDs and suggested that structural defects on the surfaces play a role in the mechanism of photo-ionization. They find that when no acceptor site is available in the surrounding media, QDs tend to remain uncharged,[95] suggesting that for a charge to leave the QD, there must be a viable acceptor present. In those experiments, the addition of a ZnO shell greatly reduced charging of

the QDs by passivating the QD surfaces and reducing the number of available trap sites similar to the effect that we find for the $Cd(Oleate)_2$ treatment.

The similarities found between QD blinking experiments and what is studied here make it tempting to assign them to the same mechanism, however, there are some striking differences that make more study a necessity. There are three factors that show blinking to be similar to what is studied here. (1) Both processes can have similarly long lifetimes. (2) There is a clear dependence on surface passivation. Surface traps play a large part in blinking and passivating them causes a near complete suppression of blinking.[88,96-99] Those observations lead to the conclusion that surface states are responsible for the creation of photocharged states, and therefore blinking.[89] Surface states seem to play a role in the photocharging observed here and possibly the MEG efficiency, as can be seen from the effects of the $Cd(Oleate)_2$ treatment. (3) The Auger quenching mechanism, involving the trion and discussed above to explain blinking, can be used to interpret the difference between flowing and static conditions found in our experiments. The lifetime (τ_{2T}) that we extract for the photocharged state (see Figure 3.4.1c, Figure 3.4.2c, Figure 3.4.3c and Figure 3.4.4c) is 2-3 times longer than the bi-exciton lifetime, which is consistent with either a positive or negative trion.

There are also clear differences between blinking and photocharging observed here. There is an energy dependence for the creation of photocharged QDs, with photocharging always appearing at energies above 3.1 eV, which for our experiments corresponds to $h\nu > 3.5\ E_g$ and never when samples are excited below 1.55 eV, or for these experiments, $h\nu < 1.8\ E_g$. In photon intermittency experiments, blinking is observed at all excitation wavelengths (due to material and detector sensitivity, this range has been limited to the visible 1.9-3.1 eV, or $< 2E_g$) down to low excitation intensities. On initial consideration the presence of blinking at low intensity and

excitation energies of 1-2 E_g would seem to suggest that an Auger-ionization process could not be possible for the creation of the off-state. However, Peterson et. al.[100] show that due to the long timescale of blinking experiments, the probability of directly generating a bi-exciton during the duration of an experiment is almost certain, even though the probability of creating bi-excitons is extremely low in each pulse. In our experiments, we find that an Auger-ionization mechanism is not responsible for the creation of photocharged QDs. A direct charge generation mechanism is more appropriate due to the lack evidence for charging with high fluence excitation of 1-2 E_g light. To date, we are aware of no studies of blinking at 3-4 E_g, or at low excitation energy (<1.9 eV), and there are no literature reports of an energy dependent fluorescence intermittency threshold similar to the one outlined above for QD photocharging.

Recently, we measured the QYs for PbSe QD films that had been subjected to different chemical treatments used to produce conductive films (Chapter 5).[32] The QYs reported here compare well with those results. For those measurements, the samples are completely static and therefore the photocharging observed here should be more severe than in QD solutions. However, in all but one case we observed a reduction of the apparent QYs. Since the photocharging investigated here results in an apparent increase of the QY, we conclude that the photocharging investigated in this study does not occur in the films. We saw evidence of static charging in heavily n-doped films produced by soaking PbSe QD films in an ethanol solution of hydrazine, where we estimated dopant concentrations approaching 1 dopant per QD. For these films, we observed a drastic reduction in the first exciton lifetime that we tentatively assigned to non-radiative recombination pathways, similar to the trion pathway discussed here. For hydrazine acetonitrile, methylamine acetonitrile, and untreated films we found QYs that fall on the line reported in Figure 3.4.7. The 1,2-ethanedithiol (EDT) treated films showed a drastic

decrease in QY that was partially assigned to increased QD coupling. Photocharging in films may not occur as efficiently as in solutions for several reasons: (1) the high mobility of carriers may allow for faster regeneration of the photocharged state and (2) differences in surface states induced by the different surface ligands as well as increased QD-QD coupling may reduce the density of acceptor sites. The QY of the ethanol treated films was higher than found in solutions and may indicate similar photocharging, as reported here. Future work will need to understand potential charging effects in QD films. Understanding exciton dynamics and MEG efficiency in electronically coupled QD films is essential for learning how to harness MEG to convert light into electricity with high efficiency.

3.6 Conclusion

This work partially addresses the mechanism by which a variety of studies on similar QDs fail to agree on MEG efficiency. Varying surface qualities and number of trap states present in QD samples lead to the formation of a steady state population of photocharged QDs in pulsed laser experiments. The dynamics of this photocharging have been determined through the use of a laminar flow model and flow rate experiments to show that a generation probability that depends on excitation energy and surface treatment, and a recombination mechanism that is independent of fluence, QD size, excitation energy and surface treatment can adequate explain all the experimental data. Accurate photon-to-exciton QYs can be obtained by not allowing the photocharged state to build up in the pulsed laser experiments, as first proposed by McGuire et al.[4,75] (either through stirring or flowing which we demonstrate reduces the photocharged QD population to approximately zero). Treatment of the surface of the QDs with Cd produced higher PLQYs, reduced photocharging and may lead to increased MEG. These gains can be rationalized by the possibility of an increase in confinement energy of the e^--h^+ pair and better surface

passivation. The relationship with the QD surface, and long lifetime of the photocharged state, is reminiscent of photoluminescence intermittency. While there are some clear correlations between the photocharging observed here and intermittency in QDs, our preliminary experiments suggest that they arise from different mechanisms. The fact that surface treatments and experimental conditions cause differences in the apparent QYs, can explain the variations found in the literature. The QYs reported here indicate that the MEG efficiency is enhanced by a factor of ~ 2 over bulk PbSe.[30] Further increases in the MEG efficiency are needed to make the largest impact on solar energy conversion and therefore, understanding and improving MEG is a significant research challenge. Our findings provide a way to standardize MEG measurements so that they can be easily and accurately compared. The fact that the MEG efficiency was modified with a surface treatment (although modestly) gives substance to the idea that materials can be designed to increase QYs and eventually make better use of the available energy in the solar spectrum.

3.7 Appendix

The TA signal is then given by the following expression,

$$\frac{\Delta T}{T}\left(\tau_p\right) = \exp\left\{-\sigma_{probe} N_{QDs} \int_0^L n_{1s}\left(z,\tau_p\right) dz\right\} - 1 \approx -\sigma_{probe} N_{QDs} \int_0^L n_{1s}\left(z,\tau_p\right) dz \tag{3.28}$$

where we have introduced the occupation of the first exciton level, n_{1s}, which has both a spatial and temporal dependence. The spatial dependence changes with time due to the considerations discussed above. In the absence of long-lived charged states, the first exciton population right after excitation is determined by the excitation fluence and Poisson statistics,

$$n_{1s}\left(z,\tau_p=0\right)=\frac{1}{8}\sum_{m=1}^{8}mP_m\left(z\right)+\sum_{m=9}^{\infty}P_m\left(z\right) \tag{3.29}$$

where $P_m\left(z\right)=\sigma_{pump}J_{pump}\left(z\right)\exp\left[-\sigma_{pump}J_{pump}\left(z\right)\right]/m!$ and $J_{pump}\left(z\right)=J_{pump}^{0}\exp\left(-\sigma_{pump}N_{QDs}z\right)$

where J_{pump}^{0} is the intensity of the pump bean at the front face of the cuvette.

To examine the relative importance of terms in Equation (3.19), and show that accumulation and diffusion terms can be neglected, we introduce dimensionless variables such that each variable ranges from 0 to1 and each derivative is of order of magnitude 1. Grouping of terms results in the appearance of four dimensionless numbers, three Péclet numbers (rate of transport by forced convection / rate of transport by diffusion) and one Damköhler number (rate of reaction / rate of transport by forced convection). Dimensionless variables are indicated with an overbar. These new variables are as follows:

$$\overline{N_T}=\frac{N_T}{N_{QDs}} \tag{3.30}$$

$$\bar{t}=\frac{t}{\tau_c}$$

$$\overline{V_x}=\frac{V_x}{V_{xMax}}$$

$$\overline{X}=\frac{X}{\delta_x}$$

$$\bar{y}=\frac{y}{\delta_y}$$

$$\bar{z}=\frac{z}{\delta_z}$$

$$\overline{R_g}=\frac{R_g}{R_{Max}}$$

$$\overline{R_r}=\frac{R_r}{R_{Max}}$$

In Equation (3.30), τ_c is the time scale for convective replacement of QDs. Since this goes to infinity as $V_x \to 0$, we choose a reasonable "threshold" velocity (V_{th}) for low flow rates and small distances from the wall:

$$\tau_c = \frac{\delta_x}{V_{th}} \quad and \quad V_{th} = \frac{6Q_{\min}(L_z - z_{\min})z_{\min}}{L_y L_z^{\,3}} \tag{3.31}$$

where $Q_{min} \sim 0.0001$ cm^3/s and $Z_{min} \sim 0.1\delta_z \sim 10\mu$m. δ_z is the characteristic depth of penetration of the pump beam defined by $\delta_z = \frac{1}{\alpha}$, approximately 100 um for an O.D. of 4 at the pump wavelength). Substituting the new variables into Equation (3.19) we get:

$$\frac{n}{\tau_c}\frac{\partial \overline{N_T}}{\partial \bar{t}} + \frac{V_x n}{\delta_x}\frac{\partial \overline{N_T}}{\partial \bar{x}} = Dn\left[\frac{1}{\delta_x^{\,2}}\frac{\partial^2 \overline{N_T}}{\partial \bar{x}^2} + \frac{1}{\delta_y^{\,2}}\frac{\partial^2 \overline{N_T}}{\partial \bar{y}^2} + \frac{1}{\delta_z^{\,2}}\frac{\partial^2 \overline{N_T}}{\partial \bar{z}^2}\right] + \overline{R_g}R_{Max} - \overline{R_r}R_{Max} \tag{3.32}$$

After multiplying (3.32) by $\frac{\tau_c}{n}$ and substituting $\frac{\delta_x}{V_{th}}$ for τ_c we are left with:

$$\frac{\partial \overline{N_T}}{\partial \bar{t}} + \frac{V_x}{V_{th}}\frac{\partial \overline{N_T}}{\partial \bar{x}} = \frac{1}{Pe_x}\frac{\partial^2 \overline{N_T}}{\partial \bar{x}^2} + \frac{1}{Pe_y}\frac{\partial^2 \overline{N_T}}{\partial \bar{y}^2} + \frac{1}{Pe_z}\frac{\partial^2 \overline{N_T}}{\partial \bar{z}^2} + Da\left(\overline{R_g} - \overline{R_r}\right) \tag{3.33}$$

Here, each derivative is of order 1. The Péclet and Damköhler numbers are given by:

$$Pe_x = \frac{\delta_x V_{th}}{D} \approx 70 \tag{3.34}$$

$$Pe_y = Pe_x \approx 70 \ (\text{since } \delta_x = \delta_y) \tag{3.35}$$

$$Pe_z = \frac{\delta_z^{\,2} V_{th}}{\delta_x D} \approx 1 \tag{3.36}$$

$$Da = \left(\frac{\delta_x R_{Max}}{n V_{th}}\right) = \left(\frac{k_{Max}}{V_{th}/\delta_x}\right) >> 1 \tag{3.37}$$

Dropping terms that are << 1, it is seen that, to a good approximation, the PDE simplifies to:

$$\frac{\partial \overline{N_T}}{\partial \bar{t}} + \frac{V_x}{V_{th}}\frac{\partial \overline{N_T}}{\partial \bar{x}} = \frac{1}{Pe_z}\frac{\partial^2 \overline{N_T}}{\partial \bar{z}^2} + Da\left(\overline{R_g} - \overline{R_r}\right) \tag{3.38}$$

However, of these four terms, it is seen that two are of order 1 (the accumulation term and the z-diffusion term) while the other two (the reaction and convection terms) are much greater than 1.

$\left(\frac{V_x}{V_{th}}\right) >> 1$ and since the we observe effects of photocharging at all, it is clear that Da is greater than order-of-magnitude 1. Thus, we can further simplify to:

$$\frac{V_x}{V_{th}}\frac{\partial \overline{N_T}}{\partial \overline{x}} = Da\left(\overline{R_g} - \overline{R_r}\right) \tag{3.39}$$

We are only interested in the total number of trapped QDs in the probe beam path, so we integrate over δ_x, δ_y and δ_z. However, $Vx=f(z)$ and R_g and R_r are also functions of z, but we don't need to know the x and y dependence of n_T, so we can go ahead and integrate over x and y.

$$\frac{V_x}{V_{th}}\int_0^1\int_0^1 \frac{\partial \overline{N_T}}{\partial \bar{x}}\, d\bar{x}d\bar{y} = \int_0^1\int_0^1 Da(\overline{R_g} - \overline{R_r})\, d\bar{x}d\bar{y} \tag{3.40}$$

By the Fundamental Theorem of Calculus the LHS is $\left(\frac{V_x}{V_{th}}\right)\overline{N_T}$

$$\frac{V_x}{V_{th}}\overline{N_T} = Da\left(\overline{R_g} - \overline{R_r}\right) \tag{3.41}$$

By substituting the dimensional variables back into equation (3.40) we arrive at equation (3.20).

$$\frac{V_x N_T}{\delta_x} = R_g - R_r \tag{3.42}$$

Supporting Information Available: The supplemental section for reference 31 contains absorbance and photoluminescence spectra for both samples studied here along with the time resolved photoluminescence of the 4.6 nm PbSe. These data, along with the PL quantum yield, were used to determine the radiative and non-radiative rates of these materials, with and without the $Cd(Oleate)_2$ treatment. This section also contains a compilation of literature data for the band

edge alignment of PbSe and CdSe and a discussion about the position of these bands in a core-shell structure. This material is available free of charge via the Internet at http://pubs.acs.org.

Chapter 4: Size Dependence of Multiple Exciton Generation Efficiencies in PbS, PbSe and PbS_xSe_{1-x} Alloy Quantum Dots

4.1 Abstract

Here we report the multiple exciton generation (MEG) efficiencies for several different QD sizes representing bandgaps in the ranges of 0.6 to 1 eV for QD materials consisting of either PbSe, PbS, or a PbS_xSe_{1-x} alloy using ultrafast transient absorption spectroscopy. In previous MEG reports on PbSe QDs, no dependence on the QD size or bandgap were found. Here, we find a clear size dependent MEG efficiency within the strong confinement region for both the PbS and PbS_xSe_{1-x} alloys that depends on the physical size of the quantum dot (QD), and its bandgap. The size-dependent MEG efficiency decreases for larger sizes and results from the decreased quantum confinement in PbS and PbS_xSe_{1-x} compared to PbSe. The decrease in MEG efficiency is correlated with a smaller Bohr exciton radius of PbS. Since MEG is more efficient in PbSe and PbS QDs than their bulk counterparts, a size-dependent MEG efficiency is expected. Different theories predict different forms of this size-dependence, and our measurements provide insight and guidance for the mechanism behind MEG.

4.2 Introduction

Efficient multiple exciton generation (MEG) has been observed in several quantum dot systems, but the lead chalcogenide system (PbX; X=S,Se,Te) has been the most extensively studied. For MEG studies, the lead chalcogenides offer several advantages such as low bandgap, large Bohr exciton radius (46nm in PbSe, 18-20nm in PbS and ~80nm in PbTe),[101,102] good stability, and relatively easy and reproducible synthesis. Furthermore, PbX QDs look promising

for solar applications due to their natural abundance, ease of processing, large carrier mobilities, and large static dielectric constants resulting in low exciton binding energies.

The Bohr exciton radius represents the average distance between the electron and hole for an exciton in a bulk semiconductor, and is determined by the dielectric constant of the material and the effective mass of the electron and hole. The Bohr radius of an exciton in a semiconductor material is calculated using:

$$a_B = \epsilon_\infty \frac{m_e}{m^*} a_0 \tag{4.1}$$

where ϵ_∞ is the optical dielectric constant of the material, m_e is the mass of the electron, m^* is the reduced effective mass of the exciton ($\frac{1}{m^*} = \frac{1}{m_e^*} + \frac{1}{m_h^*}$) and a_0 is the Bohr radius of the hydrogen atom.[103] The Bohr radius is a measure of the volume occupied by the bulk exciton; Therefore, a QD with a radius smaller than a_B, and confined by a high potential (the surface of the quantum dot), will modify the electronic states of the exciton. Size-dependent effects in semiconductor nanocrystals are governed by quantum confinement as well as surface effects, and include increasing bandgap energy that can be tuned across the visible and near IR, relaxation of momentum conservation, increased Auger processes, increased coulomb coupling between electron and hole, increased potential for MEG and many other fundamental intrinsic properties of bulk semiconductors.[2,62,104] Arguments by Efros and Efros utilize the Bohr exciton radius as a measure of the degree of quantum confinement. The strong confinement limit is defined as $R \ll a_B$, and in this regiem, the individual motions of electrons and holes are quantized.[105] This approach uses the ratio of the radius of the crystal (R) to the Bohr radius (a_B) as the "smallness

parameter" that defines the quantum confinement $\left(\lambda = \frac{R}{a_B}\right)$.[106] This parameter is used in determining the Hamiltonian of QDs and we use it here as a measure of quantum confinement.

Typical approaches to tuning opto-electronic properties in bulk semiconductors include alloying. Vegards law states that the properties of the alloyed material are a linear combination of the two constituent elements. Alloying may also increase MEG efficiencies by both providing higher impact-ionization cross sections by disrupting the lattice, and tuning the excited state electronic properties in order to alter relaxation channels.[107,108] Alloys also have the benefit of being able to independently control nanocrystal size and band gap. This is helpful, because designing a system with the correct physical and electronic properties is desirable.

There are several theoretical descriptions of the MEG process and while all include an increased efficiency of quantum confined systems over bulk, only a few have predicted a size dependence in the MEG efficiency within the quantum confined region,[104,109] while the rest have not studied this aspect of the MEG process.[62] We define the MEG efficiency as the ratio between the minimum amount of energy needed to create an electron hole pair (the band gap) and the electron-hole pair creation energy (ε_{EHPM}), or the actual amount of energy needed to produce an additional electron hole pair after the MEG threshold is crossed ($\eta_{EHPM} = E_g/\varepsilon_{EHPM}$).[30] The theoretical picture as to the size dependence of MEG in QDs is murky and to date, experiments have not provided definitive results. The increased confinement found in quantum confined systems when compared to the bulk leads to higher MEG efficiencies, and it is logical that as the size of the QD approaches the bulk, so will the MEG efficiency. However, the size at which this happens is unclear. Calculations done by Rabani et al. on several QD materials (although notably not PbSe or PbS) and calculations on CdSe by Lin et al. show that as the size of the quantum dot increases, the MEG efficiency (η_{EHPM}) should decrease.[104,109] This size dependence has not been

observed in the PbSe system, but with the large Bohr exciton radius of 46nm, all MEG experiments on PbSe used QDs several times smaller than the Bohr exciton radius. However, for PbS, the exciton radius is 18-20 nm, and it is possible to measure MEG in QDs with a radius of 5 nm. The two practical limitations to measuring QDs of larger sizes are that it is difficult to synthesize colloidal QDs due to the solubility of nanocrystals larger than 10 nm in diameter, and as the size of the QD increases, the measurements become more difficult. The absorption cross section increases with size, meaning that lower fluences are needed in order to reach the regime of $\langle N_0 \rangle < 0.1$ and the signal-to-noise ratio becomes too low to make accurate measurements.

4.3 Methods

PbS QDs were synthesized according to the typical hot injection method fond in reference 110. This method allows for a wide range of tunability and a narrow size distribution. The QDs were capped with oleic acid and the photoluminescence quantum yields followed the trend explained in reference 111. PbS_xSe_{1-x} alloy samples were synthesized according to a previously published preparation[73,108] and exact percentages of sulfur and selenium were determined using X-ray diffraction and inductivity coupled plasma atomic emission spectroscopy(ICP-AES). This preparation was determined to produce high quality alloys using Rutherford backscattering spectroscopy and energy filtered TEM, and the sizes of the alloys are calculated by using the sizing curves of PbS and PbSe.[108] The ratio between sulfur and selenium was used to scale these sizing curves and the values were verified by direct observation with TEM. We compare the results of the PbS and PbS_xSe_{1-x} alloys to previously published data for PbSe[5] and PbSe:Cd (Chapter 3).[31] The PbSe:Cd samples are treated with a $Cd(Oleate)_2$ treatment to passivate the surfaces and result in less than a single monolayer of Cd on the surface, but successfully reduce the amount of photocharging present.

Multiple exciton generation yields were determined using ultrafast transient absorption spectroscopy. The experimental setup is described in detail in references 3, 32, 80. Special care was taken to avoid the possibility of photocharging by stirring samples in tetrachloroethylene (TCE). This photocharging has been shown to overestimate the apparent MEG efficiencies due to the repetitive nature of the pulsed laser experiment, unless the samples are either stirred or flowed so that a significant population of photocharged QDs do not accumulate (Chapter 3).[4,31] In order to determine the photon-to-exciton quantum yields (QYs), the 1st exciton bleach dynamics for a variety of excitation fluences are measured with a temporal resolution of ~ 100 fs and the transient are collected until a pump-probe delay time of at least 3 times the biexciton lifetime. From these transients, the ratio of the transient bleach (reduction of interband absorption) at early pump-probe delay times to the respective signal at long pump-probe delay times was extracted. The bleach at early pump-probe delays is proportional to the number of excitons produced by the laser pulse while at long delay times it is proportional to the total number of QDs excited by the laser pulse.[3,77] The bleach at late pump-probe delay times ($\tau_p > 3\tau_2$) is a measure of the bleach after all multiple excitons have decayed through Auger recombination, while the single excitons have not had time to decay. We label the ratio of the transient bleach at early times to late times as, R_{pop} , because this ratio is proportional to the average number of excitons created within each excited QD. We correct for any decay in the single excitons over this time by comparing the R_{pop} value found below the MEG threshold to the R_{pop} above the MEG threshold. We find that by reducing the photon fluence of the excitation pulse so that $\langle N_0 \rangle < 0.1$ while stirring, we are able to extract the correct photon-to-exciton QY, while reducing the contribution from photocharging. If $R_{pop} > 1$ for these low photon fluences, single photons absorbed in a QD must have created multiple excitons. For each of the samples

studied a set of TA traces was taken below 2*Eg* and at least one set was taken above 3*Eg* in order to determine the MEG efficiency. More detail on how this data is analyzed is shown in Chapter 2.[30]

4.4 Results

Figure 4.4.1 shows the absorbance data for all of the PbS and PbS_xSe_{1-x} samples studied. These samples were chosen so that a wide range of bandgaps and physical sizes were studied for both the PbS and the PbS_xSe_{1-x} QDs. The percentage of sulfur is included on Figure 4.4.1a, and both graphs show the MEG efficiency (η_{EHPM}) of each sample. Table 4.4.1 contains a more detailed list of the different samples studied along with their size (calculated from sizing curves), bandgaps, percentages of sulfur and selenium, photon-to-exciton QY at a given bandgap multiple, the MEG efficiency (η_{EHPM}) of each sample and the threshold onset rate adjusted efficiency (η'_{EHPM}). These efficiencies are derived and explained in detail in Chapter 2[30] Several things should be noticed about Table 4.4.1. First, it is important to realize that for similar bandgap energies, the PbS QDs are larger than either PbSe or the PbS_xSe_{1-x} alloys, due to the relatively small bulk bandgap of PbSe. The two ways to design alloys with varying bandgaps are to either vary the size of the QD or the percentage of sulfur to selenium. Adding more sulfur increases the bandgap of the QD, while an increased selenium concentration will lower the bandgap. Second, while the photon-to-exciton quantum yield (MEG) measures how well a particular material behaves when excited at a certain energy, the MEG efficiencies (η_{EHPM} and η'_{EHPM}) serve as a measure of how efficiently a material can convert a high energy photon into two or more excitons of lower energy.[30] Finally, it is important to notice that for all

sizes of PbSe, the efficiency (η_{EHPM}) does not change dramatically, while for PbS and PbS_xSe_{1-x} the efficiency decreases as the size of the QD increases.

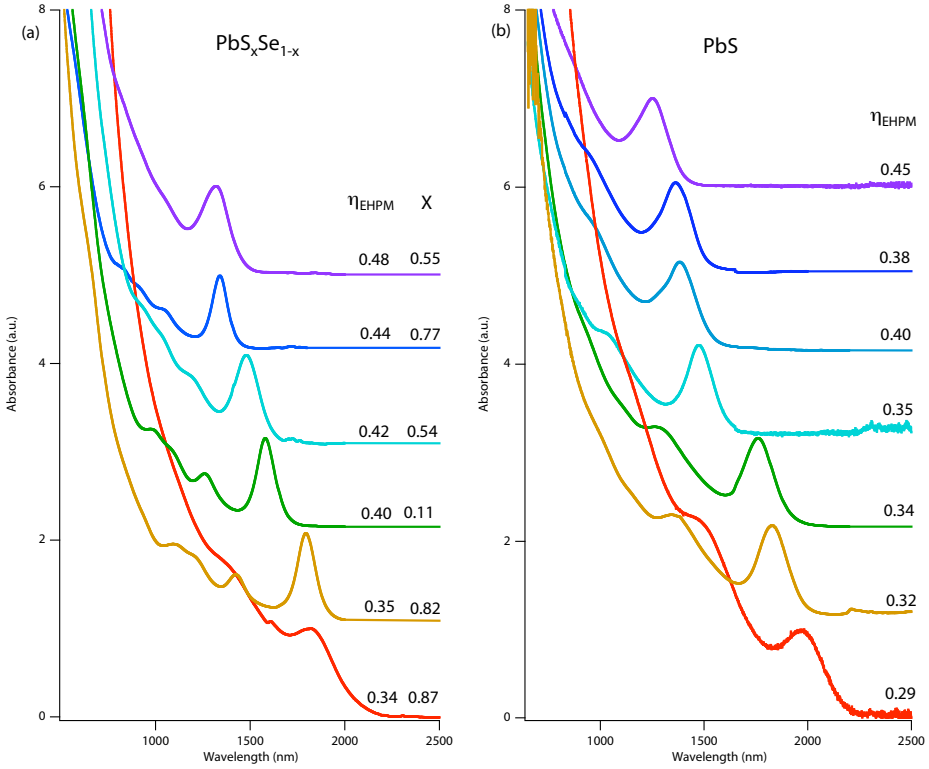

Figure 4.4.1: Absorbance Data of Pbs and PbS_xSe_{1-x} Samples Studied
Absorbance data are shown for (a) PbS_xSe_{1-x} alloy samples along with the MEG efficiency (η_{EHPM}) and the percentage of sulfur in each sample, and (b) PbS.

Table 4.4.1: MEG Data for PbSe, PbS, PbS_xSe_{1-x} Samples Studied
List of samples studied at NREL, their composition, size and bandgap along with the photon-to-exciton QY found in each case at a given bandgap multiple and the MEG efficiency (η_{EHPM}) and threshold adjusted efficiency (η'_{EHPM}) for each sample.

Sample	Size (nm)	E_g (eV)	QY (± STD)	$h\nu/E_g$	η_{EHPM}	η'_{EHPM}
PbSe	4.1	0.89	1.20 (0.05)	3.7	0.44	0.65
			1.55 (0.05)	4.5		
PbSe:Cd	4.0	0.91	1.27 (0.05)	3.7	0.47	0.69
			1.64 (0.02)	4.4		
PbSe:Cd	6.4	0.66	1.61 (0.05)	4.7	0.42	0.63
			1.95 (0.05)	5.7		
PbS	4.2	0.99	1.02 (0.02)	3.1	0.45	0.63
			1.26 (0.03)	3.8		
PbS	4.8	0.91	1.04 (0.02)	3.4	0.38	0.55

			1.21 (0.03)	4.2		
PbS	5.0	0.90	1.24 (0.03)	4.1	0.40	0.59
PbS	5.5	0.84	1.06 (0.02)	3.7	0.35	0.55
			1.23 (0.03)	4.5		
PbS	7.6	0.70	1.18 (0.03)	4.4	0.34	0.53
			1.51 (0.03)	5.3		
PbS	8.1	0.68	1.18 (0.03)	4.6	0.32	0.49
PbS	9.4	0.64	1.09 (0.03)	4.9	0.29	0.44
			1.36 (0.08)	5.9		
$PbS_{55}Se_{45}$	4.3	0.93	1.10 (0.02)	3.4	0.48	0.67
			1.52 (0.03)	4.1		
$PbS_{77}Se_{23}$	4.5	0.93	1.33 (0.03)	4.0	0.44	0.64
$PbS_{54}Se_{46}$	5.1	0.84	1.14 (0.03)	3.7	0.42	0.59
			1.35 (0.03)	4.5		
$PbS_{11}Se_{89}$	6.2	0.69	1.40 (0.03)	4.5	0.40	0.61
			1.80 (0.03)	5.5		
$PbS_{82}Se_{18}$	7.9	0.68	1.30 (0.03)	4.6	0.35	0.54
			1.51 (0.05)	5.5		
$PbS_{87}se_{13}$	8.0	0.68	125 (0.05)	4.6	0.34	0.45
			150 (0.08)	5.5		

Figure 4.4.2 displays the MEG efficiency of the PbS and PbS_xSe_{1-x} samples studied at NREL, PbSe samples from Chapter 5,[31] PbS data on four of the same samples made at NREL from Los Alamos National Laboratory,[7] along with several PbSe samples studied at TU Delft.[5] The first thing to note in this graph (and in Table 4.4.1) is that all of the PbSe and PbSe:Cd samples studied have a very similar efficiency (within the standard deviation) and are consistent with previous results for all sizes studied.[4,5,7,31,75] Second, we find that the PbS samples do not show similar MEG efficiencies for all sizes. Plotted in this fashion it is difficult to recognize any trends in the measured QYs. However, upon careful examination of the data, it is clear that **Error! Reference source not found.** does not provide sufficient information, for while this sort of graph is sufficient for PbSe and other samples with relatively size independent efficiencies, the changes in efficiency with size seen is PbS and PbS_xSe_{1-x} are difficult to discern. In order to aid in clarifying this data, the size and color of each data point represents the QD size relative to

the Bohr radius (r/a_B). The size-dependence is explained in detail in the discussion section. For the smallest size of PbS (0.99 eV and 4.2nm) the yield is very similar to PbSe QDs with a similar bandgap, however, for the 7.6, 8.1 and 9.4 nm samples, the yield is considerable lower than PbSe. This is confusing considering the fact that PbS and PbSe are so similar in structure and electronic properties. The fact that the impact ionization efficiency for bulk PbS ($\eta'_{EHPM} = 0.45$) is higher than bulk PbSe ($\eta'_{EHPM} = 0.31$) would also suggest that the MEG efficiency of PbSe QDs should be lower than PbS, not higher. These discrepancies are resolved by looking at the major differences between these two materials.

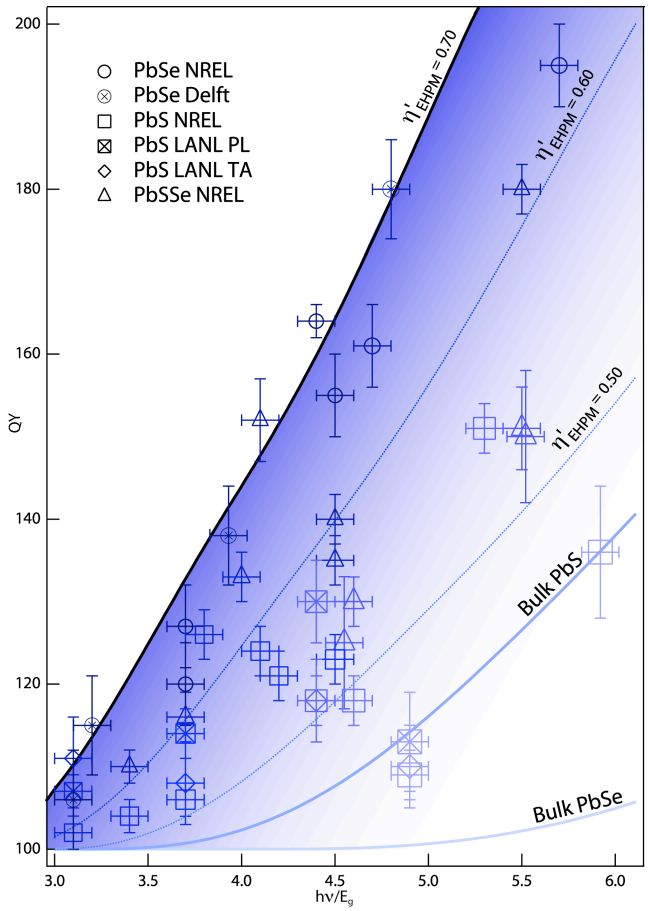

Figure 4.4.2: PbS, PbSe, PbS_xSe_{1-x} Photon-to-Exciton Quantum Yields
Photon-to-exciton quantum yields for several samples of quantum dots and alloy QDs plotted verses the photon energy relative to the bandgap of the material. While there looks to be a large amount of scatter in the data, this can be explained by the different sizes of PbS and PbS_xSe_{1-x} and their respective MEG efficiencies. The size and color

of the data points represents the normalized size of the QD, with larger and lighter data points representing a larger normalized size. The fit lines show where a range of efficiencies (η'_{EHPM}) would fall. PbSe data from TU Delft is from reference 5 and LANL PbS data is from reference 7.

4.5 Discussion

To explain the decrease in efficiency with size, it is helpful to examine the MEG efficiencies plotted verses their physical size and verses their relative size when compared to the Bohr exciton radius (Figure 4.5.1). The MEG efficiency of each QD sample was determined by fitting the R_{pop} ratios at multiple wavelengths to Equation (4.2).

$$QY = \left(\frac{h\nu}{E_g} - 1\right)\eta_{EHPM} \tag{4.2}$$

(η'_{EHPM}) was calculated using a similar, but more complicated formula that takes into account the competition between the carrier cooling rate and the electron hole pair multiplication rate that is explained in Chapter 2.[30] When these competing channels are taken into account, the result is an equation that depends on the rate of carrier cooling and the rate of MEG. In Figure 4.5.1a, we find a clear different size verses efficiency curve for each material. The MEG efficiency is relatively size-independent for the PbSe QDs, but for PbS QDs, as the size increases, the efficiency drops in a linear fashion. A similar trend is observed with the alloys, however, the efficiency is effected by size to a lesser extent than the PbS. The 4.3 nm alloy has the same QY as several of the PbSe samples and within the error bars, it is difficult to say which sample is more efficient. However, for the 5.1, 6.2, 7.9 and 8.0 nm samples, the MEG efficiency is much closer to the PbS than the PbSe. This is particularly interesting for the 6.2 nm $PbS_{11}Se_{89}$ sample, which contains only 11% sulfur. A similar size PbSe sample at the same wavelength showed 161% MEG compared to 140% for the alloy. There may be many reasons for this size dependence, but because of the similarities between PbS and PbSe, the one that stands out is the significantly smaller Bohr exciton radius of 18-20nm for PbS compared to 46nm for PbSe. This

would seem to suggest that as the PbS size increases, it becomes closer to the bulk material and loses some of its MEG enhancement. To explore this possibility, Figure 4.5.1b shows the efficiency of the different samples plotted verse smallness parameter $\left(\lambda = \frac{R}{a_B}\right)$. We calculated the smallness parameter of the PbS and PbSe by dividing the size of the QD by the Bohr radius of the material, which signifies the relative amount of confinement, with smaller numbers signifying more confinement. For the alloy system, we calculated the Bohr radius by using a weighted reciprocal average of the Bohr radius of PbS and PbSe based on their respective percentages in the alloy. From this graph, it is clear that the MEG efficiency is dependent on smallness parameter. For the PbSe system, the changes are small enough that without the trend seen in the PbS and PbS_xSe_{1-x}, these variations are easily attributed to noise, however, there is a clear trend in the data that follows the relationship across all lead chalcogenide samples studied.

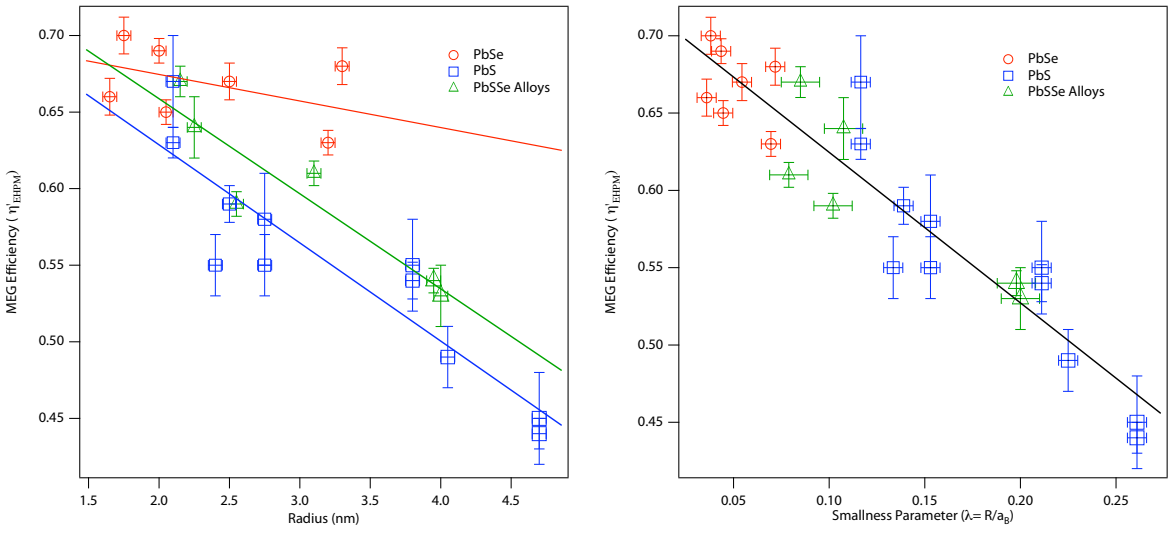

Figure 4.5.1:MEG Efficiency Verses Size and Smallness Parameter
(a) MEG efficiency plotted verses QD size for PbS, PbSe, and PbS_xSe_{1-x}. Note that for all sizes, the PbSe efficiency does not change dramatically, but for both the PbS and PbS_xSe_{1-x}, the efficiency decreases with increasing size. (b) When comparing the MEG efficiency to the smallness parameter (the size of the particle divided by the Bohr exciton radius) we see that a linear relationship exists for all materials studied. For fitting purposes, (η'_{EHPM}) is used over (η_{EHPM}) so the lower QY data is fit more accurately, but both efficiencies yield similar results.

One of the major components of the Bohr exciton radius is the dielectric constant. The dielectric constant depends on the frequency of the incident field and the motion it inspires and is generally discussed at the two extremes. The low frequency, or static dielectric constant (ϵ_s) describes the background screening provided by the charged neucli in the lattice, while the optical (or electronic) dielectric constant (ϵ_∞) is the real part of the dielectric constant that describes the electronic screening caused by the electron cloud in the material.[112] Since the motions of electrons and atoms are on drastically different time scales, typically the motion of one of the two is neglected, although the dielectric constant can be calculated at any frequency. For calculating the bulk Bohr radius in semiconductors, the optical dielectric constant is used since the absorption of photons and the excitation of electrons and the screening provided by the other electrons in the material are the primary concerns. Starting with the Penn model,[113,114] theory has suggested a size-dependent static dielectric constant (ϵ_s) and a few experiments[115] have confirmed this theory. The static dielectric constant depends on the structure of the material, however, experiments and theory show that the optical dielectric constant (ϵ_∞) displays no size-dependence in lead chalcogenide quantum dots.[112] For this paper, we calculate the Bohr exciton radius using the optical dielectric constant and assume that (ϵ_∞) does not change for quantum confined systems. The scarce experimental results agree with this assumption, but it should be noted that the Bohr exciton radius is not used to calculate an imperial value for the amount of confinement found in this system, but instead as a way to describe the changes in electronic properties with size as seen between PbS and PbSe. Because of this fact, any conclusions drawn in this paper using the smallness parameter are valid even if the dielectric constant changes with size as long as those changes are consistent between PbS and PbSe. We feel that the Bohr radius relationship developed here is a more accurate way to describe all of the

differences that come with quantum confinement, because the Bohr radius is a natural measure of the confinement of the electron and hole wavefunctions and incorporates the mass of electron and hole, any changes in dielectric constant and the changes in coulomb coupling due to changes in QD size and bandgap.

The mechanism behind the proportional relationship between MEG efficiency and confinement is unclear, but there are several logical explanations. First, logic predicts that as the QD size approaches the bulk, the MEG efficiency will also approach the impact ionization (II) efficiency in bulk. While this is a broad explanation, at some size, a QD must become a small piece of bulk material and the electronic properties will follow suit. Second, increasing confinement leads to increasing coulomb interactions, increased splitting between energy levels,[15] a slowed radiative recombination rate,[23,64] or phonon bottleneck, and an increased Auger rate.[2,15] All of these are predicted to be the causes behind the increased MEG efficiency found in QDs compared to II in bulk and so the increase of all of these should lead to more efficient MEG. These arguments are backed up by theoretical calculations that also predict that MEG should depend on QD size.

Some of the more complete theoretical calculations available (using a Green's function formalism) on multiple exciton generation in semiconductor QDs show that a size dependence is expected in these systems.[104] In this study by Rabani et al. of CdSe, Si and InAs QDs, a size dependence in the efficiency was observed due to increased confinement seen in smaller systems. The values seen in these systems do not agree with the experimental results seen in PbS, PbSe and PbS_xSe_{1-x}, however this would not be expected due to the differences in electronic structure of these materials. This theory does predict that when the rate for the transformation of the excitonic state into a biexcitonic state becomes larger than the radiative decay rate, then

MEG will become efficient. This happens at the energy where the biexciton density of states exceeds the single exciton density of states (DOS). While the biexciton DOS stays fairly constant for all sizes examined, the single exciton DOS increases with the size of the QD.[104] This increase in the single exciton DOS can be explained decreasing confinement leading to a more bulk like band structure where there is less separation in between states and more of a continuous distribution of states and in turn leads to a decrease in MEG efficiency in larger QDs. Following this reasoning, Trinh et al. suggest that some core shell and Alloy QDs would have lower MEG efficiencies than PbSe due to an increased density of calculated single exctiton states.[5]

The theoretical work of Rabani et al. was expanded on by Lin et al. in a recent paper on the size dependence of MEG rates in CdSe calculated using an atomistic pseudopotential. This work built on that of Rabani et al. by examining larger QDs, including spin-orbit coupling and including excitonic interactions in order to calculate MEG rates.[109] The conclusion is similar to Rabani et al. in that the MEG rate is found to depend on the volume of the QD, with larger QDs leading to a slower MEG rate at a given normalized photon energy, but more detail is provided in determining that fact. This size dependence was attributed to a competition between the coulomb coupling and the density of trion states (the final state in the MEG process). In CdSe, the main contribution to the MEG rate is found to be the density of negative trion states (formed due to the relaxation of a high energy electron through MEG) due to the larger amount of energy transferred to the electron in the absorption of a photon. However, hole states are found to have a much higher MEG rate at a given energy, they simply do not acquire as much energy in CdSe due to the effective masses of the carriers. This paper suggests that by using Auger processes to transfer the electron energy to the hole, the overall MEG rate could be increased.[109] Since the

effective masses of carriers in PbS and PbSe are much more similar, this situation would be different, but he size dependent effects should still hold.

4.6 Conclusion

This paper measures the multiple exciton generation efficiencies of PbS and PbS_xSe_{1-x} alloy samples over a wide range of sizes and compositions and compares those results to previous results on PbSe. We find that unlike previous results, a size dependence over the strong confinement regime clearly exists in the MEG efficiency that seems to depend on the amount of confinement that exists in the QD. PbSe also seems to follow this trend, but due to the large Bohr exciton radius, it is difficult to measure samples with a large enough diameter to see this trend clearly emerge. We attribute this size dependence to the decreasing confinement seen in larger QD samples as the diameter of the QD approaches the Bohr exciton radius. This is shown in the linear relationship found between the smallness parameter of the QD and the MEG efficiency (η'_{EHPM}) of the material (Figure 4.5.1b). The exact mechanism behind this relationship is unclear, but the are many explanations that can be used to explain this result. All of the factors governing the increase of MEG efficiency in QDs over II in bulk are simply amplified with increased confinement and experimentally verifying these results adds validity to some of the theories behind MEG. Our hope is that these results will shed light on the mechanism of MEG and eventually lead to a better understanding of how to develop materials that are more efficient at collecting energy from the solar spectrum.

Chapter 5: Variations in the Quantum Efficiency of Multiple Exciton Generation for a Series of Chemically-Treated PbSe Nanocrystal Films

5.1 Abstract

We study multiple exciton generation (MEG) in two series of chemically-treated PbSe nanocrystal (NC) films. We find that the average number of excitons produced per absorbed photon varies between 1.0 and 2.4 (± 0.2) at a photon energy of ~$4E_g$ for films consisting of 3.7 nm NCs, and between 1.1 and 1.6 (± 0.1) at hν ~$5E_g$ for films consisting of 7.4 nm NCs. The variations in MEG depend upon the chemical treatment used to electronically couple the NCs in each film. The single and multi-exciton lifetimes also change with the chemical treatment: biexciton lifetimes increase with stronger inter-NC electronic coupling and exciton delocalization, while single exciton lifetimes decrease after most treatments relative to the same NCs in solution. Single exciton lifetimes are particularly affected by surface treatments that dope the films *n*-type, which we tentatively attribute to an Auger recombination process between a single exciton and an electron produced by ionization of the dopant donor. These results imply that a better understanding of the effects of surface chemistry on film doping, NC carrier dynamics, and inter-NC interactions is necessary to build solar energy conversion devices that can harvest the multiple carriers produced by MEG. Our results show that the MEG efficiency is very sensitive to the condition of the NC surface, and suggest that the wide range of MEG efficiencies reported in the recent literature may be a result of uncontrolled differences in NC surface chemistry.

5.2 Introduction

Multiple exciton generation (MEG) in semiconductor nanocrystals (NCs) (also called quantum dots (QDs)) can produce *n* excitons for each absorbed photon possessing an energy of at least *n* multiples of the band gap energy (E_g), where *n* is an integer.[1,2,35] If multi-exciton formation, dissociation and charge collection are simultaneously efficient, the resulting enhanced photocurrent can increase solar energy conversion efficiencies.[3,53] Recently, we reported a

Schottky-junction photovoltaic device based on a thin film of colloidal PbSe NCs that demonstrated a power conversion efficiency of >2% and a short-circuit current density, J_{SC}, greater than 20 mA cm^{-2}.[84] The NC film in this device was treated with 1,2-ethanedithiol (EDT) in acetonitrile in a layer-by-layer procedure to produce a conductive NC film.[116] Excitons are created, separated, and transported all within the single-component NC film. The internal quantum efficiency (IQE), defined as the fraction of photons absorbed by the NCs that produce carriers in the external circuit, was found to be as high as 0.8, indicating efficient charge separation and transport.[117] However, no evidence was found in the IQE spectra to suggest that multiple charge carriers were collected per absorbed photon. To harvest MEG excitons from a NC film, the inter-NC charge transfer event that produces free electrons and holes must be faster than Auger recombination (non-radiative exciton annihilation), which typically occurs in 10-100 ps. In addition, the chemical treatments that are used to produce the conductive films must not degrade the MEG efficiency. We therefore conclude that either the EDT treatment quenches the MEG process or that multi-exciton recombination is faster than inter-NC charge transfer (requiring exciton dissociation and charge separation).

In a previous report, we found that soaking PbSe NC films in a solution of 1 M hydrazine (hy) in acetonitrile (CH_3CN) produces conductive films without degrading MEG.[80] Here, we extend that work to the EDT CH_3CN treatment and three other chemical treatments that produce conductive PbSe NC solids: hy in ethanol (EtOH), methylamine (me) in EtOH, and pure EtOH.[78] We show by ultrafast transient bleaching that EDT treatments almost completely quench MEG compared to pristine NC films prepared without any chemical treatment. Quenching of the MEG process by EDT explains why our previous device measurements failed to show MEG-enhanced photocurrent. Finally, we find that the exciton quantum yield (QY) reproducibly *increases* when films of 3.7 nm diameter NCs are treated in pure EtOH, while films with 7.4 nm NCs do not show such an increase.

We measure MEG by acquiring fast transients indicative of multi-exciton states - which are short lived compared to single exciton states - and relating the magnitude of the fast component relative to the long-lived component to the number of multi-excitons in the system.[35,42] Transient absorption (TA) spectroscopy is a convenient technique with which to measure exciton population dynamics. Chapter 1 discusses this experiment in detail. Other time-

resolved spectroscopies have also been employed to study MEG, including time-resolved photoluminescence (TRPL)[44,48] and time-resolved THz spectroscopy (TRTS),[46] which measures the intra-band photoinduced absorption.[118] These experimental probes provide complimentary information. In general, TA provides a better measure of the carrier population dynamics than does TRPL because of its less restrictive selection rules.

Recent reports in the literature disagree as to the efficiency of MEG in several NC systems. For example, one study employing TA on InAs/CdSe/ZnSe core/shell/shell NCs did not find appreciable MEG,[50] despite previous results from some of the same authors demonstrating very efficient MEG in this system using three techniques (TA, TRTS and a quasi-cw PL technique).[46] Later the same group reported that their original TRTS results could not be reproduced on a new set of similarly prepared samples,[49] without mentioning whether the TA or the quasi-cw results also could not be reproduced. This apparent retraction and the later independent TA study are in contradiction to a TA study from Schaller and Kilmov[6] showing enhanced QYs in InAs/ZnSe core/shell NCs, but with a lower efficiency than found in the original Pijpers report.[46] Similarly, using TRPL, Nair et al.[48] are unable to reproduce the large quantum yields in CdSe NCs reported by Schaller and Klimov.[44] Recently Nair et al. measured enhanced QYs in PbSe and PbS NCs employing TRPL,[39] but reported that MEG occurs at a lower efficiency than reported previously.[1,35,37]

These disagreements have cast doubt on the universality of MEG in NCs, and suggest that sample-dependent phenomena may be responsible. It is conceivable that the surfaces of the NCs, which are not well characterized, controlled or understood - can modulate the efficiency of the MEG process. It is known that surfaces of NCs have a large impact on their photo-physical properties. Carrier relaxation,[64,65] and carrier dynamics[119] are affected by the surface ligands. Surface chemistry also determines the electrical properties of NC films, dictating in part the carrier doping level, mobility, and whether the films exhibit *n*- or *p*-type transport.[78,83,116,119] To date no generally accepted theory has emerged to explain all of the MEG experimental findings.[3] Since surface preparation can drastically modulate the carrier cooling rates, it is reasonable to conclude that MEG may also depend on the detailed chemistry and interactions at the NC surfaces. In the Shabaev-Efros-Nozik (SEN) MEG model,[62] enhanced QYs are determined by the relative dephasing rates of single and multi-exciton states that mix and form a coherent

superposition of states through the multi-electron Coulomb interaction. While measuring the dephasing rate of multi-exciton states is experimentally challenging, the dephasing rate of single exciton states has been shown to depend upon the surface ligands.[120] If dephasing rates depend on surface interactions, then MEG should also depend on surface interactions in the SEN model.

To date, no report has shown an absence of MEG in lead salt NCs; in fact a recent report from a group independent of those previously reporting on MEG confirms MEG in PbSe NCs.[37] We found a large variation in the enhanced QYs in our original paper on PbSe and PbS NCs.[1] Understanding the variations in QYs and reconciling the different InAs, PbSe, PbS and CdSe NC results will enable a deeper understanding of the fundamental MEG process and may provide prospects for increased solar energy conversion efficiencies. Ben Lu-Lu et. al.[50] rule out differences in experimental methods as the source of the different QYs for InAs-core NCs and suggest that the different NC structures - a core/shell$_1$/shell$_2$ versus just a core/shell - might explain the lack of measurable MEG with respect to the results of Schaller et.al.[6] While these authors consider sample-to-sample variations as a possible contributor in their irreproducible results, they do not think this plays a significant role. In a recent report,[4] McGuire et al. propose that uncontrolled, long-lived NC charging due to a low probability NC photoionization event may be the cause of the variations in the reported MEG efficiencies due to an accumulation of charged NCs over multiple laser shots. However, even when eliminating these extraneous effects by vigorously stirring of their samples, they report QYs higher than that found by Nair et al.[39] However, a careful TA study by Trinh et al.[37] did not find evidence for NC charging. In this report we have focused on NC films and show that very different MEG efficiencies are measured depending on how the NC films are prepared.

5.3 Results

We measured the multi-exciton dynamics of two series of PbSe NC films, consisting of either 3.7 nm or 7.4 nm diameter NCs (first exciton transitions at 1310 nm and 2040 nm in tetrachloroethylene (TCE), respectively). The NCs were prepared according to published procedures[78] and films in each series were prepared from NCs produced in the same reaction. The NC films were spin cast directly onto the sapphire windows of 1.33" ConFlat viewports from 350 mg mL^{-1} octane solutions in a nitrogen-filled glove box. Each film was then immersed

in one of the following solutions for the following time: 0.02 M EDT in CH_3CN for 3 minutes, or overnight in 1 M hy in CH_3CN, 1 M hy in EtOH, 1 M me in EtOH, or pure EtOH. After treatment, the films were allowed to dry in the glove box and then sealed together with a second, uncoated ConFlat viewport to create an airtight sample cell that can remain outside of the glove box for several weeks without measurable change in the optical properties of the treated films. The basic characterization of these films is described in detail elsewhere.[78,116] The size of the NCs is not affected by these chemical treatments.[78] By investigating MEG for this series of film treatments, we hope to gain a better understanding of the overall factors that can enhance or reduce MEG.

Figure 5.3.1 shows the optical density near the first exciton transition for the 3.7 nm and 7.4 nm NC films (the traces have been offset for clarity). While not shown here, the treated films experience an offset in their optical extinction due to scattering by cracking induced by loss of the oleate capping ligand during film treatment. Light scattering is also responsible for the negative slope on the red side of the first exciton transition. We consistently observe a red-shift of the first exciton transition after chemical treatment due to a combination of changes in dielectric screening and inter-NC electronic coupling,[78,116] and a reduction in optical extinction at high photon energies relative to low photon energies, which we mainly attribute to a reduced dielectric screening as the discontinuity of the dielectric constant at the surface of the NC, $\varepsilon_{in}/\varepsilon_{out}$, is reduced.[116] The photoluminescence (PL) spectra of the 3.7 nm NC films are displayed in Figure 5.3.1a, but we did not measure the PL from the 7.4 nm NC films due to detector limitations. The photoluminescence quantum yields (PLQYs) of the 3.7 nm NC films are substantially lower than those of the NCs dispersed in TCE, with the PLQY roughly inversely proportional to the inter-NC separation previously determined by small-angle X-ray scattering.[78] We display the PL normalized to the peak of the first exciton absorbance and do not attempt to quantify the absolute values of the film PLQYs. PL could not be detected from the hy EtOH treated films.

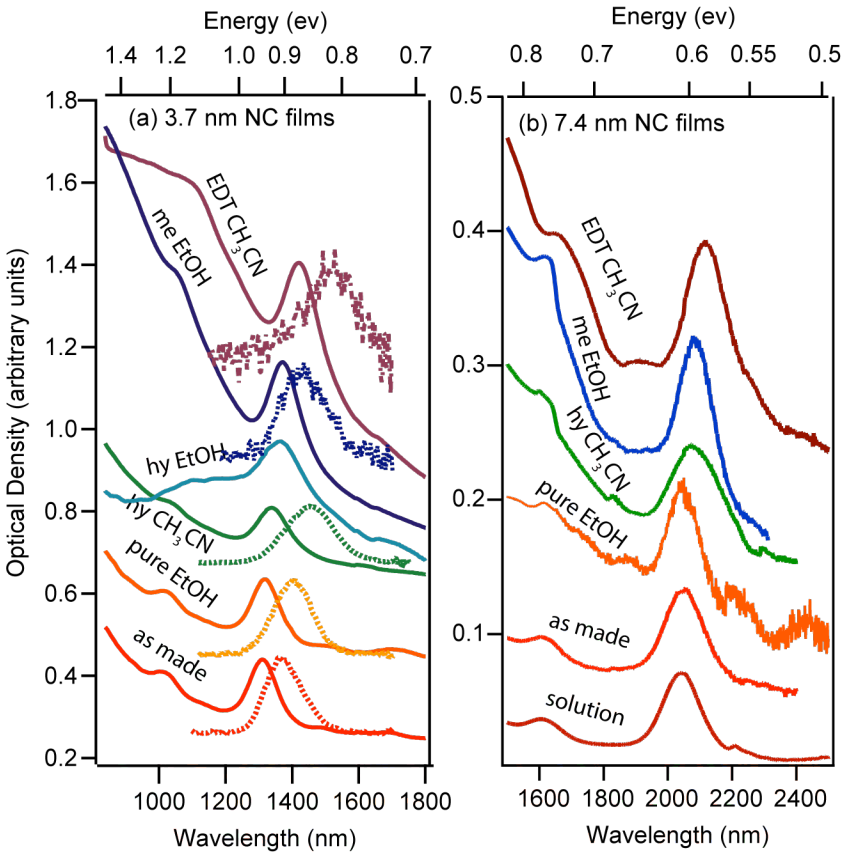

Figure 5.3.1: Extinction Spectra of PbSe NC Films
(a) 3.7 nm NCs (first exciton transition in TCE of 1310 nm) and (b) 7.4 nm NCs (first exciton transition in TCE of 2040 nm). Traces are offset for clarity. In (a) we also display the PL of the films. The PL is not reported for the large sized NC.

To measure MEG in the 3.7 nm NC films, we study the intensity-dependent interband TA bleach decays upon photoexciting with either 800 nm or 330 nm light, which corresponds to ~1.6 E_g and ~4 E_g. For the 7.4 nm NC films, we measured the transient bleaching after photoexciting at 1300 nm and 400 nm, which corresponds to ~1.6 E_g and ~5 E_g . In all cases, the band edge bleach is monitored at the peak of the first exciton absorption. The experimental apparatus is described in detail elsewhere.[3,80] Experiments with excitation light below that of the MEG threshold (~2 E_g) allow us to obtain the single and biexciton lifetimes, and also the absorption cross section, σ_a. An exact knowledge of σ_a is not necessary to determine MEG. This is a critical feature of the data analysis because in the films the optical extinction may not be linearly related to σ_a at all wavelengths, due to wavelength-dependent scattering. To circumvent this complication, we measure the dependence of the carrier dynamics on pump fluences which, as we have shown previously,[3,42,80] enables analysis that is insensitive to the exact knowledge of σ_a.

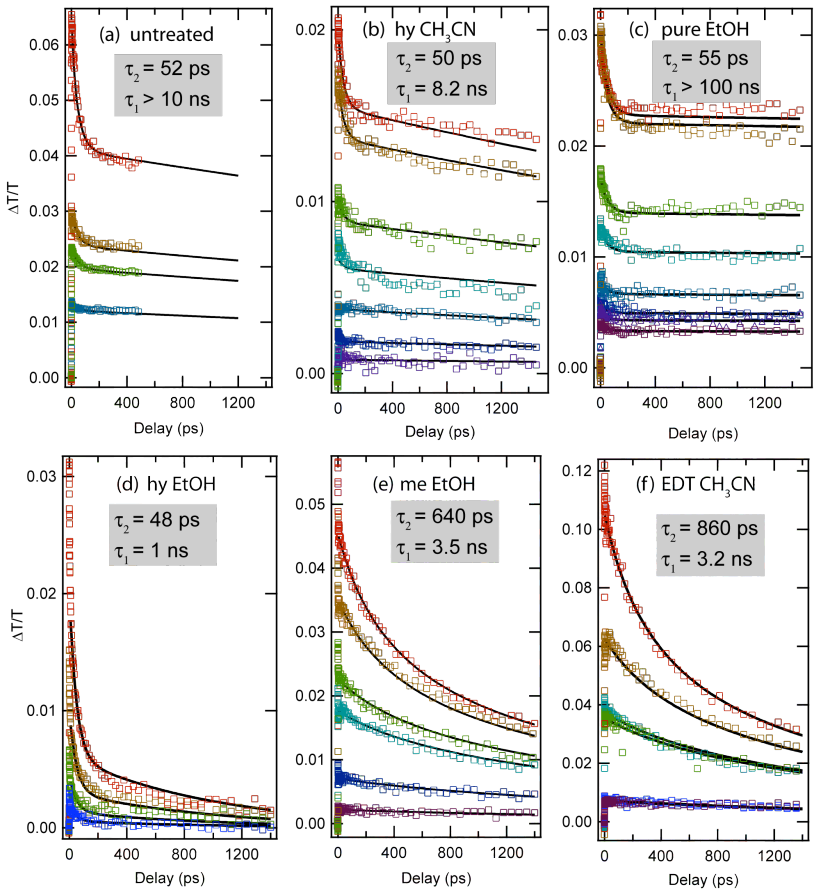

Figure 5.3.2: Intensity-Dependent Bandedge Bleach Dynamics for 3.7 nm NC films.
The films were photoexcited at λ_{pump} = 800 nm which is < $2E_g$. The open squares are the data points and the lines are the global fit described in the text. All data sets are modeled with the Auger recombination model discussed in the text except for the hy EtOH. The biexciton lifetime for these NCs in solution is ~45ps. For each film we report the average number of excitons per NC excited,$\langle N_o \rangle$. (a) untreated, $\langle N_o \rangle$ = 0.22, 0.39, 0.49, 1.09 (b) hy CH_3CN, $\langle N_o \rangle$ = 0.022, 0.052, 0.11, 0.18, 0.28, 0.47, 0.54 (c) pure EtOH, $\langle N_o \rangle$ = 0.046, 0.06, 0.068, 0.093, 0.15, 0.207, 0.35, 0.36 (d) hy EtOH, fits to a bi-exponential function whose shape is independent of excitation fluence. (e) me EtOH, $\langle N_o \rangle$ = 0.088, 0.287, 0.72, 0.92, 1.42, 1.84 and (f) EDT CH_3CN, $\langle N_o \rangle$ = 0.185, 0.188, 0.19, 0.92, 0.98, 1.63, 2.76.

The intensity-dependent carrier dynamics for photoexcitation of the 3.7 nm PbSe NC films at 800 nm are shown in Figure 5.3.2. Figure 5.3.3 displays the transients for the 7.4 nm NC films with excitation light at 1300 nm. We maintain a low excitation density so that the average exciton density per NC, $\langle N_o \rangle$ at the front of the sample for the various incident photon fluences is low, ranging from < 0.02 to < 2 in Figure 5.3.2 and Figure 5.3.3. This ensures that the average number of excitons per NC within the excitation volume is also low for shorter wavelengths with higher optical densities. Higher excitation intensities were found to gradually and irreversibly alter the decay dynamics over the course of the experiment, indicating photo-damage of the samples. To avoid such damage, each transient was averaged over at least two traces. If scan-to-

scan reproducibility was not satisfactory, the resulting traces were not used in the analysis and another spot on the film was tested at a lower pump fluence. Using low photon densities also ensured that non-linearities in $\Delta T/T$ did not complicate our analyses. All of the data were reproduced several times on each film and on at least two different films prepared at different times.

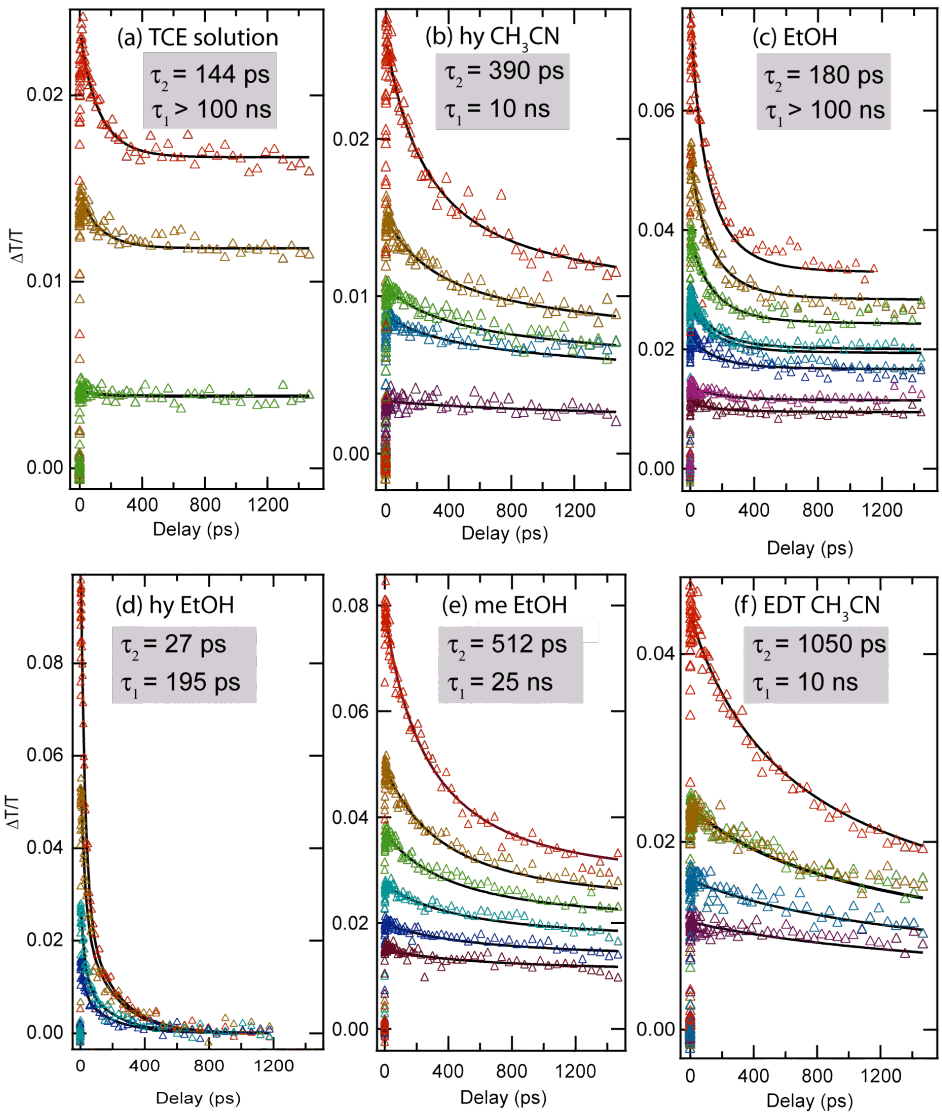

Figure 5.3.3: Intensity-Dependent Dynamics of 7.4 nm NC films
λ_{pump} = 1300 nm, (a) solution of NCs in TCE, <N_0> = 0.13, 0.46, 0.74 (b) hy CH_3CN, <N_0> = 0.195, 0.51, 0.61, 0.87, 1.5 and (c) EtOH, <N_0> = 0.25, 0.41, 0.54, 0.74, 1.0, 2.1 (d) hy EtOH, the dynamics are characterized by a 195 ps time constant and a faster 27 ps component at high photon fluences (e) me EtOH, <N_0> = 0.29, 0.58, 0.71, 1.0, 1.4, 2.0 (f) EDT CH_3CN, <N_0> = 0.54, 0.75, 1.1, 2.1

Each set of data is modeled using a global fitting routine that incorporates Auger recombination (AR) and is described in detail elsewhere.[1,3] Within the global fitting routine the single exciton lifetime (τ_1) and biexciton lifetime (τ_2) are varied globally across the entire data set; the best fit values are tabulated in Table 5.3.1 and Table 5.3.2 and noted in Figure 5.3.2 and Figure 5.3.3. There are three important changes that occur for the treated films relative to NCs dispersed in solution: (1) The single-exciton lifetime decreases for each of the chemical treatments except pure EtOH, reflecting an increased rate of surface recombination (2) the bi-exciton lifetime increases as the inter-NC distance decreases, and (3) the absorption cross section per NC increases for films with longer biexciton lifetimes. These observations are consistent with our previous findings for drop-cast hy CH_3CN treated films.[80]

The hy EtOH treated films show drastically shorter single-exciton lifetimes than the other treated films. The 3.7 nm NC films shows bi-exponential decay with 48 ps and 1000 ps components, but neither component shows the variation with intensity indicative of biexciton decay. The first exciton lifetime decreased to ~195 ps for the 7.4 nm NC films and a fast 27 ps component appears with higher pump fluence, indicative of a fast biexciton component. The 48 and 195 ps decays are roughly equal to that of the biexciton lifetimes found for the respective uncoupled NC films. As a result, we can tentatively assign this rapid decay to an Auger process involving a single exciton interacting with a charge carrier created by an ionized dopant. The hy EtOH treatment produces heavily *n*-type films (see below), with an estimated carrier density equivalent to ~1 electron per NC. The only other *n*-type films in the series are the hy CH_3CN treated films, which apparently have a lower electron concentration and thus do not suffer from such pronounced Auger recombination. The short lifetimes of the hy EtOH films precluded measurements of their MEG efficiency by TA.

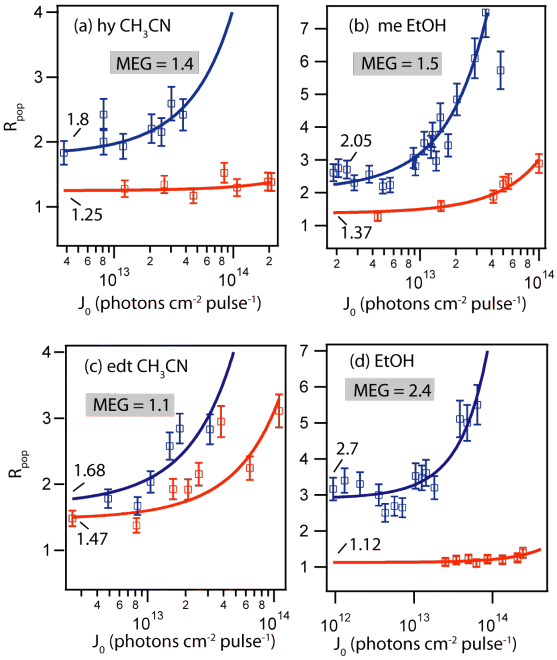

Figure 5.3.4: MEG Results for the 3.7 nm NC Films.
Blue squares are for excitation at 330 nm (~4 E_g) and red squares are for excitation at 800 nm (~1.6 E_g). The solid lines are best fits of Equation (5.1). (a) hy CH_3CN (b) me EtOH, (c) EDT CH_3CN, (d) EtOH

In Figure 5.3.4 and Figure 5.3.5 we display the ratio, R_{pop}, of the TA signal at early times (2 ps) and late times (1500 ps). These data are modeled with Poison statistics as previously described;[42,80] this analysis yields the following relationship,

$$R_{pop} = \frac{J_0 \sigma_{pump} \delta \cdot QY}{\left(1 - \exp\left(-J_0 \sigma_{pump}\right)\right)} \qquad (5.1)$$

where J_0 is the input photon fluence, σ_{pump} is the absorption cross section per NC at the pump wavelength, and $\delta = \exp\left[\left(t_{late} - t_{early}\right)/\tau_1\right]$ accounts for the decay of the single exciton. The y-intercept for the sub-MEG threshold excitation (red squares are the data points and the red line is the best fit values) are indicative of the decay of the first exciton and determine δ. The ratio of the y-intercept for above-MEG threshold (blue squares are the data points and the best fit is the blue line) and sub-MEG threshold determines the QY, this is equivalent to holding δ fixed at the value determined by fitting the sub-MEG threshold data and floating QY in Equation (5.1). For the hy CH_3CN treated 3.7 nm NC film, the QY is 1.8/1.25 = 1.4±0.1. The 3.7 nm NCs suspended in TCE and the untreated film (data not shown) showed QYs of ~1.5±0.1. The me CH_3CN and hy CH_3CN treated 3.7 nm NC films show QYs unchanged from the untreated NCs,

in agreement with our previous findings. However, the EDT CH_3CN and the pure EtOH 3.7 nm NC treated films show substantially different QYs of 1.1±0.1 and 2.4±0.2, respectively.

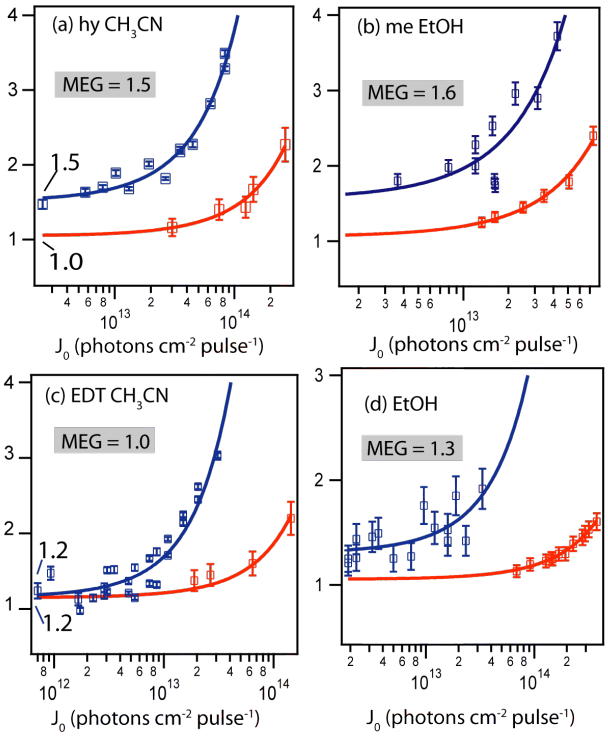

Figure 5.3.5: MEG Results for the 7.4 NC Films.
Blue is for 400nm excitation (~5 E_g) and red is for 1300 nm excitation (~1.6 E_g) (a) hy CH_3CN, (b)me EtOH (c) EDT CH_3CN and (d) EtOH.

Figure 5.3.5 presents the MEG results for the 7.4 nm NC films treated with hy CH_3CN, me EtOH, EDT CH_3CN, and EtOH: results for the NCs in TCE and the as-made films can be found in the supplemental section. We find similar behavior to the 3.7 nm NC films for the EDT CH_3CN treatment: MEG is largely quenched. For the hy CH_3CN, me EtOH, and the untreated 7.4 nm NC films we find that MEG is reduced compared to the NCs in solution, with QY = 1.5-1.6 in the films compared to 2.2(±0.1) for the isolated NCs. In contrast to the smaller NCs where EtOH treatment produced the highest MEG efficiency (QY = 2.4), the EtOH-treated larger NCs showed a QY of 1.3(±0.1), slightly reduced relative to the other films. In each case the results indicate a reduction in MEG for the larger NCs relative to the same film treatments for the smaller NCs. Figure 5.3.6 compiles the MEG results from this study with our previous results. The blue open circles are data taken for 4.0 nm NCs and the red circles are for larger NCs, 4.7 and 5.7 nm diameters. The open green circles are data reproduced from Schaller et al.[40] for isolated PbSe NCs.

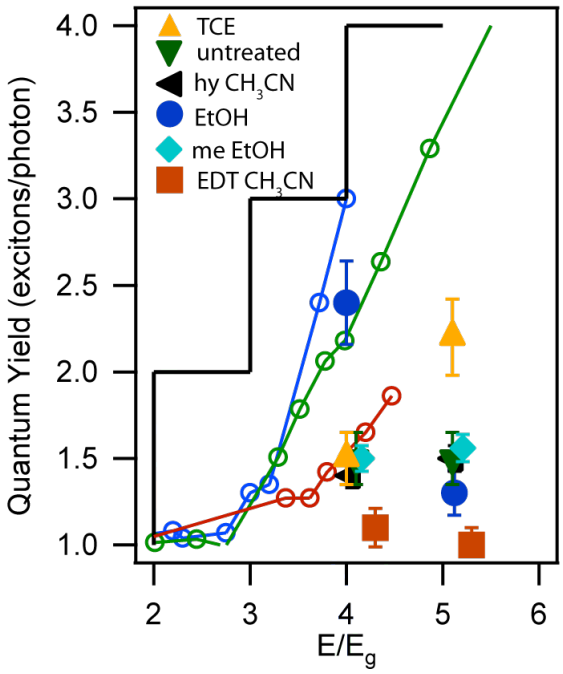

Figure 5.3.6 MEG QYs for Films and Solutions
QYs as determined in this work (solid symbols) overlaid with past QYs of PbSe NCs dispersed in solution from NREL, reference[1]. Blue open circles correspond to results for 4.0 nm NCs in TCE and the red open circles are average results for 4.7 nm and 5.7 nm NCs in TCE. In our original report some variation on either sample preparation or NC size was observed. The green open circles are reported from LANL, reference[6]. The solid black line represents the maximum possible MEG efficiency; achieving *n* excitons at *n* times the band gap energy.

The percentage of oleate removed after treatment from small and large NCs was quantified by an FTIR analysis (see supplemental section) and is similar to that reported earlier for 6.5 nm NC treated films.[78,116] We find agreement with our previous findings for the EDT CH_3CN, me EtOH, and hy EtOH treatments and no significant dependence on the NC size. However, we consistently find larger oleate loss for the hy CH_3CN treatment, 30-35% in this study versus only 2-7% in our previous findings. We also find a size-dependent oleate loss for both the hy CH_3CN and pure EtOH treatments. Thus, while the large NCs treated with EtOH show consistent results with our previous findings, the smaller NCs lose more oleate, 50% vs. 15-20%. The effect of hy CH_3CN treatment is also size-dependent; the smaller NCs lose 60-70% while the larger NCs lose 30-35%. In our earlier report the loss of oleate was correlated with a decrease in inter-NC separation, quantified by small-angle X-ray scattering. We assume here that the trends in changes to the inter-NC separation are the same as found in our earlier studies. We repeated our earlier electrical characterization to determine if film conductivity depends on NC size. We are able to reproduce the earlier results[78,116] for all of the film treatments except EDT CH_3CN, where we observe an order of magnitude higher conductivity (see supplemental section for a comparison of our recent measurements with those reported previously). We consistently observe higher conductivities for the larger NCs compared to the smaller NCs, however the trends in the conductivity with chemical treatment are size-independent. Table 5.3.1

and Table 5.3.2 summarizes the MEG results, single and biexciton lifetimes, conductivities, and the change in inter-NC separation for the small and large NCs, respectively.

Table 5.3.1 Compilation of Results for 3.7 nm NC Films

Δd (nm) is the change in inter-NC distance and represents the NCs moving closer together due to loss of the capping ligand, oleate. The average inter-NC distance in the untreated film is ~ 1.8 nm. *These results were obtained from Luther et al.[116] and Law et al.[78]

Treatment	%Oleate removed	σ Ω^{-1}cm^{-1}	Δd (nm)*	Type	τ_1	τ_2	QY
Solution	--	--	--	--	>10 ns	45 ps	1.5 (±0.1)
untreated	--	< 1 x10^{-9}	0.0	--	> 10 ns	52 ps	1.5 (±0.1)
hy CH_3CN	60-70	6x10^{-3}	0.8	n	8.2 ns	50 ps	1.4 (±0.1)
hy EtOH	85-90	2x10^{-3}	1.0	n	48ps/1000ps	----	NA
me EtOH	80-85	1x10^{-5}	0.9	p	3.5 ns	640 ps	1.5 (±0.1)
EtOH	40-50	2x10^{-5}	0.55	p	>100 ns	55 ps	2.4 (±0.2)
EDT CH_3CN	99-100	7 x10^{-4}	1.8	p	3.2 ns	862 ps	1.1 (±0.1)

Table 5.3.2Compilation of Results for 7.4 nm NC Films.

*These results were obtained from Luther et al.[116] and Law et al.[78]

Treatment	%Oleate removed	σ Ω^{-1}cm^{-1}	Δd (nm)*	Type	τ_1	τ_2	QY
Solution	--	--	--	--	> 100 ns	144 ps	2.2(±0.1)
untreated		< 1 x10^{-9}	0.0	--	5 ns	150 ps	1.5(±0.1)
hy CH_3CN	30-35	3x10^{-2}	0.8	n	10 ns	390 ps	1.5 (±0.1)
hy EtOH	85-90	2x10^{-2}	1.0	n	195ps/27ps	----	NA
me EtOH	80-85	1x10^{-4}	0.9	p	25 ns	512 ps	1.6 (±0.1)
EtOH	15-20	3x10^{-3}	0.55	p	>100 ns	180 ps	1.3 (±0.2)

EDT CH_3CN	99-100	$4x10^{-3}$	1.8	p	10 ns	1050 ps	1.0 (±0.1)

5.4 Discussion

There are at least three ways in which the various chemical treatments can affect MEG: (1) changes in the surface chemistry which affect NC-ligand interactions, and subsequently exciton relaxation rates, (2) doping of the NCs causing enhanced Auger recombination, and (3) an increase in inter-NC coupling producing diminished quantum confinement, and/or charge-transfer states with higher carrier mobilities and lower inter-NC charge-transfer barriers. While the present study cannot distinguish which of these is most important to MEG, we can gain insight by discussing the trends.

The variations in MEG are not correlated with the fraction of oleate removed from the NC films by the chemical treatments. For instance, the me EtOH treated films result in an 80-90% loss of oleate while the hy CH_3CN treatment results in 33% oleate loss: however, MEG is about the same in the two films. Moreover, the 3.7 nm EtOH film loses 40-50% compared to only 15-20% for the larger NCs, while MEG is enhanced in the smaller NCs and reduced in the larger NCs. The me EtOH and hy EtOH treatments remove about the same amount of oleate and cause a similar reduction in the inter-NC spacing. However, the electrical properties and carrier dynamics are vastly different after these two treatments. The hy EtOH treatment produces *n*-type films with large conductivities and fast single-exciton decay while me EtOH produces *p*-type films with lower conductivities and only slightly reduced single-exciton decays. As the loss of oleate in itself is insufficient to determine the either electrical behavior of the films, the carrier dynamics, or MEG, we conclude that other factors such as inter-NC separation or the chemical reactivity of the treatments are more important.

The chemical treatments do more than simply remove oleate from the NCs. Of the four treatments, hydrazine is the strongest reducing agent. Treating the films in pure hy or a concentration substantially higher than 1 M yields measurable metallic Pb in the film.[78] Hydrazine therefore tends to reduce surface Pb^{2+} to produce *n*-type films. While methylamine is a reducing agent, it is apparently unable to reduce the surface Pb^{2+} as efficiently as hydrazine. P-type films may result if the as-produced NCs are p-type, which can be the case if the NCs are Se-rich. Treatments may also produce *p*-type films by partially oxidizing the NC surfaces. The

identity of the NC surface species after chemical treatment, whether adsorbates, vacancies or other surface states, is difficult to ascertain and quantify. Small amounts of impurities in the EtOH or other chemical treatments such as residual water may alter the inter-NC coupling through lowering of barrier heights for efficient transport and/or oxidizing or reducing surface Pb or Se ions. The precise nature of the resulting surface species may dictate much of the electrical and carrier dynamics observed here. A small defect concentration, corresponding to only 1 defect site in 10 to 100 NCs, could produce large changes in the measured conductivities. For the EDT CH_3CN treated films producing p-type conductivity, an estimate of the carrier concentration has been obtained through Mott-Schottky analysis[84] yielding carrier densities of ~ 10^{16} to 10^{17} cm^{-3}. These carrier densities correspond to approximately 1 dopant in 10- 100 NCs, which agrees with an estimate of the carrier doping levels in similarly prepared hy CH_3CN treated films.[121] The conductivity of the hy EtOH treatments are an order of magnitude higher; therefore, the dopant density is likely higher, yielding values approaching 1 dopant per NC. Such low amounts of surface doping are very difficult to measure using standard techniques such as FTIR and XPS.[78] A 3.7 nm NC has approximately 1000 surface atoms, requiring detection of 1 part in 1000. To highlight this point we draw attention to measurements on hy CH_3CH treated films that show no evidence for hy in the FTIR or XPS analysis after treatment. Upon heating, the film switches from *n*-type to *p*-type as the small amount of hy (or other absorbates) is desorbed form the film. N-type conductivity is restored upon retreating the film with hy CH_3CN.[78] The amount of hy that is desorbed and then readsorbed is smaller than our detection limits.

Carrier concentrations approaching 1 dopant per NC could result in new Auger recombination pathways for non-radiative recombination of single excitons, and may explain the fast decays observed in the hy EtOH films as discussed previously. We do not see evidence for this mechanism in the hy CH_3CN treated films which are also *n*-type and have similarly high conductivities. The reason for this difference is unknown but may suggest a different mechanism for the fast decays in the hy EtOH treated films. It is important to note here that charged NCs, if present, would cause a fast decay in the single-exciton dynamics that is photon-energy independent. MEG causes a fast decay in the apparent single-exciton dynamics that is photon-energy dependent, the fast component is larger at higher photon energies. The small amount of static charges (produced by doping) in the film does not appear to influence the optical data in any of the films except perhaps the hy EtOH film. *Transient* charging of the films due to

photoionization appears not to play a significant role in these results. The MEG efficiency of all of the films except the EtOH-treated film decreased or remained the same as the NCs in solution. It is not apparent how transient charging of the NCs could account for an apparent reduction in MEG efficiency. It may be that low probability ionization events such as proposed by McGuire et al.[4] do not produce long-lived charged states in these films due to the high mobility of carriers.

While MEG is not correlated with loss of oleate, the MEG efficiency does correlate with the change in inter-NC distance for both NC sizes, with smaller NC separation coinciding with lower MEG yields. Figure 5.4.1a plots the QY versus the change in inter-NC distance created by the various film treatments. This correlation could arise due to an increase in inter-NC electronic coupling that bypasses or inhibits the MEG process. As neighboring NCs couple more strongly to one another, quantum confinement could be reduced sufficiently to greatly decrease the Coulomb coupling necessary to drive the MEG process. Furthermore, charge-transfer states, where the electron resides on one NC and the hole on an adjacent NC, could become lower in energy than highly excited single exciton states isolated on single NCs, as an example see reference 122. In a model that treats MEG, excitation at higher photon energies would result in a mixture of charge-transfer states, single exciton states and multi-exciton states and the interplay between these states could decrease MEG by rapid population of charge-transfer states. The final state of the system and hence any enhanced QYs would then be determined by the relative dephasing and carrier cooling rates within the different channels that include the charge-transfer states. Recently we reported that the IQE of solar cells constructed from PbSe NC films treated with EDT CH_3CN decreases in the IR region of the spectrum, suggesting the existence of a branching ratio between excitonic states and charge-transfer states that depends on the photon energy.[117] This observation suggests that the formation of charge-transfer states competes with exciton cooling which occurs on a ps timescale and therefore provides tentative evidence that charge-transfer states could also play a role in the decreased MEG efficiency. A similar situation arises in molecular solids of pentacene where charge-transfer states can be directly photoexcited despite weak inter-molecular interactions.[123] More work is needed to fully understand these observations and will be the topic of future reports.

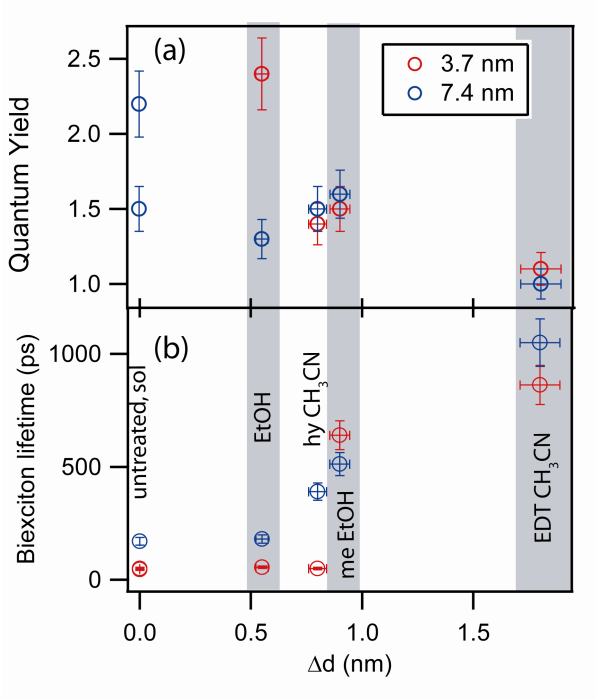

Figure 5.4.1: General Film Data Trends
Correlation of QY (a) and biexciton lifetime (b) with the change in average inter-NC distance for the 3.7 nm NC films (red circles) and 7.4 nm NC films (blue circles).

In support of the above conclusions, the increase in biexciton lifetime, τ_2, is also correlated to the change in inter-NC distance (see Figure 5.4.1b). The increase of τ_2 with smaller inter-NC separation indicates a reduced Auger recombination rate. We attribute this to a delocalization of the excitons due to increased electronic coupling between NCs. The increased τ_2 is greatest for the EDT CH_3CN treated film, where τ_2 increases by an order of magnitude relative to untreated films. The red-shift in the first exciton and the decrease in the inter-NC spacing are also largest for the EDT-treated films. The me EtOH treated films also a show substantially increased τ_2. Consistent with our previous findings, the biexciton lifetimes of the hy CH_3CN treated films increases for the larger NCs, from 150 to 390 ps, while only increasing slightly for the smaller NCs[80] We conclude that electronic coupling is strongest in the EDT CH_3CN, followed by me EtOH, hy CH_3CN, and finally the EtOH films. This roughly correlates with the MEG efficiency, suggesting a trade-off between MEG and strong electronic coupling accompanied by reduced quantum confinement.

The results for the EtOH treated films, while showing roughly the correlation with inter-NC distance, also demonstrate anomalous behavior. The MEG efficiency is greatly increased in the smaller NC films, while it decreases in the larger NC films. While the biexciton lifetime of the EtOH treated smaller NCs remains approximately the same as for the untreated NCs, the single exciton lifetime increases, suggesting that the surfaces are better passivated. It is unclear why the EtOH treatment increases the surface passivation as a significant amount of oleate is removed. Some evidence of either absorbed molecular ethanol and/or ethoxide on the NC surfaces was found,[78] and these species could account for the better passivation relative to oleate. The increased surface passivation may partially explain the increase in MEG observed in the

smaller NCs. In contrast, the larger NCs lose less oleate with a concomitant lower MEG. The effect on the single-exciton lifetime of the EtOH on the larger NCs is hard to ascertain given the 1.2 ns time window used here. The fact that the EtOH treated films show anomalous behavior suggest that the issues governing MEG are still unresolved and require further study with careful control over doping and intimate knowledge of the NC surfaces.

5.5 Conclusion

In conclusion, we have measured MEG by transient absorption in a series of chemically-treated conductive PbSe NC films. We observe a large variation in the MEG efficiency depending on the NC size and the chemical treatment. The decrease in MEG with smaller inter-NC distance may indicate that reduced quantum confinement and/or an increased inter-NC coupling diminish the MEG process. This large sensitivity of the QYs to conditions at the NC surface suggests that recent disagreements over the magnitude of the QYs of various colloidal NC systems may stem from uncontrolled differences in NC surface chemistry. Our results, combined with recent demonstrations that solar cells with large photocurrents can be fabricated from PbSe NCs,[84,124] provide an incentive to study the surfaces of NCs in detail, with the specific goal of understanding how different ligands and surface states affect carrier dynamics and electrical transport within NC films. A better understanding of how the NC surfaces modulate the electrical properties, carrier dynamics and MEG efficiency is clearly desired in order to design systems that harness MEG to convert light into electricity with very high efficiency.

References

(1) Ellingson, R. J.; Beard, M. C.; Johnson, J. C.; Yu, P.; Micic, O. I.; Nozik, A. J.; Shabaev, A.; Efros, A. L. *Nano Lett*. **2005**, *5*, 865.

(2) Nozik, A. J. *Physica E* **2002**, *14*, 115.

(3) Beard, M. C.; Ellingson, R. J. *Laser & Photon. Rev.,* **2008**, *2*, 377.

(4) McGuire, J. A.; Joo, J.; Pietryga, J. M.; Schaller, R. D.; Klimov, V. I. *Acc. Chem. Res*. **2008**, *41*, 1810.

(5) Trinh, M. T.; Polak, L.; Schins, J. M.; Houtepen, A. J.; Vaxenburg, R.; Maikov, G. I.; Grinbom, G.; Midgett, A. G.; Luther, J. M.; Beard, M. C.; Nozik, A. J.; Bonn, M.; Lifshitz, E.; Siebbeles, L. D. A. *Nano Letters* **2011**, 4, 1623.

(6) Schaller, R. D.; Pietryga, J. M.; Klimov, V. I. *Nano Lett*. **2007**, *7*, 3469.

(7) Stewart, J. T.; Padilha, P. A.; Midgett, A. G.; Qazilbash, M.; Pietryga, J. M.; Luther, J. M.; Beard, M. C.; Nozik, A. J.; Klimov, V. I. **2011**.

(8) Hemminger, J.; Crabtree, G.; Kastner, M. In *A Report from the Basic Energy Sciences Advisory Commitee*; Energy, U. S. D. **2008**.

(9) Lewis, N. S.; Nocera, D. G. *Proceedings of the National Academy of Sciences* **2006**, *103*, 15729.

(10) Hillhouse, H. W.; Beard, M. C. *Current Opinion in Colloid & Interface Science* **2009**, *14*, 245.

(11) Nelson, J. *The Physics of Solar Cells*; Imperial College Press: London, **2003**.

(12) Shockley, W.; Queisser, H. J. *J. Appl. Phys*. **1961**, *32*, 510.

(13) Henry, C. H. *Journal of Applied Physics* **1980**, *51*, 4494.

(14) Boudreaux, D. S.; Williams, F.; Nozik, A. J. *J. Appl. Phys*. **1980**, *51*, 2158.

(15) Nozik, A. J. *Annu. Rev. Phys. Chem*. **2001**, *52*, 193.

(16) Klimov, V. I., Mikhailovsky, A. A., McBranch, D. W., Leatherdale, C. A., Bawendi, M. G. *Science* **2000**, *287*, 1011.

(17) Chatterji, D. *The Theory of Auger Transitions*; Academic Press: London, **1976**.

(18) Efros, A. L.; Kharchenko, V. A.; Rosen, M. *Solid State Commun*. **1995**, *93*, 281.

(19) Chepic, D. I.; Efros, A. L.; Ekimov, A. I.; Ivanov, M. G.; Kharchenko, V. A.; Kudriavtsev, I. A.; Yazeva, T. V. *J. Lumin*. **1990**, *47*, 113.

(20) Pietryga, J. M.; Zhuravlev, K. K.; Whitehead, M.; Klimov, V. I.; Schaller, R. D. *Physical Review Letters* **2008**, *101*, 217401.

(21) Alivisatos, A. P. *J. Phys. Chem*. **1996**, *100*, 13226.

(22) Rogach, A. L. *Semiconductor Nanocrystal Quantum Dots*; SpringerWien: New York, **2008**.

(23) Blackburn, J. L., Ellingson, R. J., Micic, O. I., Nozik, A. J. *J. Phys. Chem. B* **2003**, *107*, 102.

(24) Cho, B.; Peters, W. K.; Hill, R. J.; Courtney, T. L.; Jonas, D. M. *Nano Letters* **2010**, *10*, 2498.

(25) Brus, L. E. *The Journal of Chemical Physics* **1984**, *80*, 4403.

(26) Chepic, D. I.; Efros, A. L.; Ekimov, A. I.; Ivanov, M. G.; Kharchenko, V. A.; Kudriavtsev, I. A.; Yazeva, T. V. *Journal of Luminescence* **1990**, *47*, 113.

(27) Kang, I.; Wise, F. W. *J. Opt. Soc. Am. B* **1997**, *14*, 1632.

(28) Woggon, U. *Optical Properties of Semiconductor Quantum Dots*; Springer, **1996**.

(29) Levine, I. N. *Quantum Chemistry*; 5th ed.; Prentice Hall: N.Y., **2000**.

(30) Beard, M. C.; Midgett, A. G.; Hanna, M. C.; Luther, J. M.; Hughes, B. K.; Nozik, A. J. *Nano Lett.* **2010**, *10*, 3019.

(31) Midgett, A. G.; Hillhouse, H. W.; Hughes, B. K.; Nozik, A. J.; Beard, M. C. *The Journal of Physical Chemistry C* **2010**, *114*, 17486.

(32) Beard, M. C.; Midgett, A. G.; Law, M.; Semonin, O. E.; Ellingson, R. J.; Nozik, A. J. *Nano Lett.* **2009**, *9*, 836.

(33) Robbins, D. J. *Physica Status Solidi B-Basic Research* **1980**, *97*, 9.

(34) Landsberg, P. T. *Recombination in Semiconductors*; Cambridge University Press: Cambridge, **1991**.

(35) Schaller, R.; Klimov, V. *Phys. Rev. Lett.* **2004**, *92*, 186601.

(36) Califano, M.; Zunger, A.; Franceschetti, A. *Appl. Phys. Lett.* **2004**, *84*, 2409.

(37) Trinh, M. T.; Houtepen, A. J.; Schins, J. M.; Hanrath, T.; Piris, J.; Knulst, W.; Goossens, A.; Siebbeles, L. D. A. *Nano Lett.* **2008**, *8*, 1713.

(38) Ji, M.; Park, S.; Conner, S. T.; Mokari, T.; Cui, Y.; Gaffney, K. J. *Nano Lett.* **2009**, *9*, 1217.

(39) Nair, G.; Geyer, S. M.; Chang, L. Y.; Bawendi, M. G. *Phys. Rev. B* **2008**, *78*, 10.

(40) Schaller, R. D.; Sykora, M.; Pietryga, J. M.; Klimov, V. I. *Nano Lett.* **2006**, *6*, 424.

(41) Murphy, J. E.; Beard, M. C.; Norman, A. G.; Ahrenkiel, S. P.; Johnson, J. C.; Yu, P.; Micic, O. I.; Ellingson, R. J.; Nozik, A. J. *J. Am. Chem. Soc.* **2006**, *128*, 3241.

(42) Beard, M. C.; Knutsen, K. P.; Yu, P. R.; Luther, J. M.; Song, Q.; Metzger, W. K.; Ellingson, R. J.; Nozik, A. J. *Nano Lett.* **2007**, *7*, 2506.

(43) Schaller, R. D.; Petruska, M. A.; Klimov, V. I. *App. Phys. Lett.* **2005**, *87*, 253102.

(44) Schaller, R. D.; Sykora, M.; Jeong, S.; Klimov, V. I. *J. Phys. Chem. B* **2006**, *110*, 25332.

(45) Gachet, D.; Avidan, A.; Pinkas, I.; Oron, D. *Nano Lett.* **2009**, *10*, 164.

(46) Pijpers, J. J. H.; Hendry, E.; Milder, M. T. W.; Fanciulli, R.; Savolainen, J.; Herek, J. L.; Vanmaekelbergh, D.; Ruhman, S.; Mocatta, D.; Oron, D.; Aharoni, A.; Banin, U.; Bonn, M. *J. Phys. Chem. C* **2007**, *111*, 4146.

(47) Stubbs, S. K.; Hardman, S. J. O.; Graham, D. M.; Spencer, B. F.; Flavell, W. R.; Glarvey, P.; Masala, O.; Pickett, N. L.; Binks, D. J. *Phys. Rev. B* **2010**, *81*, 081303.

(48) Nair, G.; Bawendi, M. G. *Phys. Rev. B* **2007**, *76*, 081304.

(49) Pijpers, J. J. H.; Hendry, E.; Milder, M. T. W.; Fanciulli, R.; Savolainen, J.; Herek, J. L.; Vanmaekelbergh, D.; Ruhman, S.; Mocatta, D.; Oron, D.; Aharoni, A.; Banin, U.; Bonn, M. *Journal of Physical Chemistry C* **2008**, *112*, 4783.

(50) Ben-Lulu, M.; Mocatta, D.; Bonn, M.; Banin, U.; Ruhman, S. *Nano Letters* **2008**, *8*, 1207.

(51) Pijpers, J. J. H.; Ulbricht, R.; Tielrooij, K. J.; Osherov, A.; Golan, Y.; Delerue, C.; Allan, G.; Bonn, M. *Nat Phys* **2009**, *11, 811*.

(52) Ross, R. T.; Nozik, A. J. *J. Appl. Phys.* **1982**, *53*, 3813.

(53) Hanna, M. C.; Nozik, A. J. *J. Appl. Phys.* **2006**, *100*, 074510/1.

(54) Alig, R. C.; Bloom, S.; Struck, C. W. *Physical Review B* **1980**, *22*, 5565.

(55) Alig, R. C.; Bloom, S. *Phys. Rev. Lett.* **1975**, *35*, 1522.

(56) Ridley, B. K. *Quantum processes in semiconductors*; 2nd ed.; Oxford University Press: New York, **1988**.

(57) Tirino, L.; Weber, M.; Brennan, K. F.; Bellotti, E.; Goano, M. *Journal of Applied Physics* **2003**, *94*, 423.

(58) Ziaja, B.; London, R. A.; Hajdu, J. *Journal of Applied Physics* **2006**, *99*, 033514.

(59) Jung, H. K.; Taniguchi, K.; Hamaguchi, C. *J. Appl. Phys.* **1996**, *79*, 2473.

(60) Klein, C. A. *Journal of Applied Physics* **1968**, *39*, 2029.

(61) Kubarsepp, T.; Karha, P.; Ikonen, E. *Appl. Opt.* **2000**, *39*, 9.

(62) Shabaev, A.; Efros, A. L.; Nozik, A. J. *Nano Lett.* **2006**, *6*, 2856.

(63) Harbold, J. M.; Du, H.; Krauss, T. D.; Cho, K. S.; Murray, C. B.; Wise, F. W. *Physical Review B* **2005**, *72*.

(64) Guyot-Sionnest, P.; Wehrenberg, B.; Yu, D. *J. Chem. Phys.* **2005**, *123*, 074709.

(65) Pandey, A.; Guyot-Sionnest, P. *Science* **2008**, *322*, 929.

(66) Klimov, V. I. *J. Phys. Chem. B* **2000**, *104*, 6112.

(67) Gali, A.; Voros, M.; Rocca, D.; Zimanyi, G. T.; Galli, G. *Nano Letters* **2009**, *9*, 3780.

(68) Schaller, R. D.; Agranovitch, V. M.; Klimov, V. I. *Nature Physics* **2005**, *1*, 189.

(69) Rupasov, V. I.; Klimov, V. I. *Physical Review B* **2007**, *76*.

(70) Franceschetti, A.; An, J. M.; Zunger, A. *Nano Lett.* **2006**, *6*, 2191.

(71) Klimov, V. I. *Appl Phys. Lett.* **2006**, *89*, 123118.

(72) Gabor, N. M.; Zhong, Z. H.; Bosnick, K.; Park, J.; McEuen, P. L. *Science* **2009**, *325*, 1367.

(73) Ma, W.; Luther, J. M.; Zheng, H.; Wu, Y.; Alivisatos, A. P. *Nano Letters* **2009**, *9*, 1699.

(74) Luo, J.-W.; Franceschetti, A.; Zunger, A. *Nano Letters* **2008**, *8*, 3174.

(75) McGuire, J. A.; Sykora, M.; Joo, J.; Pietryga, J. M.; Klimov, V. I. *Nano Lett.* **2010**.

(76) Wang, S.; Khafizov, M.; Tu, X.; Zheng, M.; Krauss, T. D. *Nano Letters* **2010**

, *10*, 2381.

(77) Klimov, V. I.; Mikhailovsky, A. A.; Xu, S.; Malko, A.; Hollingsworth, J. A.; Leatherdale, C. A.; Eisler, H.-J.; Bawendi, M. G. *Science* **2000**, *290*, 314.

(78) Law, M.; Luther, J. M.; Song, O.; Hughes, B. K.; Perkins, C. L.; Nozik, A. J. *J. Am. Chem. Soc.* **2008**, *130*, 5974.

(79) Pietryga, J. M.; Werder, D. J.; Williams, D. J.; Casson, J. L.; Schaller, R. D.; Klimov, V. I.; Hollingsworth, J. A. *J. Am. Chem. Soc.* **2008**, *130*, 4879.

(80) Luther, J. M.; Beard, M. C.; Song, Q.; Law, M.; Ellingson, R. J.; Nozik, A. J. *Nano Lett.* **2007**, *7*, 1779.

(81) Schaller, R. D.; Petruska, M. A.; Klimov, V. I. *J. Phys. Chem. B* **2003**, *107*, 13765.

(82) Norris, D. J.; Sacra, A.; Murray, C. B.; Bawendi, M. G. *Phys. Rev. Lett.* **1994**, *72*, 2612.

(83) Talapin, D. V.; Murray, C. B. *Science* **2005**, *310*, 86.

(84) Luther, J. M.; Law, M.; Beard, M. C.; Song, Q.; Reese, M. O.; Ellingson, R. J.; Nozik, A. J. *Nano Letters* **2008**, *8*, 3488.

(85) Swart, I.; Sun, Z.; Vanmaekelbergh, D.; Liljeroth, P. *Nano Lett.* **2010**.

(86) Hines, M. A.; Guyot-Sionnest, P. *J. Phys. Chem. B* **1996**, *100*, 468.

(87) Jeong, S.; Achermann, M.; Nanda, J.; Ivanov, S.; Klimov, V. I.; Hollingsworth, J. A. *J. Am. Chem. Soc.* **2005**, *127*, 10126.

(88) Nirmal, M.; Dabbousi, B. O.; Bawendi, M. G.; Macklin, J. J.; Trautman, J. K.; Harris, T. D.; Brus, L. E. *Nature (London)* **1996**, *383*, 802.

(89) Gomez, D. E.; Califano, M.; Mulvaney, P. *Physical Chemistry Chemical Physics* **2006**, *8*, 4989.

(90) Cichos, F.; von Borczyskowski, C.; Orrit, M. *Current Opinion in Colloid & Interface Science* **2007**, *12*, 272.

(91) Wang, L. W.; Califano, M.; Zunger, A.; Franceschetti, A. *Phys. Rev. Lett.* **2003**, *91*, 4.

(92) Jha, P. P.; Guyot-Sionnest, P. *ACS Nano* **2009**, *3*, 1011.

(93) Efros, A. L.; Rosen, M. *Phys. Rev. Lett.* **1997**, *78*, 1110.

(94) Verberk, R.; van Oijen, A. M.; Orrit, M. *Phys. Rev. B* **2002**, *66*, 233202.

(95) Li, S.; Steigerwald, M. L.; Brus, L. E. *ACS Nano* **2009**, *3*, 1267.

(96) Mahler, B.; Spinicelli, P.; Buil, S.; Quelin, X.; Hermier, J. P.; Dubertret, B. *Nature Materials* **2008**, *7*, 659.

(97) Hohng, S.; Ha, T. *J. Am. Chem. Soc.* **2004**, *126*, 1324.

(98) Wang, X. Y.; Ren, X. F.; Kahen, K.; Hahn, M. A.; Rajeswaran, M.; Maccagnano-Zacher, S.; Silcox, J.; Cragg, G. E.; Efros, A. L.; Krauss, T. D. *Nature* **2009**, *459*, 686.

(99) Shimizu, K. T.; Neuhauser, R. G.; Leatherdale, C. A.; Empedocles, S. A.; Woo, W. K.; Bawendi, M. G. *Phys. Rev. B* **2001**, *63*, 5.

(100) Peterson, J. J.; Nesbitt, D. J. *Nano Lett.* **2008**, *9*, 338.

(101) Wise, F. W. *Acc. Chem. Res.* **2000**, *33*, 773.

(102) Rogach, A. L.; Eychmüller, A.; Hickey, S. G.; Kershaw, S. V. *Small* **2007**, *3*, 536.

(103) Ashcroft, N. W.; Mermin, N. D. *Solid State Physics*; W.B. Saunders Company, **1976**.

(104) Rabani, E.; Baer, R. *Chem. Phys. Lett.* **2010**, *496*, 227.

(105) Efros, A. L.; Efros, A. L. *Sov. Phys. Semicond.* **1982**, *16*, 772.

(106) Banyai, L.; Koch, S. W. *Semiconductor Quantum Dots*; World Scientific: River Edge, NJ, **1993**.

(107) Wolf, M.; Brendel, R.; Werner, J. H.; Queisser, H. J. *Journal of Applied Physics* **1998**, *83*, 4213.

(108) Smith, D. K.; Luther, J. M.; Semonin, O. E.; Nozik, A. J.; Beard, M. C. *ACS Nano* **2010**, *5*, 183.

(109) Lin, Z.; Franceschetti, A.; Lusk, M. T. *ACS Nano* **2011**, ASAP.

(110) Hines, M. A.; Scholes, G. D. *Advanced Materials* **2003**, *15*, 1844.

(111) Semonin, O. E.; Johnson, J. C.; Luther, J. M.; Midgett, A. G.; Nozik, A. J.; Beard, M. C. *J. Phys. Chem. Lett.* **2010**, *1*, 2445.

(112) Moreels, I.; Allan, G.; De Geyter, B.; Wirtz, L.; Delerue, C.; Hens, Z. *Physical Review B* **2010**, *81*, 235319.

(113) Penn, D. R. *Physical Review* **1962**, *128*, 2093.

(114) Sharma, A. C. *Journal of Applied Physics* **2006**, *100*, 8.

(115) Yoo, H. G.; Fauchet, P. M. *Physical Review B* **2008**, *77*, 115355.

(116) Luther, J. M.; Law, M.; Song, Q.; Perkins, C. L.; Beard, M. C.; Nozik, A. J. *Acs Nano* **2008**, *2*, 271.

(117) Law, M.; Beard, M. C.; Choi, S.; Luther, J. M.; Hanna, M.; Nozik, A. J. *Nano Letters* **2008**, *8*, 3904.

(118) Beard, M. C.; Turner, G. M.; Schmuttenmaer, C. A. *Nano Letters* **2002**, *2*, 983.

(119) Murphy, J. E.; Beard, M. C.; Nozik, A. J. *Journal of Physical Chemistry B* **2006**, *110*, 25455.

(120) Salvador, M. R.; Hines, M. A.; Scholes, G. D. *Journal of Chemical Physics* **2003**, *118*, 9380.

(121) Wang, R. Y.; Feser, J. P.; Lee, J. S.; Talapin, D. V.; Segalman, R.; Majumdar, A. *Nano Letters* **2008**, *8*, 2283.

(122) Scholes, G. D. *Acs Nano* **2008**, *2*, 523.

(123) Schuster, R.; Knupfer, M.; Berger, H. *Physical Review Letters* **2007**, *98*, 4.

(124) Johnston, K. W.; Pattantyus-Abraham, A. G.; Clifford, J. P.; Myrskog, S. H.; MacNeil, D. D.; Levina, L.; Sargent, E. H. *Applied Physics Letters* **2008**, *92*, 3.